DISTANT OBSCURED QUASARS

Alejo Martínez-Sansigre

Wolfson College, Oxford

Trinity Term 2006

THESIS SUBMITTED IN FULFILMENT OF THE REQUIREMENTS

FOR THE DEGREE OF DOCTOR OF PHILOSOPHY

DISTANT OBSCURED QUASARS

Alejo Martínez-Sansigre

Wolfson College, Oxford

Trinity Term 2006

THESIS SUBMITTED IN FULFILMENT OF THE REQUIREMENTS

FOR THE DEGREE OF DOCTOR OF PHILOSOPHY

Abstract

This thesis presents a study of high-redshift obscured (type-2) quasars, selected at mid-infrared and radio wavelengths. This population had remained elusive, even to hard X-ray surveys, and in Chapter 2 I compare the selection of type-2 quasars in X-ray and mid-infrared surveys, as well as explaining the criteria I will use to search for these objects at $z \sim 2$, around the peak in the unobscured (type-1) quasar activity.

Chapter 3, presents a sample of radio-intermediate type-2 quasars selected from the criteria described in Chapter 2. Optical spectroscopy shows indeed that at least half of the objects have the characteristic narrow emission lines, and lie around the expected redshift of $z = 2$. The other half of the objects are consistent with also being type-2 quasars at similar redshifts, although no emission lines are visible.

In Chapter 4, I discuss the possibility of two types of obscured quasars, some obscured by a dusty torus and some by a dusty host galaxy, to explain the lack of emission lines in half of the sample. I model the number of type-1 quasars expected to follow similar selection criteria and at the same redshifts as our type-2 quasars, and find that the obscured quasars outnumber the unobscured by a ∼2-3:1 ratio. I conclude that most supermassive black hole growth is obscured by dust. When comparing this to predictions from unified schemes, I find that this result is only consistent with the schemes provided host-obscuration is indeed happening. The lower ratio of type-2 to type-1 quasars inferred from X-ray surveys (∼1:1) suggests that some of the type-2 quasars in this sample might be Compton thick.

Radio data taken at three frequencies, are presented in Chapter 5, to study the spectral properties and intrinsic luminosities of our sample. I show that some type-2 quasars have flat radio spectra, which is inconsistent with obscuration by the torus, but consistent with host-obscuration. Some

gigahertz-peaked spectra, characteristic of young radio jets, are present, but the majority of the sources have very steep spectra. These steep spectral indices can be explained by active developed jets in which continuous injection of electrons is accompanied by inverse-Compton losses against the cosmic microwave background.

In Chapter 6, I select a similar sample of type-2 quasars in a different field, where X-ray data are available. The selection criteria are kept identical, except for the radio flux density cut, which is lowered. This is expected to introduce significant numbers of starburst contaminants. To filter these out, and due to a lack of spectroscopy, I use a bayesian method to fit the spectral energy distributions, obtain photometric redshifts, and select between a quasar and a starburst model. I measure the X-ray properties for the resultant sample of type-2 quasars. The entire sample is found to be Compton-thick, and repeating the modelling of Chapter 4, I find that the population of Compton-thick quasars is at least comparable to the population of unobscured quasars, and probably larger.

Declaration

I declare that no part of this thesis has been accepted or is currently being submitted for any degree or diploma or certificate or any other qualification in this University or elsewhere.

This thesis is the result of my own work unless otherwise stated. The 610 MHz data used for Chapter 5 was reduced by Timothy Garn and Dave Green. The bulk of the work for Appendix A was carried out by Chris Simpson, and Steve Rawlings reduced the radio image. For Appendix B, although I reduced the data, Chris Willott undertook most of the work.

Some of this work has appeared or will appear in refereed journals:

Martínez-Sansigre A., Rawlings S., Lacy M., Fadda D., Marleau F. R., Simpson C., Willott C. J., Jarvis M. J., 2005, Nat, 436, 666

Martínez-Sansigre A., Rawlings S., Lacy M., Fadda D., Marleau F., Simpson C., Willott C.J., Jarvis M.J., 2006, AN, 327, 266

Simpson C., Rawlings S., Martínez-Sansigre A., 2006, AN, 327, 270

Martínez-Sansigre A., Rawlings S., Lacy M., Fadda D., Jarvis M. J., Marleau F. R., Simpson C., Willott C. J., 2006, MNRAS, 370, 1479

Simpson C., Martínez-Sansigre A., Rawlings S., Ivison R., Akiyama M., Sekiguchi K., Takata T., Ueda Y., Watson M., 2006, MNRAS, 372, 741

Willott C.J., Martínez-Sansigre A., Rawlings S., 2006, AJ, in press (astro-ph/0610564)

Martínez-Sansigre A., Rawlings S., Garn T., Green D.A., Alexander P., Klöckner H.R., Riley J.M., 2006, MNRAS, 373L, 80

Martínez-Sansigre A., et al., Rawlings S., Bonfield D.G., Mateos S., Simpson C., Watson M., Almaini O., Foucaud S., Sekiguchi K., Ueda Y., 2006, MNRAS, submitted (astro-ph/0611739)

Dedicada, con mucho cariño, a mis padres Marta y Luis, y a mi hermana Esther

Acknowledgements

I am very grateful to Steve Rawlings for the opportunities he has given me during these three years, for his enthusiasm and for his extensive help during this project. Most of all, for organising regular football games so I could keep my good habit of limping regularly. I also have big thanks for Matt Jarvis, Hans-Rainer Klöckner, Mark Lacy, Chris Simpson and Chris Willott, for their important help and contributions to my work. I am also grateful to Dave Bonfield, Dario Fadda, Timothy Garn, Dave Green, Francine Marleau, Silvia Mateos and Mike Watson, for their contributions to this project, and to Filipe Abdalla, Jordi Barr, Eugenio Barrio, Caroline van Breukelen, Lee Clewley, Garret Cotter, Ian Heywood, Ryan Houghton, Davor Krajnović, Ewan Mitchell, Lance Miller, Dimitra Rigopoulou, Dan Smith, Andrew Taylor and Chris Wolf for comments and discussions.

This thesis is dedicated to my parents, Marta and Luis, and to my sister, Esther.

Contents

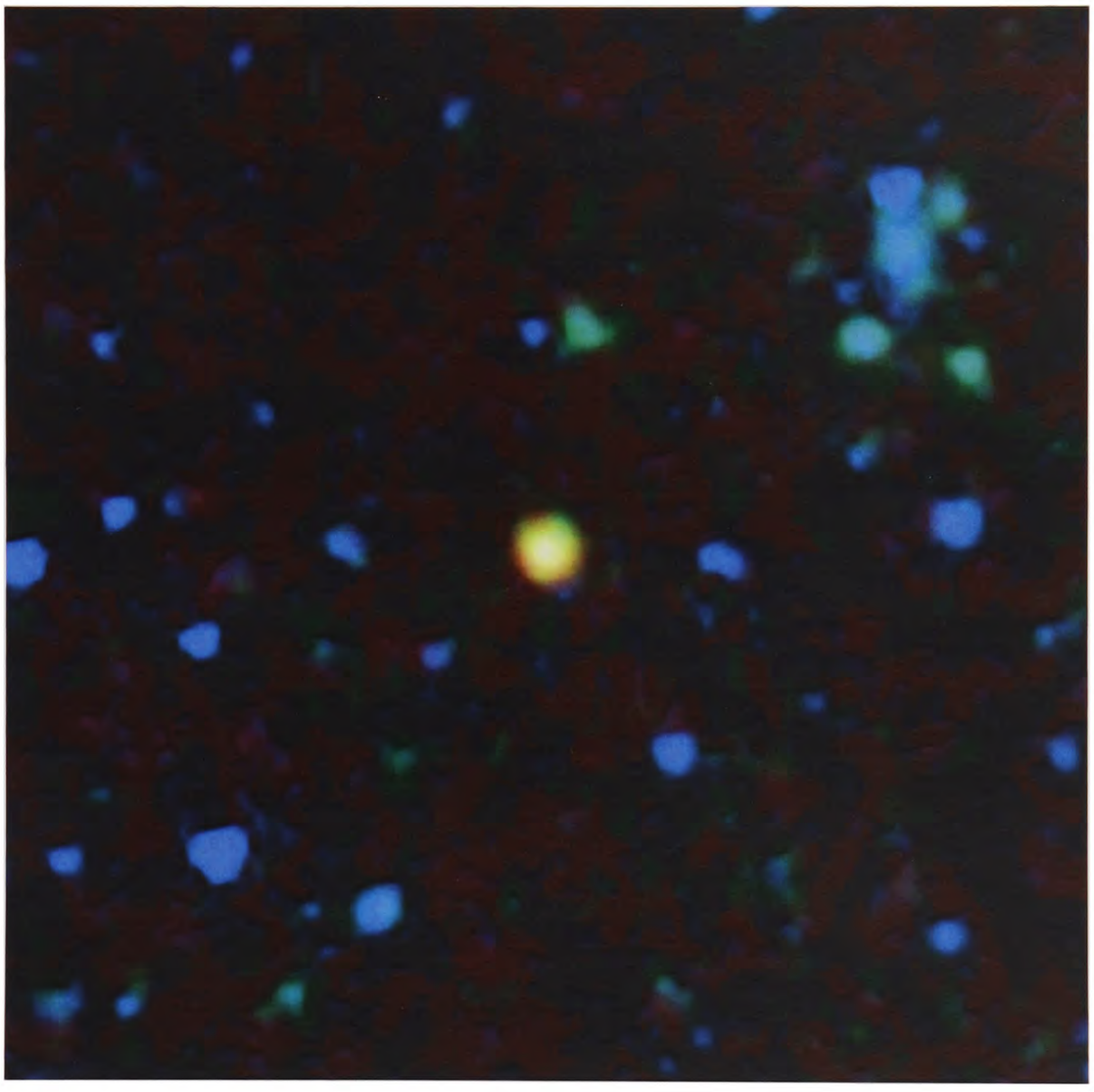

Figure 1: False colour image of AMS08, at $z = 1.979$. Blue, 3.6 μm; green, 24 μm; red, 1.4 GHz. Prepared by Gordon Squires for the press releases of: "The obscuration by dust of most of the growth of supermassive black holes" Martínez-Sansigre A., Rawlings S., Lacy M., Fadda D., Marleau F., Simpson C., Willott C.J., Jarvis M.J., 2005, Nature, 436, 666

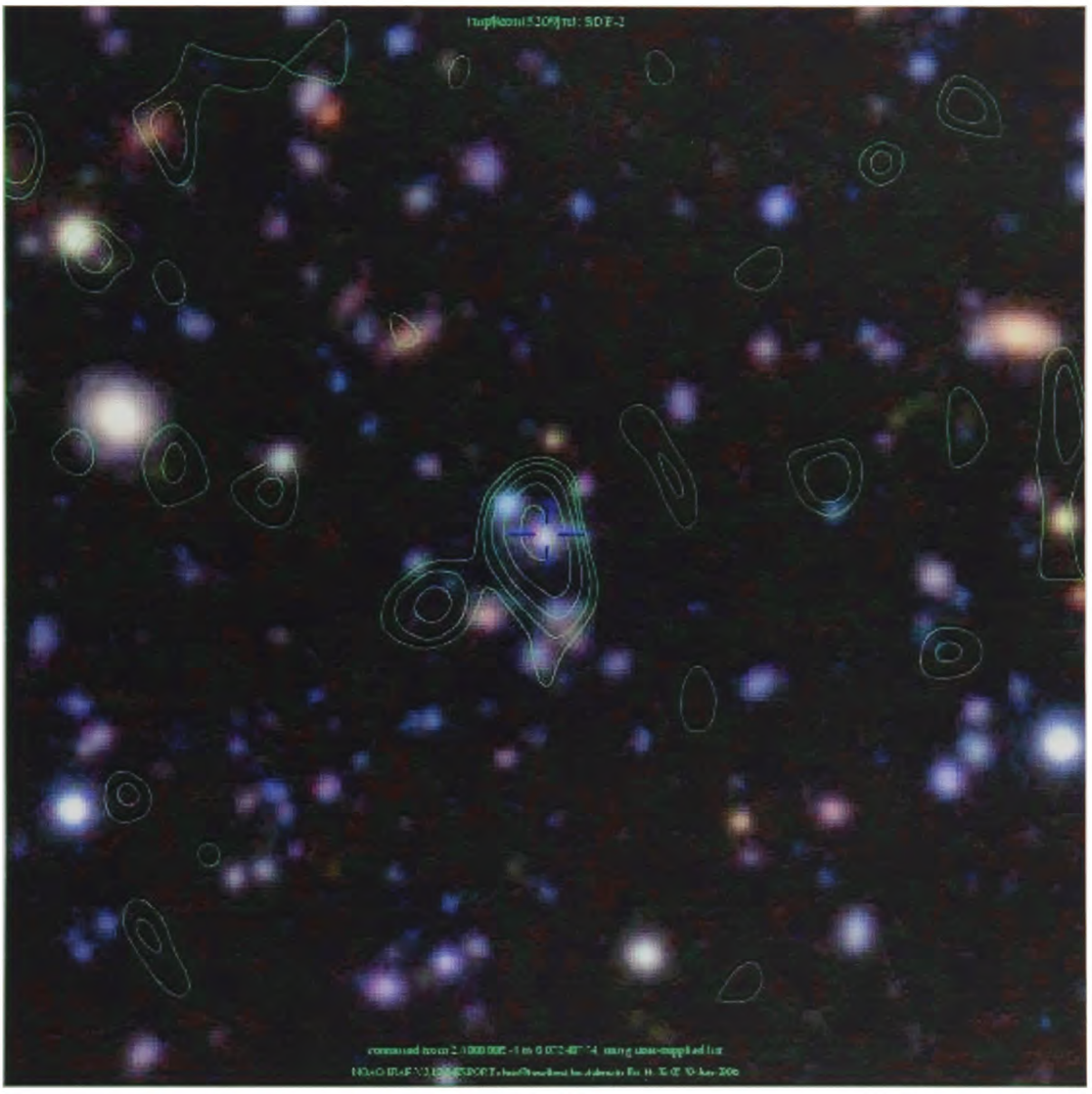

Figure 2: Composite image of ID401, an X-ray detected, Compton-thick quasar at $z_{\rm phot} = 1.90$. Blue, B-band; green, R-band; red, z-band; green contours, 1.4 GHz; blue cross, optical quasar identified with the radio source. Prepared by Chris Simpson.

Chapter 1

Introduction

It is currently believed that supermassive black holes underwent periods of exponential growth during which we see them as quasars in the distant Universe. For a long time, a population of obscured (type-2) radio-quiet quasars has been postulated, from the unification paradigm of Active Galactic Nuclei and from modelling the hard X-ray background (energies $\geq$ 1 keV) as the sum of the emission from extragalactic sources. These type-2 quasars would consist of supermassive black holes accreting vast amounts of matter, just like unobscured, or naked, (type-1) quasars. However, unlike the type-1 quasars which outshine their host galaxy at practically all wavelengths, type-2 quasars were expected to have large amounts of gas and dust blocking our line-of-sight to the accreting black hole. This gas and dust causes large amounts of extinction from the near-infrared (wavelengths $\sim$ 1 μm) to the soft X-rays (energies <1 keV), where type-2 quasars do not outshine their host galaxy and are therefore indistinguishable from normal galaxies in imaging surveys.

This thesis is concerned with finding high-redshift type-2 quasars, and understanding how their properties compare to those of type-1 quasars. To put this in context, the introduction will summarise the previous evidence for this hidden population.

1.1 Active Galactic Nuclei and the Unified Schemes

Observationally, at optical wavelengths, type-1 (unobscured) active galactic nuclei (AGN) are divided between sources powerful enough to outshine their host galaxy and those that are not. The former have most of their visible light emanating from a region too small to be resolved by

optical telescopes, and therefore look like point-sources or stars. They are known as quasi-stellar-objects (QSOs) or quasi-stellar-radio-sources (QSRS or quasars) if they are powerful emitters at radio frequencies (wavelength ≤ 1 mm). For simplicity, in this thesis these sources will be called quasars, irrespective of their radio properties. AGN of type-1 that are not powerful enough to outshine their host galaxy are known as Seyferts, with the dividing power sitting at approximately at B-band absolute magnitude, $M_{\rm B} = -23$ or X-ray luminosity, $L_{\rm X} = 10^{37}$ W.

There are many different definitions of what constitutes a type-2 AGN: X-ray astronomers will define this as an AGN with an absorbing column, $N_{\rm H}$, $\geq 10^{26-26.5}$ m^{-2} (e.g. Comastri et al., 1995). Optical astronomers define them as having narrow emission lines (< 2000 km s^{-1}), although the division is not necessarily clear-cut, and intermediate objects exist e.g. type 1.5 (see e.g. Antonucci, 1993). However, we note that the identification of such intermediate objects requires very high signal-to-noise spectra, which are not available here. Throughout this thesis, split AGN into three broad categories: type-1 (showing broad lines only), reddened (narrow UV lines but broad H α) and type-2 (narrow lines only). Simpson et al. (1999) found these optical definitions to correspond to values of extinction at visual band of $A_{\rm V} \lesssim 1$, $A_{\rm V} \sim 1 - 5$ and $A_{\rm V} \gtrsim 5$, and throughout this thesis we follow this separation. The definitions of type-2 from X-ray and optical wavelengths are therefore not necessarily matched, and this is discussed further in Chapter 2.

Type-2 AGN are then referred to as type-2 quasars or Seyfert-2s depending on whether their luminosities, corrected for obscuration, would or would not outshine the host galaxy.

The division between radio-loud or radio-quiet AGN is not well defined, but radio-quiet AGN have radio luminosities that are consistent with being caused by star-formation alone (see Condon 1992), while radio-loud AGN require powerful magnetic fields and jets to explain their radio luminosity. In this thesis, we take the division to lie at $L_{1.4\ \rm GHz} = 10^{24}$ W Hz^{-1} sr^{-1} (Miller et al., 1990).

In addition, the observed ionisation states are observed to vary. Seyfert-2s have higher ionisation states than Seyfert-1s, and a class of narrow-line Seyfert-1 exists (e.g. Osterbrock & Pogge, 1985), as well as low-ionisation nuclear emission-line region galaxies (LINERs). Amongst the radio-loud sources, examples are found of sources with large ($\sim$ 100 kpc) regions of ionised gas, with properties consistent with H-II region photoionisation (e.g. McCarthy et al., 1987).

The term AGN therefore encompasses a range of extragalactic sources with different observed properties, which are believed to be powered by a central supermassive black hole (SMBH, with $M_\bullet \gtrsim 10^6\,M_\odot$). While the dominant source of energy for "normal" galaxies is nuclear energy released at the cores of stars, the common underlying mechanism for all AGN is gravitational infall of matter onto a SMBH (see Rees, 1984). The energy is then transferred through the accretion disk or released via a range of thermal and non-thermal processes, most of which are beyond the scope of this introduction so we will focus here on the processes relevant to this thesis. The power emitted by an AGN is dependent on the mass of the SMBH as well as the accretion rate.

To summarise what is a very complicated system, AGN are believed to consist of an accreting SMBH with regions of hot ($T \sim 10^4$ K) gas and a dusty torus around it, and sometimes radio jets (see Figure 1.1 for a sketch). The accretion disk consists of hot gas spanning temperatures between $\sim 10^3$ K to $\sim 10^6$ K, and is responsible for the non-stellar luminosity of AGN between the near-infrared and the far-ultraviolet (except for blazars, sources where our line of sight is straight down the jet, and the optical continuum is from Doppler-boosted synchrotron radiation). Further away, and on the same plane as the accretion disk, is a large body of dust, believed to bulge out, which is known as the obscuring torus. This dust is believed to be at a range of temperatures between $\sim$ 1500 K and $\sim$ 100 K, and is therefore responsible for the observed far- to near-infrared emission of the AGN.

Zooming again towards the centre, one finds relativistic electrons, emitting large amounts of X-ray photons through synchrotron and inverse-Compton radiation. At a distance of <1 pc from the SMBH, clouds of ionised gas move with speeds in excess of 2000 km s^{-1}, with the observed emission lines greatly broadened by the Doppler shifts. These velocities, measured along the line of sight, are interpreted as either being a component of the orbital speed or a component of a disk wind (e.g. Chiang and Murray, 1996). Further out ($\sim$1 kpc), regions of ionised gas move with slightly lower speeds, and lead to narrower lines ($\lesssim$2000 km s^{-1}). This is supported by the evidence that both linewidth and ionisation state decrease as reverberation timescale increases (e.g. Wandel, Malkan & Peterson, 1999).

Finally, some AGN have been observed to have powerful radio-jets, although the exact physical process that produces these is not well understood. The electrons have relativistic speeds (with

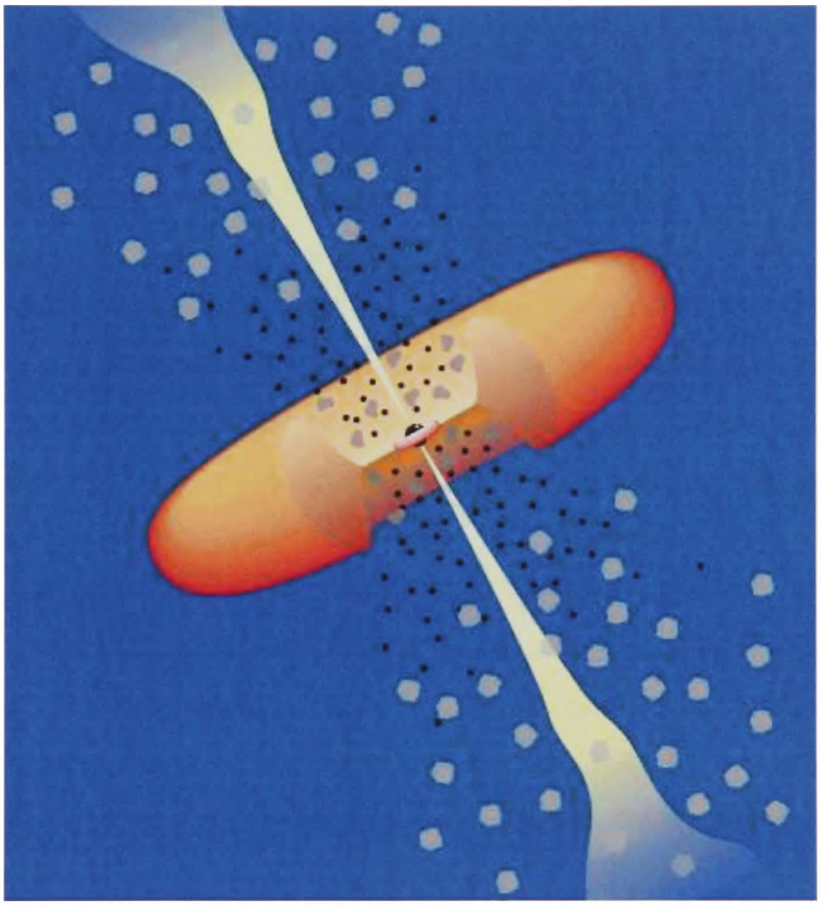

Figure 1.1: Cartoon representation of the unified scheme, from Urry & Padovani (1995). The dusty torus (orange) has been cut to reveal the accretion disk (yellow and pink) and the broad-line region (dark grey clouds). The narrow-line region (light grey clouds) is shown further away from the SMBH, and a radio jet is also represented (yellow). Copyright PASP, reprinted with permission of the authors.

v_e ~c) and emit synchrotron radiation, causing the jets to be visible at radio frequencies. The bulk motions of the electrons can reach speeds of $\sim$ 0.1c, where c is the speed of light, so if the AGN is active for $3\times \geq 10^5$ years, the jets can have sizes ($\geq$ 10 kpc) greater than the host galaxy. The possible mechanisms invoked to form these jets require the black hole to be spinning and to have strong magnetic fields, to extract energy in the form of non-thermal radiation (Blandford & Znajek, 1977).

The broad-line region and the accretion disk are only visible at a favourable viewing angle with respect to the torus, meaning that the appearance of the AGN in optical to soft X-rays is highly orientation-dependent. According to this scheme, type-2 quasars would consist of quasars with the symmetry axes perpendicular to the observer's line of sight, so that the dusty torus around the accretion disk would be viewed edge on, obscuring the optically-bright accretion disk and the broad-line region. This unfavourable orientation means type-2 quasars do not outshine their host galaxy at (rest-frame) ultra-violet or optical wavelengths, as is the case with the unobscured (type-1) quasars. Type-2 quasars are therefore indistinguishable from normal galaxies in optical imaging surveys.

While radio emission is isotropic at frequencies above the synchrotron self-absorption frequency, relativistic boosting of the jets can lead to radio spectral properties that are also dependent on viewing angle (ranging from narrow-line radio galaxies to blazars). For detailed reviews on the observational evidence behind this scheme, and the physical processes involved, see, for example Antonucci (1993), Urry & Padovani (1995), Krolik (1999) and Osterbrock & Ferland (2006).

The study of AGN is therefore plagued by selection-effects, so that surveys at a particular wavelength will be dominated by sources at a particular viewing angle or radio-power. While Seyfert-2s are found in large numbers in the local Universe, examples of type-2 quasars were originally limited to those sources bright enough at radio wavelengths to be detected in the early radio-surveys. From the existence of these narrow-emission-line radio galaxies as well as Seyfert-2s, the unified scheme was also expected to apply to radio-quiet quasars, and type-2 quasars were expected to exist with their numbers relative to the type-1 quasars determined by the torus opening angle.

1.2 The Hard X-ray Background

The cosmic hard X-ray background is believed to be the summed emission from accreting black holes, and the shape of the hard X-ray background (HXB) has been used to argue that most accretion, and hence most black hole growth, occurs in highly obscured regions. Comastri et al. (1995) assumed a population of absorbed AGN, with the same intrinsic spectrum and evolution as unobscured AGN, but with a range of obscuring Hydrogen column densities, $N_{\rm H}$, between 10^{25} and 10^{29} m^{-2}. The resulting best-fit ratio for absorbed ($N_{\rm H} > 10^{26.5}$ m^{-2}) to unabsorbed ($N_{\rm H} < 10^{26.5}$ m^{-2}) AGN was found to be ~3:1. The model assumed the same distribution of obscuring columns and redshifts for the low-X-ray luminosity objects ($L_{\rm X} < 10^{37}$ W; the Seyferts) and the high-X-ray luminosity objects ($L_{\rm X} > 10^{37}$ W; the quasars), including a population of highly obscured AGN (the Seyfert-2s and type-2 quasars).

If it is the gas and dust present in the torus which will obscure the X rays via photoelectric absorption and Compton scattering, then the obscured fraction will be dependent on the half-opening angle of the torus. If this angle is $\sim 40°$, as appears to be the case in radio-loud samples (e.g. Willott et al., 2000a), the population of type-2s is expected to be comparable in size to the type-1 population and not to outnumber it by a factor of ~3.

A modification to the standard unified scheme is the "receding torus" model (Lawrence, 1991) in which the more luminous AGN sublimate the dust in the inner edge of the torus out to larger distances than the less luminous AGN. This leads to a larger opening angle for more luminous AGN, so the fraction of type-1 quasars increases as a function of bolometric luminosity. Such luminosity dependence of the type-2 to type-1 ratio is indeed found, for example, in radio-selected samples by Willott et al. (2000a), in X-ray-selected samples by Ueda et al. (2003), and in spectroscopically selected samples by Simpson (2005).

More recent modelling of the hard X-ray background has consistently shown signs of a large population of obscured AGN (Wilman & Fabian, 1999; Worsley et al., 2005) and synthesis models have generally required a type-2 to type-1 ratio $\sim 3-4$:1 (Gilli et al., 2001; Ueda et al., 2003; Treister & Urry, 2005). However, the bulk of the sources required to fit the unresolved X-ray background have moderate redshifts ($z = 0.5-1$) and X-ray luminosities ($L_{\rm X} \sim 10^{36}$ W) characteristic of Seyferts rather than quasars. The latest studies of the hard X-ray background indeed

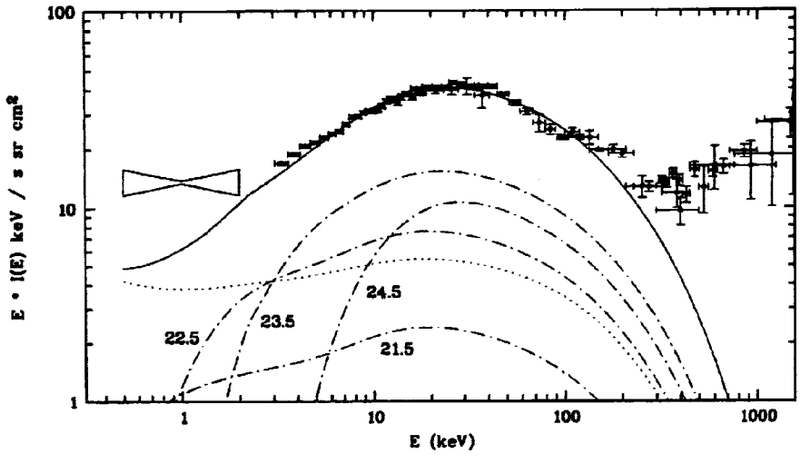

Figure 1.2: The hard X-ray background (HXB), Figure and models from Comastri et al. (1995). The solid line is the best fit model, overlayed on the measurements of the HXB. The dotted lines represent the contributions to the model from unobscured sources, while the dash-dotted lines represent the contributions from sources with different absorption, in $\log_{10}(N_{\rm H}/{\rm cm}^{-2})$. Copyright A&A, reprinted with permission of the authors.

suggest a luminosity-dependent Compton-thin-type-2 to type-1 ratio, which decreases to $\lesssim$1:1 at the higher luminosities corresponding to quasars (Ueda et al., 2003; Treister & Urry, 2005). The true type-2 to type-1 ratio will remain unknown until the Compton-thick population ($N_{\rm H} > 10^{28}$ m^{-2}) is unveiled.

1.3 Obscured Quasars from X-ray and Mid-infrared Surveys

Deep hard X-ray surveys have now revealed a large population of obscured AGN (see Brandt & Hasinger, 2005, for a review), but again most of these sources have moderate X-ray luminosities ($L_{\rm X} < 10^{37}$ W) and are better described as Seyfert-2s rather than type-2 quasars. Amongst objects with X-ray luminosities large enough to qualify as quasars, the ratio of type-2 to type-1 objects appears to be only $\sim$1:1 (e.g. Zheng et al., 2004), although redshift completeness at faint optical magnitudes ($m_{\rm R} > 23$, Vega) may still be an issue. Despite the great progress with the deep hard X-ray surveys, at high energies (above 6-8 keV) only $\sim$ 50% of the hard X-ray background is accounted for by individual sources, suggesting the existence of a substantial population of Compton-thick AGN which contribute to the hard X-ray background but are missing from current flux-limited X-ray surveys (Worsley et al., 2005). Indeed, a good example is the type-2 quasar

IRAS FSC 10214+4724: this object, found in an IRAS 60 μm survey (Rowan-Robinson et al., 1991), has recently been found to be Compton-thick (Alexander et al., 2005a).

An alternative strategy for looking for type-2 objects is to look for the mid-infrared emission. IRAS FSC 10214 +4724, at $z \sim 2.3$, is a classic type-2 object (e.g Serjeant et al., 1998). However, due to the limited sensitivity of IRAS, this object was only detected due to a huge gravitational lens magnification ($\sim$ 50) of the flux (Broadhurst & Lehar, 1995). The dramatic increase of mid-infrared sensitivity allowed by the Spitzer Space Telescope (Werner et al., 2004) means that similar objects can now be found without the 'benefit' of gravitational lensing, and mid-infrared selection should be sensitive to the Compton-thick quasars missed by X-rays.

1.4 Starbursts and Quasars in the mid-infrared

Quasars are bright mid-infrared emitters due to the warm dust present in the obscuring torus, but any mid- or far-infrared selected sample will also include large numbers of star-forming galaxies. Star formation requires gas and dust as fuel, and young stars are often enshrouded in dust. As a result, $\sim$60% of the star-formation in the local Universe is obscured by dust (e.g. Takeuchi et al., 2006).

Heavily star-forming galaxies are therefore powerful emitters in the mid- and far-infrared, and will be present in any mid-infrared selected sample. These "starburst" galaxies follow a correlation between their far-infrared (FIR) and radio emission (both thermal and non-thermal), with the star-formation rate as the (dominant) variable controlling both the radio and FIR luminosities. This correlation is believed to occur due to massive ($\geq$ 5 $M_{\odot}$) stars heating the cool dust (T $\sim$ 40 K) responsible for the FIR emission, and also causing the radio emission (both synchrotron and bremsstrahlung) from supernovae remnants. Only radio-quiet quasars obey this correlation (e.g. Sopp & Alexander, 1991) , since their radio and FIR emissions are dominated by the starburst, while in radio-intermediate ($L_{1.4\ \mathrm{GHz}} \sim 10^{24}$ W Hz^{-1} sr^{-1}) and radio-loud quasars the radio emission is dominated by the radio jets.

The FIR-radio correlation therefore provides a way of selecting quasars in far- and mid-infrared surveys, by selecting objects with a "radio excess" over their FIR luminosity. This correlation does translate to the mid-infrared (e.g. Cohen et al., 2000), but the mid-infrared spectra of quasars

and starbursts complicate the issue.

Starburst galaxies have several prominent features in their mid-infrared spectra, notably polyaromatic hydrocarbon (PAH) emission lines and two silicate absorption features (e.g. the spectrum of NGC7714 used in Figure 2.5, from Brandl et al., 2004). This means that the observed flux density of starbursts in the mid-infrared will vary strongly as a function of redshift. Quasars have typically a power-law spectrum, with the only relevant lines being due to the silicates. The silicate 9.7 μm feature can be seen in absorption for obscured sources, or even in emission for type-1 quasars where the torus is seen face-on (for recent results see Siebenmorgen et al., 2005; Ogle et al., 2006).

The mid-infrared therefore provides a natural place to look for obscured quasars, since they are strong mid-infrared emitters, even when obscured. In addition, the FIR-radio correlation and the mid-infrared spectral shape are useful tools to distinguish starbursts from quasars, unless, of course, one finds composite objects.

1.5 Overview

Following the success of mid-infrared selection in finding type-2 radio-quiet quasars at $z \sim 0.5$ (Lacy et al., 2004, 2005a), we combined data from the Spitzer MIPS instrument at 24 μm (Marleau et al., 2004; Fadda et al., 2006), IRAC at 3.6 μm (Lacy et al., 2005b) and from the Very Large Array (VLA) at 1.4 GHz (Condon et al., 2003) and devised strict selection criteria to hunt for higher redshift type-2s. The trade-off between our method and X-ray selection is that our quasars are intrinsically more luminous than AGN found in the deep hard X-ray surveys.

The format of this thesis is as follows. In Chapter 2, we compare X-ray and mid-infrared selection of obscured quasars. We then explain in detail the selection criteria which we used to find a sample of high-redshift type-2 quasars. Chapter 3 includes the description of the observations and the resulting optical spectra of our sample. In addition, we compare our sample to the well studied radio-loud samples. In Chapter 4 we model the type-2 to type-1 fraction by applying our selection criteria to a type-1 luminosity function, and we discuss the implications of the resulting quasar fraction. Chapter 5 is dedicated to radio-follow up of our sample, and the conclusions about orientation and age that can be inferred. In Chapter 6 we describe selection of a similar sample

in a field with X-ray data. We devise a method to separate type-2 quasars from contaminants, and discuss the implications of the X-ray properties of mid-infrared (and radio) selected quasars. Chapter 7 discusses the conclusions that we can make from this study. In addition, we include Appendix A, the radio catalogue in the Subaru-XMM-Newton Deep Field, and the conclusions made from it, as well as Appendix B, a CO (2-1) study of a hyperluminous quasar (3C318). Throughout this thesis we adopt a Λ Cold Dark Matter (ΛCDM) cosmology with the following parameters: $h = H_0/(100 \text{ km s}^{-1} \text{ Mpc}^{-1}) = 0.7$; $\Omega_\text{m} = 0.3$; $\Omega_\Lambda = 0.7$.

Chapter 2

Selection of distant obscured quasars

2.1 Comparison between X-ray and Mid-infrared Selection

In the unified scheme for AGN (Antonucci, 1993), the central engine is surrounded by a torus of dust which will obscure the broad-line region from certain lines-of-sight. The optical classification for quasars is that type-1s should show broad lines (and strong optical-UV continuum) while the type-2s are those objects where the dusty torus is obscuring the broad line region, so only narrow lines are seen. This classification is concerned with the optical/UV properties, and Simpson et al. (1999) found that the dividing extinction for radio-selected (3CR and 3CRR) objects corresponded to $A_V \gtrsim 5$, with a low fraction of objects with A_V in the range 5-15 and a large fraction with $A_V \gtrsim 15$. Note also that the Simpson et al. (1999) study found that most type-1s ($A_V \lesssim 5$) had $A_V \sim 0$, with only a small fraction lightly reddened ($A_V \sim 1-5$). Gas and dust are responsible for obscuring the X-rays emitted from the central engine, and the geometrical distribution of the gas is almost certainly different from that of the dust. It is possible to imagine lines-of-sight which "graze" the dusty torus, leading to small amounts of extinction in the optical, but which go through significant additional amounts of gas. Such a line-of-sight would lead to a quasar classified as "reddened" (not type-2) in the optical ($A_V \simeq 1-5$) but as type-2 ($N_H \gtrsim 10^{26}\,m^{-2}$) in X-rays. The converse situation, where an optically obscured quasar is barely absorbed in X-rays, is harder to envisage: any line of sight that passes through significant amounts of dust will lead to significant absorption in the X-rays. It seems therefore unlikely that optical type-2 quasars will have negligible X-ray absorption. However, in edge-on sources, the nuclear soft X-ray

emission can plausibly be scattered from optically thin material located above or below the plane of the torus, leading to an optically-obscured AGN with a soft X-ray spectrum. Finally, obscuring material in the host galaxy of the AGN can further complicate interpretation. Independently of the orientation of the torus, dust and gas in the host galaxy can cause extinction and absorption with a huge range in A_V and N_H.

X-ray and optical definitions of obscured AGN are therefore slightly different and the range of gas-to-dust ratios found by comparing dust-reddening in the optical or near-infrared and X-ray absorption suggests they are not always matched (e.g. Willott et al., 2003b; Urrutia et al., 2005; Wilkes et al., 2005). We note that we have used a mid-infrared plus radio selection, but since the role of the radio criterion was to avoid non-AGN contaminants (see Section 2.2), in this Section we can proceed to consider our technique as basically mid-infrared selection. The effect of adding the radio flux density cuts is to constrain the type-2 quasars selected to those at the high end of the radio-to-optical correlation for radio-quiet quasars of Cirasuolo et al. (2003), as described in in Section 2.2. It is of course plausible that radio luminosity correlates in some complicated way with joint mid-infrared, X-ray detectability but we ignore this possibility here.

This section aims to compare the "merits" of mid-infrared and X-ray selection by considering a model quasar (described in section 2.1.1) with varying amounts of dust extinction (section 2.1.2) and different gas-to-dust ratios (section 2.1.3). We also consider the effects of different types of dust (section 2.1.5) and the orientation dependence of 24-μm emission (section 2.1.6).

2.1.1 Model quasar

We choose this quasar to have $M_B = -25.7$ since this corresponds to the break in the optical quasar luminosity function at $z = 2$ (Croom et al., 2004), the redshift of interest in the analysis in Martínez-Sansigre et al. (2005) and Chapter 4. The model quasar is assumed to have an intrinsic unreddened type-1 spectral energy distribution (SED), which we take from Rowan-Robinson (1995). This model covers the range between the (rest-frame) far-infrared and 4 keV. We need to complement this with a spectral energy distribution, or SED, that goes into the hard X-rays, so we assume the Madau et al. (1994) spectrum with the form $L_\nu \propto \nu^{-0.9}\exp(-\nu/\nu_c)$ with $h\nu_c = 360$ keV. This intrinsic unabsorbed type-1 spectrum is chosen as it was used by Wilman & Fabian (1999) for the models we use for absorbed X-ray spectra. This is practically a flat X-ray

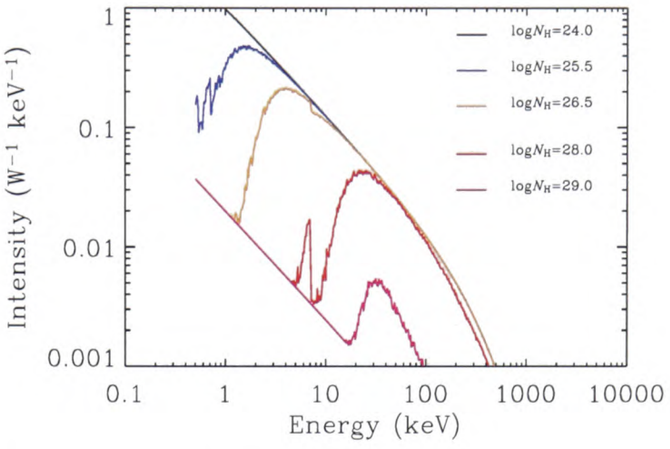

Figure 2.1: Intensity (arbitrary normalisation) vs Energy for a representative sample of the X-ray spectra from Wilman & Fabian (1999) used for our model type-2 quasar. The black line is the intrinsic spectrum absorbed by $N_{\rm H} = 10^{24}$ m^{-2} due to the Milky Way.

SED, and in the range probed by observations at 24 μm (for $z \leq 5$), the SED is also flat ($L_\nu \propto \nu^{-1}$ so $\nu L_\nu \propto \nu^0$). We choose the normalisation to match the Rowan-Robinson (1995) SED at 2 keV.

2.1.2 Obscuration by dust

Starting with this type-1 SED, we proceed to model the obscuration of it with dust and gas. In recent times, the type of dust present in type-1 quasars (from the SDSS sample of Richards et al., 2002b) has been described as "grey" and alternatively as similar to that of the Small Magellanic Clouds (SMC). Grey dust shows a relatively flat extinction law in the optical and UV, while SMC-type dust is characterised by a steep increase in the extinction at UV wavelengths. Milky Way (MW)-type dust has a UV extinction law which sits in between that of grey and SMC dust. Richards et al. (2003) and Hopkins et al. (2004) have found the dust in the SDSS type-1 sample to be closest to that found in the SMC, while Czerny et al. (2004) and Gaskell et al. (2004) argued that extinction curves flatten in the UV (grey dust). However, Willott (2005) has shown this implication of grey dust to be a selection effect. The main selection effect arises from measuring dust-reddening from a composite constructed from a flux limited sample: the UV part of the composite is constructed from the higher redshift quasars, which will only make the sample if they are intrinsically brighter and have very little extinction due to dust. This leads to a negative correlation between $E(B-V)$ and redshift, so that different parts of the composite spectrum

are dominated by quasars with different amounts of dust. The result is a derived dust extinction curve which appears to flatten in the UV (see Willott, 2005, for more details).

We use the extinction curves from Pei (1992), with the extinction at (observed) 24 μm given in terms of the extinction at rest-frame visual band, A_V, and a particular dust type. The quasars in the SDSS sample are all type-1s, and the dust discussed in the above paragraph is not necessarily associated with the torus. The SMC has sub-solar metallicity, while the nuclear regions around quasars have solar or super-solar metallicities, with dust properties probably closer to the MW. The effects of different types of dust are secondary compared to the gas-to-dust ratio, yet important, so we assume MW-dust in Figure 2.2 and discuss the effect of large magellanic cloud (LMC) and SMC-type dust in Section 2.1.5 and in Figure 2.3. Dust extinction is small at rest-frame 24 μm, yet the extreme obscuring columns present in the torus and the large redshifts discussed here mean that dust obscuration is not necessarily negligible at observed 24 μm. In particular, the 9.7 μm silicate absorption feature can have a very important effect on observed 24-μm flux density at $z \sim 1.5$ and this feature is significantly deeper for SMC-type dust than for MW-type dust, Figure 2.3. This is due to a lower graphites to silicates ratio in the SMC; Pei (1992).

2.1.3 X-ray absorption

In contrast to dust extinction, which increases with redshift, X-ray absorption decreases at higher frequencies, meaning X-ray samples benefit from a "negative K-correction". The X-ray spectra of heavily absorbed quasars can only be modelled correctly via Monte-Carlo simulations, so we use the models of Wilman & Fabian (1999) (see Figure 2.1 for a sample). These assume the intrinsic unabsorbed type-1 spectrum metioned earlier, and assume an Fe abundance 5-times solar, which provides a better fit to the hard X-ray backround. The particular models which we use here ignore the reflection component of X-ray spectra. This is because low-luminosity objects are known to exhibit a reflection component that is unimportant in high-luminosity objects such as our model quasar. The models do include a 2% scattered component, to represent the flux scattered into the line of sight by electrons in the ionized medium $\sim$ 1 kpc away from the SMBH. This scattered component has no effect on our discussion above $z \gtrsim 0.5$. The obscuring column of Hydrogen, responsible for both types of absorption, is given here as a function of A_V by assuming a gas-to-dust ratio.

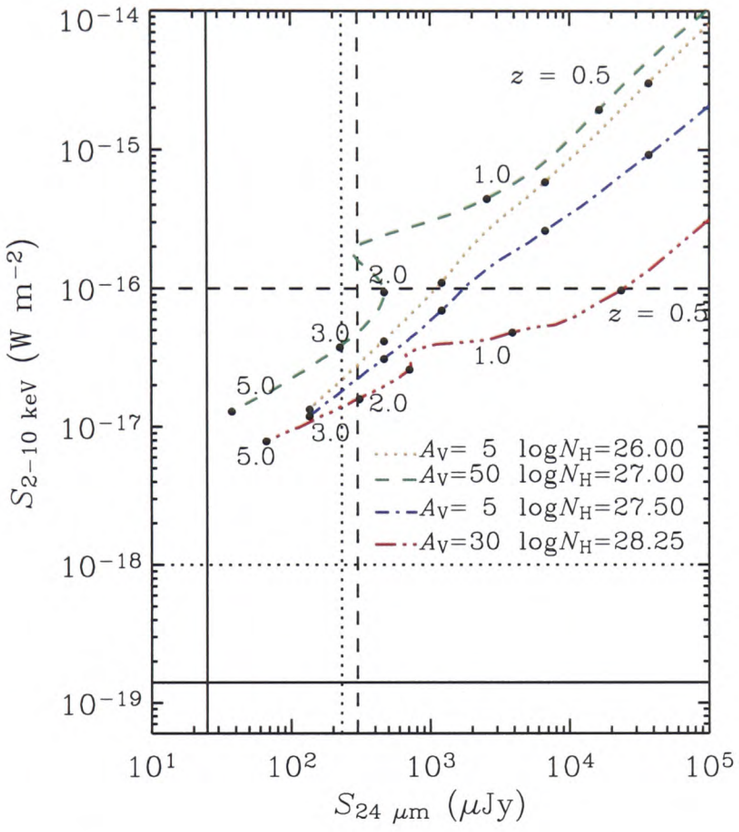

Figure 2.2: Hard X-ray flux ($S_{2-10\mathrm{keV}}$) versus 24-μm flux density ($S_{24\ \mu\mathrm{m}}$) as a function of redshift for the model quasar described in Section 2.1. The tracks have the redshifts labelled at the positions marked with black dots at $z = 0.5$, 1, 2, 3 and 5, and they show the effect on the quasar of MW-type dust with two different gas-to-dust ratios: $N_\mathrm{H} = 1.9 \times 10^{25}\ \mathrm{m}^{-2} \times A_\mathrm{V}$ (Milky-Way, top two lines) and $N_\mathrm{H} = 5 \times 10^{26}\ \mathrm{m}^{-2} \times A_\mathrm{V}$ (bottom two lines). Two tracks are drawn for each gas-to-dust ratio, $A_\mathrm{V} = 5$ and 50 for the MW gas-to-dust ratio and $A_\mathrm{V} = 5$ and 30 for the higher gas-to-dust ratio. The legend shows the combination of A_V and N_H [in $\log10(N_\mathrm{H}/\mathrm{m}^{-2})$] for each track. For the larger A_V, the 9.7 μm silicate absorption feature can be seen as a "meander". The dashed straight lines mark typical limits for deep surveys covering large areas ($\sim 4-5$ deg^2), while the solid straight lines show the limits for the GOODS fields, ultra-deep surveys which cover $\sim$ 0.1 deg^2. As an example of the large area Spitzer surveys, we have taken the flux density limit for 24-μm from the FLS (flux limit from Martínez-Sansigre et al., 2005, catalogue from Fadda et al., 2006), while the X-ray flux is taken from the ASCA survey of Ueda et al. (1999). For the deeper GOODS surveys, the 24-μm flux density limit is as quoted by Treister et al. (2006) and the X-ray flux limit is from Alexander et al. (2003). We note that the latter is actually in the 2-8 keV band (not 2-10 keV quoted here) but this relatively small difference does not alter our argument. Finally, the dotted lines are for the SXDF limit, a deep survey which has $\sim$1 deg^2 of deep X-ray data with 24-μm data from SWIRE (Lonsdale et al., 2003, Ueda et al. in prep).

The Milky Way is known to have a gas-to-dust ratio such that $N_{\rm H} = 1.9 \times 10^{25}$ m$^{-2} \times A_{\rm V}$ (Bohlin et al., 1978, note this is per magnitude of extinction in V band), while the SMC has $N_{\rm H} = 1.8 \times 10^{26}$ m$^{-2} \times A_{\rm V}$ (Bouchet et al., 1985). Many AGN have been found to have higher gas-to-dust ratios than the MW (Maiolino et al., 2001; Willott et al., 2004). We therefore choose two representative values for the gas-to-dust ratio. The MW value is sometimes used as a "standard" gas-to-dust ratio. To show the effects of higher gas-to-dust ratios, we note that, for example, NGC 3281 has a value of $N_{\rm H} = 3.2 \times 10^{26}$ m$^{-2} \times A_{\rm V}$ (Simpson, 1998b), while Urrutia et al. (2005) study one object with $N_{\rm H} \sim 7.7 \times 10^{26}$ m$^{-2} \times A_{\rm V}$ (FTM1004+1229, assuming a factor $R = 3.0$, the average between the SMC and MW factors, to convert between $E(B-V)$ and $A_{\rm V}$). We therefore choose $N_{\rm H} = 5 \times 10^{26}$ m$^{-2} \times A_{\rm V}$ as a realistic higher value to illustrate the effect of different gas-to-dust ratios. This is not claiming we encompass the whole range in gas-to-dust ratios, but is chosen to illustrate how mid-infrared and X-ray selection are affected by variations in gas-to-dust ratio. The higher value of gas-to-dust ratio $N_{\rm H} = 5 \times 10^{26}$ m$^{-2} \times A_{\rm V}$ is high enough for an $A_{\rm V} = 20$ type-2 quasar to be Compton-thick.

2.1.4 Comparison

Figure 2.2 shows the X-ray flux in the 2-10 keV band ($S_{2-10{\rm keV}}$) versus the 24-μm flux density ($S_{24\mu{\rm m}}$) for type-2 quasars with a range in $A_{\rm V}$. MW-type dust is used to obscure the 24-μm emission, and two different gas-to-dust ratios are used. The top set of curves are for a MW gas-to-dust ratio ($N_{\rm H} = 1.9 \times 10^{25}$ m$^{-2} \times A_{\rm V}$), while the bottom curves are for $N_{\rm H} = 5 \times 10^{26}$ m$^{-2} \times A_{\rm V}$. For the higher value of $A_{\rm V}$, the 9.7 μm silicate absorption feature can be seen as a "meander". The caption in Figure 2.2 details the survey limits used for comparative purposes.

The effect of dust at observed 24 μm is small in the range $5 \lesssim A_{\rm V} \lesssim 50$. However, it is important to note that at $A_{\rm V} \sim 50$, type-2s will start to drop out of 24-μm selection (for the larger area surveys) at $z \sim 1.5$ (due to the silicate absorption) and at $z \gtrsim 2.5$ due to significant dust extinction at the shorter rest-frame wavelengths. For larger values of $A_{\rm V}$, the width of the silicate absorption line means type-2s in the range $1.3 \leq z \leq 1.7$ drop out of the sample. As long as the $A_{\rm V}$ is < 50, the model type-2 quasar would be detectable by the large area 24-μm surveys at $z \lesssim 3$ (FLS and SWIRE surveys: Fadda et al., 2006; Lonsdale et al., 2003, respectively).

In the ~ 5 deg^2 X-ray ASCA survey (Ueda et al., 1999) with flux limit 10^{-16} W m^{-2}, the

model type-2 quasars with $N_{\rm H} \lesssim 2 \times 10^{27}$ m^{-2} are hardly affected by the absorption, and would be detected at $z \lesssim 2$. For $N_{\rm H} \sim 3 \times 10^{27}$ m^{-2} only $z \lesssim 1.5$ type-2s are detected, and the ASCA survey would not have the sensitivity to detect Compton-thick quasars with $N_{\rm H} \gtrsim 1 \times 10^{28}$ m^{-2} above $z = 0.5$.

Since 24-μm selection becomes poor for objects with $A_{\rm V} \gtrsim 50$ and X-ray selection fails for objects with $N_{\rm H} \gtrsim 10^{24}$ m^{-2}, we can see clearly how the gas-to-dust ratio determines which of the two selections is better. For surveys covering a large area ($\sim 4-5$ deg^2), required to find of order ~50-100 $z \sim 2$ quasars around the break in the luminosity function, 24-μm selection will be able to pick out type-2s with $N_{\rm H} \geq 10^{28}$ m^{-2} as long as they have $A_{\rm V} \lesssim 50$. Therefore, for AGN with gas-to-dust ratios like that of the MW or higher, 24-μm selection would fare better than X-ray selection in these surveys. However, we do not know exactly the selection biases in measuring these gas-to-dust ratios, so the possibility of large numbers of AGN with gas-to-dust ratios lower than the MW is not excluded.

For such a gas-to-dust ratio, significantly lower than the MW (e.g. a tenth of the MW value), only quasars with $A_{\rm V} \gtrsim 50$ would be classified as type-2s by X-ray observations. An extreme $A_{\rm V} \gtrsim 5000$ would be required for the quasars to be Compton-thick. Such objects would not be detected by the larger area mid-infrared samples, and therefore X-ray selection would be more sensitive.

This model type-2 would be detected in the GOODS fields at the whole range of redshifts concerned here, both at 24 μm and at 2-10 keV (survey fluxes from Alexander et al., 2003; Treister et al., 2006, for X-ray and 24-μm respectively). So although the Compton-thick quasars have not been detected in the ASCA survey, they are, in theory X-ray detectable in the GOODS survey. The reason they have not been found in large numbers is probably an issue of space density, as our model type-2 quasar is rare and large areas are required to find significant numbers of these objects. In an area of ~ 0.1 deg^2, only 1-3 such quasars are expected at $z \sim 2$. GOODS therefore has the required sensitivity to find hard-X-ray-selected Compton-thick type-2 quasars at all redshifts $z \lesssim 5$, but they do not cover the area required for this.

Since the hard X-ray background is believed to be dominated by $z = 0.5 - 1$ Seyfert-2s, and since Seyferts have a much higher space density than quasars, a large area is not so crucial. However, Seyfert-2s will have typical fluxes $\lesssim 10-100$ times fainter than our model type-2 quasar,

and therefore, at all redshifts Seyfert-2s with $N_{\rm H} \geq 10^{28}$ m^{-2} will have $S_{\rm X} \lesssim 10^{-19} - 10^{-18}$ W m^{-2}. This was, of course, already known, as the deep X-ray surveys in GOODS have not been able to find a population of Seyfert-2s large enough to account for the hard X-ray backround. This has been explained by a bias against the most heavily obscured AGN both by X-ray observations and optical spectroscopy (Treister et al., 2004), and our argument is consistent with this.

Thus, to find be sensitive to the Compton thick quasars, one requires a survey with a 2-10 keV flux limit of about 10^{-18} W m^{-2} over a reasonably large area. Therefore, the SXDF survey (horizontal dotted line: Ueda et al. in prep.), which covers $\sim$1 deg^2 to this depth, should be able to find X-ray-selected Compton-thick quasars. Comparing to the SWIRE depth, we can see that in the region of the SXDF, X-ray selection is expected to be more sensitive than 24-μm selection, while still being able to find powerful type-2 quasars.

For Compton-thick objects, the X-ray selection function is almost flat for $0.5 \lesssim z \lesssim 2$. The dependence of this function on the assumed scattered component (assumed here to be 2%) is negligible above $z \gtrsim 0.5$. Below this redshift, a model curve lacking the scattered component would be flat so, for a quasar with a negligible scattered component, the selecton function would be flat at all redshifts up to $z \sim 2$ and not just for $0.5 \lesssim z \lesssim 2$ as is the case for a quasar with a 2% scattered component. The redshift distribution of Compton-thick type-2s, with $N_{\rm H} \sim 10^{28}$ m^{-2}, in a survey deep enough to find them would therefore be dominated by the volume of the survey as a function of redshift and the evolution of the luminosity function. This means that X-ray surveys deep enough to be sensitive to Compton-thick type-2 quasars should find a wealth of $1 \lesssim z \lesssim 2$ objects. Coincidentally, this would be complementary to 24-μm surveys, as the mid-infrared surveys would struggle to find heavily obscured type-2s ($A_{\rm V} \gtrsim 50$), especially in the range around $z \sim 1.5$.

2.1.5 Dust type

A second-order effect for mid-infrared selection is the type of dust obscuring the AGN, which is particularly important in the range $1.2 \lesssim z \lesssim 1.8$ due to the varying depth of the silicate absorption feature. Figure 2.3 shows the ratio of transmission (see Figure caption), at observed 24-μm, for MW- and SMC-type dust. It shows clearly that for $z \lesssim 3$ SMC-type dust will cause more absorption in the mid-infrared, in particular around 9.7-μm rest-frame ($z \sim 1.5$). Thus

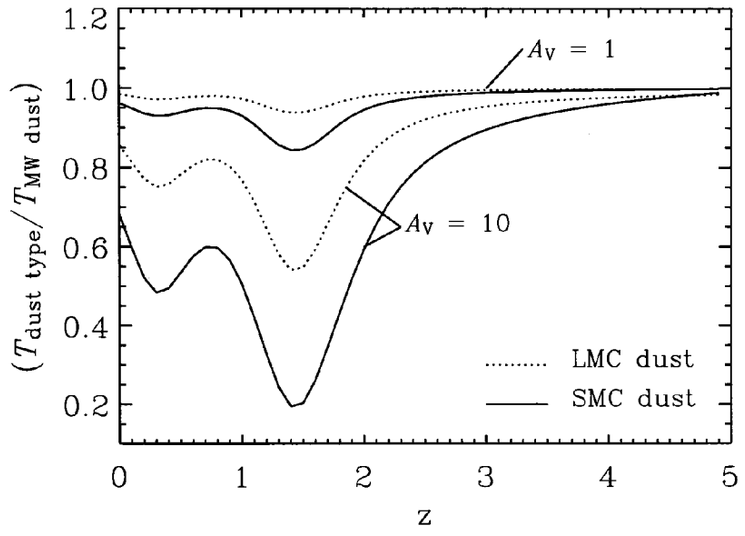

Figure 2.3: Curves showing the ratio of transmission for two dust types (LMC and SMC) over the transmission for MW-type dust, using the dust models of Pei (1992), and given two values of A_V. The transmission is here defined as $T = 10^{-A_\lambda/2.5}$. We use $\lambda = 23.7\ \mu\mathrm{m}/(1+\mathrm{z})$, the central wavelength of the MIPS instrument at 24 μm, accounting for the redshift. A_λ is parametrised as a function of A_V and is dependent on the type of dust. We plot and label curves for A_V =1 and 10, and include LMC as well as SMC-type dust for comparative purposes. The different extinction curves show that, given an A_V, the different types of dust would have significantly different mid-infrared properties, and in particular, type-2 quasars with SMC-type dust will be more difficult to detect in a 24-μm survey than those with MW-dust. At $z \gtrsim 3$ the difference becomes small, but around $z \sim 1.5$ SMC-type dust has very deep silicate absorption feature which would make type-2s drop out of flux-limited surveys.

if the dust obscuring type-2s is more like the dust in the SMC than in the MW, then mid-infrared selection might perform slightly worse than expected from Figure 2.2. As mentioned in Section 2.1.2, the dust reddening of type-1 quasars has been found to be more similar to SMC-type dust, but that does not necessarily mean that the dust present in the obscuring torus is also SMC-type dust.

2.1.6 Orientation of the quasar

The analysis is mainly concerned with 24 μm selection of objects at $z \lesssim 5$, so we are seeing light reprocessed by dust in the torus at a range of temperatures, $T = 120 - 725$ K. We now use the results of a radiative transfer code by Granato & Danese (1994) to investigate the orientation dependence of observed 24-μm emission. In Figure 2.4 we quantify the fraction of the bolometric

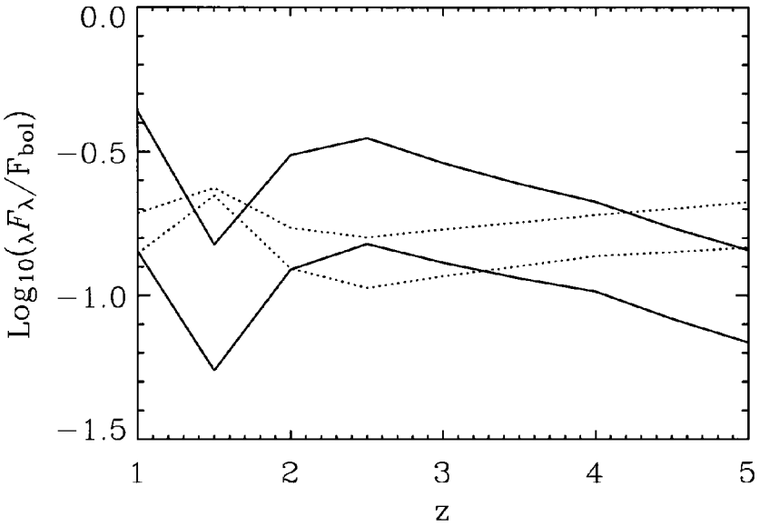

Figure 2.4: Estimate of λF_λ at $\lambda = 24\mu$m (observed) as a fraction of $F_{\rm bol}$ for two Granato & Danese (1994) models with the following parameters: the density has no radial dependence ($\beta = 0$), a covering fraction of 0.8, a ratio of outer radius $r_{\rm m}$ to inner radius of torus $r_{\rm o}$ (where $r_{\rm o} \sim 1$ pc), $r_{\rm m}/r_{\rm o} = 100$ (top two curves) and $r_{\rm m}/r_{\rm o} = 1000$ (bottom two curves). The equatorial optical depth at 0.3 μm, $\tau_{\rm e}$ is 80 (corresponding to $A_{\rm V} \approx 50$). The dotted line is for an AGN viewed pole-on (a type-1) while the solid line is for an edge-on view (type-2). The reason why the curves only have a few points is that the Granato & Danese (1994) models have few data points at the relevant range of wavelengths, and therefore further smoothing of the curves would be an overinterpretation. This shows that the 24-μm flux is roughly a constant fraction of $F_{\rm bol}$ between $2 \lesssim z \lesssim 4$ for both type-1 and type-2s. In this range of redshifts, 24-μm is therefore a good wavelength to select AGN independent of orientation. Once again we see the problems caused by the silicate absorption at $z \sim 1.5$. At very high redshifts ($z \gtrsim 4$), observed 24-μm is now a relatively short wavelength in the rest-frame, meaning obscuration by dust starts to have an increasingly large effect. The curves for both $r_{\rm m}/r_{\rm o}$ ratios are very similar, except for a normalisation, showing this argument holds for a range of torus sizes.

luminosity, $L_{\rm bol}$, seen at 24-μm as a function of redshift. For a pole-on unreddened source (necessarily a type-1), this fraction is approximately constant between $2 \lesssim z \lesssim 5$, while for an edge-on source (a type-2 with $A_{\rm V} \approx 50$), the fraction is similar to that of a type-1 and approximately constant in the range $2 \lesssim z \lesssim 4$. At higher values of z, the observed 24-μm corresponds to emitted wavelengths ($\lesssim 5\mu$m) at which the dust is becoming progressively more opaque. Around $z \sim 1.5$ the silicate feature is seen in emission by the type-1 and absorption by the type-2, so the observed 24-μm emission is not a very good indicator of $L_{\rm bol}$. We can therefore conclude that 24-μm is a good indicator of bolometric luminosity at $2 \lesssim z \lesssim 4$ and, as shown in Figure 2.4, this result is not strongly dependent on the assumed size of the torus.

2.1.7 Summary

To summarise, we have discussed the advantages of mid-infrared selection over hard X-ray selection. For gas-to-dust ratios similar to those found in the Milky Way, X-ray selection is superior, and can probe further down the luminosity function. However, many AGN have gas-to-dust ratios significantly larger than the MW. We have seen in this section how type-2 quasars with $N_{\rm H} = 5 \times 10^{26}$ m$^{-2} \times A_{\rm V}$ would naturally drop out of existing large-area X-ray samples without requiring extreme optical obscuration ($A_{\rm V} \gtrsim 20$ would be enough). We have seen that hard X-ray selected samples are in principle able to find even Compton-thick type-2s, but they require a combination of depth and area that is only just becoming available. We have also seen that dust-type is important, but mainly in the range $1 \lesssim z \lesssim 2$ (due to the 9.7-μm silicate absorption feature being more pronounced for certain dust types). Using the results of a radiative transfer code, we have also seen that (observed) 24-μm luminosity is a constant tracer of type-2 bolometric luminosity in the range $2 \lesssim z \lesssim 4$. Therefore, 24-μm selection is a natural starting place to look for the population of high-redshift type-2 quasars missing from X-ray surveys.

2.2 Selection Criteria

Our aim was to find the elusive high redshift type-2 population around the peak in the quasar activity, $z \gtrsim 2$ (e.g. Wolf et al., 2003), and for this we used the following selection criteria, which we explain in detail further down:

1. $S_{24\ \mu m} > 300\ \mu$Jy

2. $S_{3.6\ \mu m} \leq 45\ \mu$Jy

3. $350\ \mu\text{Jy} \leq S_{1.4\ \text{GHz}} \leq 2$ mJy

2.2.1 Datasets

The work described in this Chapter, and up to Chapter 5, was all done in the Spitzer Extragalactic First Look Survey (FLS). Three separate catalogues were cross-matched for the initial selection: the IRAC 3.6 μm (Lacy et al., 2005b) and the MIPS 24 μm (Marleau et al., 2004; Fadda et al., 2006) from the Spitzer First Look Survey and the 1.4 GHz catalogue from the NRAO VLA (Condon et al., 2003). The flux limits used for 3.6 μm, 24 μm and 1.4 GHz were 20, 300 and 100 μJy respectively.

Over the area with coverage in all three bands (3.8 deg^2), the radio and 24-μm catalogues were matched to select all sources detected at 24-μm and within the radio flux cuts. The chosen sources were then contrasted with the 3.6 μm catalogue, to obtain their flux densities in this IRAC channel. However, objects were not required to be detected at 3.6 μm to be kept in the candidate list. All matching was done with a 2.5 arcsec tolerance to allow for positional offsets between catalogues.

In addition, in Chapter 3 we use tabulate R-band magnitudes from data from the 4-m Mayall Telescope Kitt-Peak National Observatory (Fadda et al., 2004) and we also make use of a Westerbork Synthesis Radio Telescope deep survey at 1.4 GHz in the Spitzer First Look survey (Morganti et al., 2004). However, these two datasets were not used to select the candidate type-2 quasars.

2.2.2 Mid-infrared criteria

The mid-infrared criterion $S_{24\ \mu m} > 300\ \mu$Jy was chosen to select a flux-density-limited sample of active galaxies. At lower redshifts, a 24-μm selected sample would be dominated by starbursting galaxies, but combined with the 3.6-μm selection (which ensured high-redshift objects, see below), this 24-μm flux limit should yield powerful AGN. The $S_{24\ \mu m} > 300\ \mu$Jy criterion is the flux-density limit from a preliminary catalogue, and is actually a 7-σ limit in the 24-μm final catalogue from

the Spitzer FLS data (Marleau et al., 2004; Fadda et al., 2006). At $z = 2$, this corresponds to an emitted 8-μm luminosity $L_{8\ \mu\mathrm{m}} = 10^{24.4}$ W Hz^{-1}. Assuming a typical type-1 SED (Rowan-Robinson, 1995), this is $L_{\mathrm{B}} = 10^{23.2}$ W Hz^{-1} or $M_{\mathrm{B}} = -23.8$. At $z = 2$, the break in the quasar luminosity function, L^{*}_{quasar}, has a value of $M_{\mathrm{B}} = -25.7$ (Croom et al., 2004, with Pure Luminosity Evolution), so our 24-μm selection will select quasars $\gtrsim 0.2\ L^{*}_{quasar}$ at $z = 2$, and more luminous quasars at higher redshifts. As explained in Section 2.1, the selection becomes more complicated at $z < 2$ due to the silicate absorption, so we restrict our discussion to $z \geq 2$. The peak of the quasar activity occurred around $z \geq 2$ and by targeting the quasars around the "break" we are sensitive to the part of the population that contributes most of the luminosity density.

Quasars are considered as being type-2 if $A_{\mathrm{V}} \gtrsim 5$ (Simpson et al., 1999), and such an amount of extinction will make the observed near-infrared emission of type-2s much fainter than that of type-1s. The 3.6-μm criterion was therefore chosen to remove naked (type-1) quasars as well as lower redshift ($z \lesssim 1.4$) type-2s. At $z \geq 2$ the detected 3.6-μm flux density corresponds to light emitted at $\lambda \leq 1.2$ μm so dust extinction ensures that type-2 quasars are much fainter than type-1 quasars, even for a moderate A_V. Indeed, the $S_{3.6\mu\mathrm{m}}$ emission is likely to be dominated by starlight for $A_V \gtrsim 10$, and since light at 3.6-μm is dominated by the old stellar population, there will be an $S_{3.6\mu\mathrm{m}} - z$ correlation, analogous to the $K - z$ relation for radio galaxies (Jarvis et al., 2001a; Willott et al., 2003a). A typical host galaxy for a $z = 2$ radio-quiet quasar is the progenitor of a $\sim 2L^{*}_{gal}$ (Kukula et al., 2001) galaxy in the local Universe, so we adapt the $K - z$ relation (which corresponds to $\sim 3L^{*}_{gal}$ hosts for radio galaxies) to $\sim 2L^{*}_{gal}$ hosts at 3.6-μm. To do this, we use the models of Bruzual & Charlot (2003) to form an elliptical galaxy at $z = 10$, assign it a (stellar) mass and allow it to evolve passively. This allows us to predict the 3.6 μm flux as a function of redshift, for an elliptical galaxy of this given mass, and hence obtain a rough photometric redshift. The stellar mass of the galaxy was set to $3.8 \times 10^{11} M_{\odot}$. If we assume a Salpeter IMF (Salpeter, 1955) and take $M_{\mathrm{K}} = -24.3$ from the fitting of Schechter functions by Cole et al. (2001), then our assumed stellar mass translates to a $2.6L^{*}_{gal}$ galaxy. This is the host (elliptical) galaxy luminosity assumed to obtain the rough photometric redshifts in Chapters 3 and 4 and Martínez-Sansigre et al. (2005, 2006) and in this Chapter. The criterion $S_{3.6\ \mu\mathrm{m}} \leq 45$ μJy corresponds to a limiting photometric redshift $z_{\mathrm{phot}} \gtrsim 1.4$. This was chosen to target $z \sim 2$ type-2

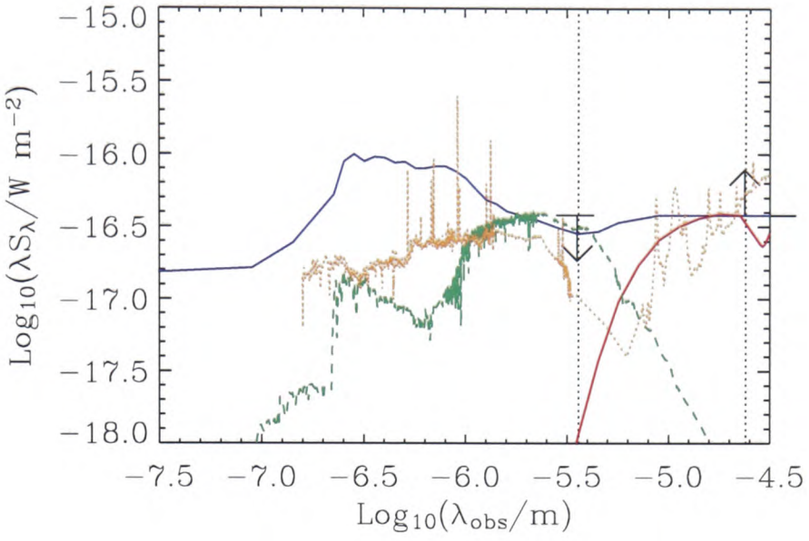

Figure 2.5: Mid-infrared selection criteria plotted on observed spectral energy distributions (SED). The 24-μm criterion is shown as a lower limit, and the 3.6-μm criterion as an upper limit. The solid lines represent quasars at $z = 2$ bright enough to make the 24-μm flux cut. The upper blue solid line is a type-1 quasar (SED from Rowan-Robinson, 1995), while the lower red solid line is a type-2 with $A_V = 5$. A type-1 quasar just bright enough to make the 24-μm cut will be too bright at 3.6 μm (once the host galaxy contribution is added). The dashed green SED represents a $2.6L^*$ elliptical galaxy at $z = 1.4$ (from Bruzual & Charlot, 2003), where it becomes just faint enough to make it fall below the 3.6-μm cut. The dotted yellow line is the ULIRG NGC 7714 redshifted to $z = 0.4$ (SED from Brandl et al., 2004), which would meet our mid-infrared criteria if it lay between $z = 0.25$ and $z = 0.4$.

quasars, while allowing for scatter in the crude photometric redshift estimation and filtering out type-1 quasars and low-redshift contaminants like radio galaxies.

The combination of these criteria is illustrated in Figure 2.5. It shows the observed spectral energy distributions of two $z = 2$ quasars (model from Rowan-Robinson, 1995), a type-1 and a type-2 (the latter obscured by $A_V = 5$, dust model from Pei, 1992). A $2.6L^*$ elliptical galaxy from Bruzual & Charlot (2003) is also plotted at $z = 1.4$, showing how the 3.6-μm criterion serves also as a crude photometric redshift cut.

2.2.3 Radio criterion

The radio selection criteria is added to ensure that the candidates are quasars rather than starburst galaxies. The 3.6-μm - 24-μm "colour" demanded by our criteria can be achieved by lower redshift

($z < 1$) ultra luminous infrared galaxies (ULIRGs). For example, NGC 7714 would satisify these criteria if it were at $z = 0.25 - 0.4$ (see Figure 2.5, SED from Brandl et al., 2004) and the more luminous ULIRG Arp 220 if it where at $z = 0.5 - 0.7$. In the absence of AGN radio activity, the radio flux densities of such objects would follow the far-IR/radio correlation (Condon, 1992), and hence would have values of $S_{1.4\ \mathrm{GH}} \sim 50$ μJy (for ULIRGs at $z \sim 0.3$) and 500 μJy (for more powerful ULIRGs at $z \sim 0.6$).

To avoid such starburst contaminants, we chose a lower limit on $S_{1.4\ \mathrm{GHz}}$ which also excludes higher-redshift (submillimetre-selected) starburst galaxies without the benefit of strong gravitational lensing (e.g. Chapman et al., 2005). For a $z \sim 0.6$ ULIRG to have $S_{1.4\ \mathrm{GH}} \geq 350$ μJy, it would require a far-infrared luminosity of $L_{\mathrm{FIR}} \gtrsim 1 \times 10^{12}\ L_{\odot}$. Objects with this far-infrared luminosity are rare in space-density (Sanders & Mirabel, 1996), and the comoving volume probed at $z \sim 0.6$ by 3.8 deg^2 is such that $\lesssim 1$ contaminants would be expected in our sample.

An upper limit on $S_{1.4\ \mathrm{GHz}}$ was also used to filter out the radio-loud objects, whose extended jets might complicate interpretation. The radio flux-density cut introduced here will select the radio-bright end of the radio-quiet quasar population (Cirasuolo et al., 2003), so these objects can be described as radio-intermediate (e.g. Miller et al., 1993). In addition, the $S_{3.6\mu\mathrm{m}}$ criterion includes objects without IRAC detections which we expect to have the highest redshifts. Since the 24-μm positions are accurate to ~ 1 arcsec, the FLS radio positions (Condon et al., 2003), accurate to ~ 0.5 arcsec, were also better for spectrosocopic follow-up.

The two simple infrared criteria together with radio selection were chosen over an IRAC colour requirement because the latter criterion would have selected type-2s with a narrow range in A_{V} and z. Our three criteria represent a simple way of selecting type-2 quasars and allow the modelling necessary to estimate the quasar fraction at high redshift (see Chapter 4).

Figure 2.6 shows an additional diagrammatic representation of the infrared selection criteria. Note that all objects plotted needed to meet the criteria on radio flux density. At all redshifts, any type-1 ($A_V < 5$) quasar bright enough to make the $S_{24\mu\mathrm{m}} > 300$ μJy criterion will also be too bright at 3.6-μm to make it into our sample. At $z = 1$, an L^*_{quasar} quasar would be able to make it through the criteria if it has $A_{\mathrm{V}} \gtrsim 20$, but then the 3.6-$\mu$m light would be dominated by the elliptical galaxy, which at $z = 1$ would be too bright to make it to the sample. At $z = 2$ an L^*_{quasar} quasar with $A_{\mathrm{V}} \gtrsim 5$ would be bright enough at 24 μm and faint enough at 3.6 μm to make

it to the sample. If, in addition, it had $A_V \gtrsim 10$, the 3.6 μm light would be dominated by the host galaxy. At $z = 2$ an elliptical host galaxy would indeed be faint enough to make the 3.6-μm cut, and assuming the host galaxy to be typically a $\sim 2L^*_{gal}$, the 3.6-μm flux density provides us with a crude photometric redshift.

As a word of caution, the above discussion has assumed all quasars to have a typical SED (e.g. Elvis et al., 1994; Rowan-Robinson, 1995). The variance in the Elvis et al. (1994) sample is large, showing that quasars have a range of intrinsic spectral shapes.

Type-1 quasars which have a spectral shape which is intrinsically brighter in the near- and mid-infrared than in the optical and UV, compared to this assumed median SED, could possibly get through our selection criteria, even if they have moderate obscuration due to dust ($A_V < 5$). At higher redshifts ($z \sim 3$), quasars that are best described as reddened ($A_V \sim 1 - 5$) might also get through, since we are probing longer rest-frame wavelengths, where the effect of dust increases. The dust extinction curve of the quasars can also be different to those considered here, although this is expected to have a small effect. Finally our parametrisation of obscured quasars as type-1s with a screen of dust is a good approximation at optical wavelengths (where the light originates from a different region to where the dust lies) but not necessarily at mid-infrared wavelengths. Alternatively, one could use a radiative transfer code to correctly model the SED of obscured quasars. However, this would be even more model-dependent, and until large samples of observed type-2 quasar SEDs are available, the models will remain poorly constrained.

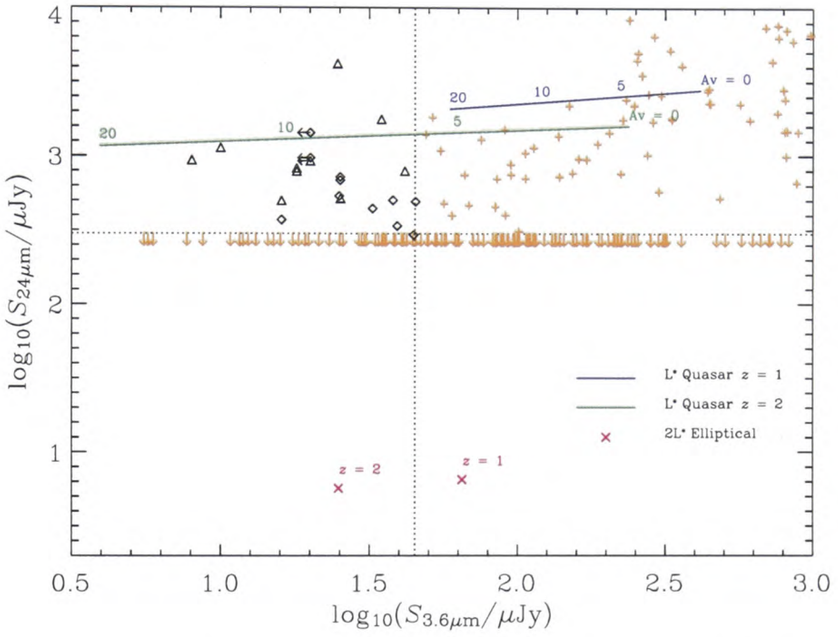

Figure 2.6: Log_{10}(24 μm flux density $S_{24\mu m}$ / μJy) plotted against $\log_{10}$(3.6 μm flux density $S_{3.6\mu m}$/ μJy). The dotted lines represent the flux density cuts of our selection criteria. The parent population is plotted as orange crosses, or arrows when $S_{24\mu m}$ is an upper limit. Our 21 candidates, described in detail in Chapter 3, are plotted in the top left corner, with black triangles for candidates with a spectroscopic redshift and black diamonds for candidates without one (See Chapter 3). Horizontal arrows represent upper limits for $S_{3.6\mu m}$. None of the candidates showed type-1 quasar spectra. The magenta crosses show $S_{24\mu m}$ and $S_{3.6\mu m}$ for a $2L^*_{gal}$ elliptical galaxy at $z = 1$ and $z = 2$; starlight is assumed to evolve passively following the stellar population synthesis models of Bruzual & Charlot (2003). The other colours represent an L^*_{quasar} quasar (spectral energy distribution from Rowan-Robinson, 1995) with varying amounts of visual extinction A_V applied to $S_{24\mu m}$ and $S_{3.6\mu m}$ and plotted on the curves (assuming a Milky-Way-like extinction curve from Pei, 1992); these are plotted at two different redshifts, and the quasar population is assumed to undergo pure luminosity evolution (Croom et al., 2004).

Chapter 3

A population of high-redshift obscured quasars

After the selection criteria described in Chapter 2, we were left with 21 candidate high-redshift type-2 quasars in the Spitzer First Look Survey (see Table 3.1 and Figure 2.6), which were followed up spectroscopically (as described in Section 3.1). Note that all our candidates were originally selected from the preliminary 3.6 and 24 μm catalogues, but have had their fluxes slightly revised and the flux densities quoted are the final ones. This explains why two candidates are slightly outside the selection boundaries (see Figure 2.6). We also note that although the R-band (Vega) magnitudes are not part of our selection criteria, they are consistent with optically obscured quasars in high-redshift host galaxies. At $z = 1.4$, our model elliptical galaxy would have $m_{\rm R} = 23.3$.

3.1 Observations and Data Reduction

The 21 candidates were observed with both arms of the ISIS instrument at the William Herschel Telescope in July 2004 and April 2005 (see Table 3.2). Low-resolution long slit spectroscopy was performed across the entire visible band (3200 Å to 9300 Å) using the gratings R158B and R158R, and the EEV12 and Marconi detectors. The 6100 Å dichroic was used in July 2004, while in April 2005 we used the new 5300 Å dichroic. Using slit widths of 1.5-2.0 arcsec, we obtained (for sources filling the slit) spectral resolutions of 12-16 Å in both arms. Bias, flat, arc, sky-flat and

standard-star frames were all taken at the beginning and end of the night to ensure reasonable calibration.

The slit was placed on the radio positions, without optical identification, by "blindly" offsetting from a nearby guide star (e.g. Rawlings et al., 1990). Whenever another radio source was in the field, the slit angle was chosen to go through the source as well as our candidate. When no other radio sources were available, bright sources from the IRAC 3.6-μm catalogue were placed in the slit. This ensured multiple objects were detected in the slit, improving the astrometry and identification of our sources in the 2-D spectra. At high airmasses ($\sim 1.4 - 1.5$) we observed the objects with slit position angles (PAs) close to the parallactic angle, to minimise atmospheric dispersion of the blue light. Each object was observed for 30 minutes with a 1-2 arcsec slit width, with one 1800 second exposure in the blue arm and two 900 second exposures in the red arm.

The spectra were all reduced using the IRAF package TWODSPEC LONGSLIT. The wavelength calibration was performed using CuAr+CuNe lamps and flux calibration was obtained from appropriate spectrophotometric stars. The two red frames for each object were reduced separately and then combined to remove cosmic rays. The 1D spectra were extracted separately for the blue and the combined red frames, using the task APSUM. The resulting one-and two-dimensional spectra are plotted in Figure 3.2. For the two-dimensional spectra, the pixel scale is 4.8 Å pixel^{-1} for all objects except AMS04 and AMS13, where the scale is 3.2 Å pixel^{-1}.

AMS01 The 3.6 μm image of this object shows it to be visible, although possibly confused with a galaxy just to the North (N) of it (see Figure 3.1). However, in the R-band image we see our target is distinguishable as an extremely faint galaxy. The two images clearly show the very red colour of AMS01. There was another radio source of similar flux East (E) of AMS01 and so a position angle (PA) of 103 degrees was chosen to go through both sources. The spectrum of AMS01 was completely blank in a 30-minute exposure..

AMS02 In this case, our target is clearly visible in the IRAC image, but is only just detected in the R-band. The PA was chosen to go through another radio source, 45 arcsec SE of AMS02. The spectrum of our target was once again completely blank in a 30-minute exposure.

AMS03 Here we see another possible source of confusion in the 3.6 μm image, but the R-band image shows our source to be very faint but distinct from the brighter source SW of it. There is a nearby radio source which is confused in the WSRT images (see Section 3.5). Here the PA

was chosen to go through this other radio source 18 arcsec E-SE of AMS03. The two-dimensional spectrum shows a faint, double, spatially-extended line ($\sim$ 1.6 arcsec once deconvolved from the seeing), which we identify as Ly α (the redward line is not N V). The spectrum shows quite a lot of structure (see Figure 3.2): there are two Ly-α lines, one at 4481 Å and the other at 4512 Å. The redward line has a full-width half maximum (FWHM) of $\sim$ 500 km s^{-1}, while the blueward line has a hint of absorption in the spatial centre, and has a greater FWHM ($\sim$ 1400 km s^{-1}) but still narrow enough to qualify as a type-2 quasar. A possible interpretation is that the type-2 quasar resides in a Ly-α halo, and there is a large difference in systemic velocity for the quasar and the halo (or the halo is collapsing, leading to a different redshift). Another possibility is associated absorption - this is present in small radio sources (van Ojik et al., 1997).

AMS04 This object is very faint at 3.6 μm (18 μJy) but reasonably bright in R-band ($m_{\rm R}$ =23). The radio emission around AMS04 is extended towards the NE. There is another distant radio source, identified at both 3.6 μm and R-band further to the east. This is possibly associated with another extremely faint galaxy about 10 arcsec away, although the radio and optical positions of the adjacent radio source and the faint galaxy do not match perfectly. We placed the slit to go through both AMS04 and the other radio source. AMS04 shows strong continuum, a spatially extended (and bright) Ly α as well as C III], N II] and C II] lines but nothing was seen associated with the extended radio emission. The Ly α line has an angular size of $\sim$ 5.5 arcsec. This object has a redshift of 1.782, with all the redshifts from individual lines agreeing well (see Table 3.3). The fact that this object is not that faint in R-band is due to the continuum and narrow-lines at the red end of the spectrum.

AMS05 Here we see again a source which is relatively bright at 3.6 μm (34 μJy) compared to R-band ($m_{\rm R}$ =25.2). The IRAC image is quite crowded and there is the danger of confusing sources, but we can see in the R-band that the radio position falls on a faint galaxy. This object showed an interesting spectrum: C IV is actually as strong as Ly α, and He II is also detected, but there is no continuum in the blue or red arm. All lines are unresolved, and the weakness of the Ly α may be due to it falling in the blue end of the spectrum while having been observed at a relatively high airmass (see Table 1) and away from the parallactic angle.

AMS06 This target is just about visible in the 3.6 μm images, but it is not bright enough to make it to the IRAC catalogue. It is undetected in the R-band. A PA of 120°was chosen to go

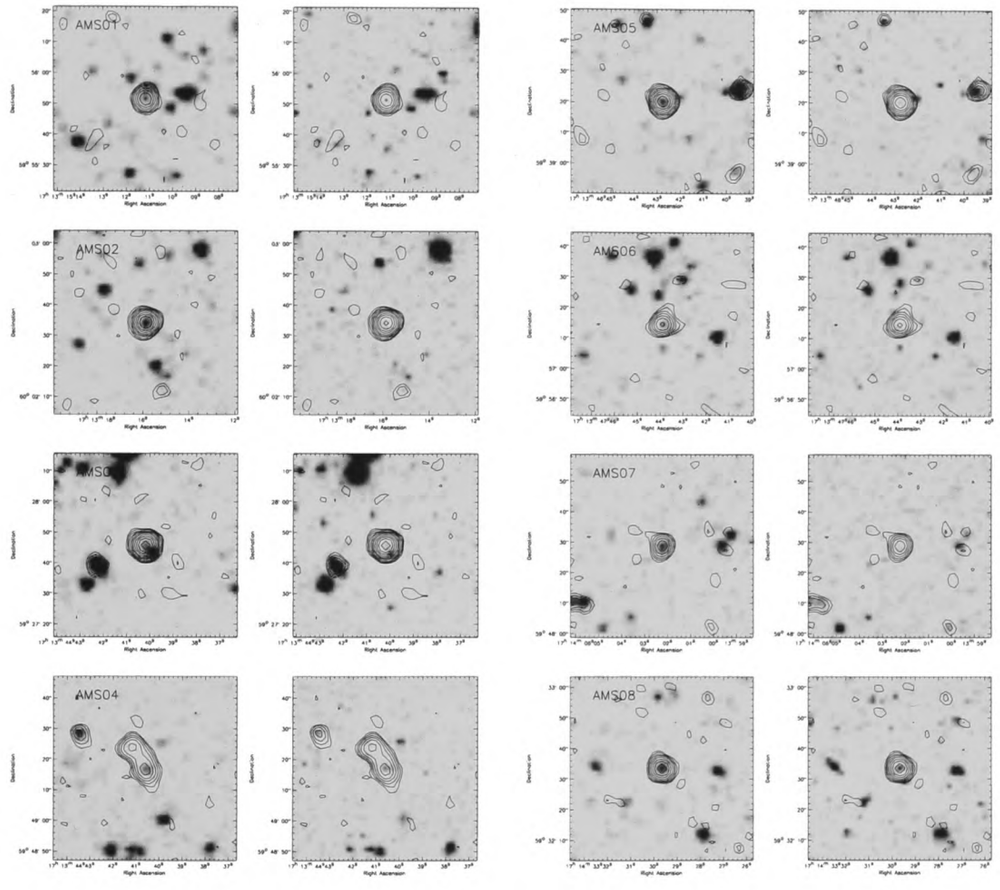

Figure 3.1: Radio contours overlayed over the 3.6-μm and R-band images for the sample (images from Condon et al., 2003; Fadda et al., 2004; Lacy et al., 2005b). In each pair of overlays, the 3.6-μm image is on the left (with the name of the source) and the R-band on the right. Radio contours are plotted at -2σ,2σ and subsequently at $2^{n/2}\sigma$ up to $2^6\sigma$, where σ is the rms noise of the radio image ($\approx$ 23 μJy). The gray scale has been chosen to overcome the high dynamical range and highlight faint objects. Faint grey pixels have values 3-times that of the noise.

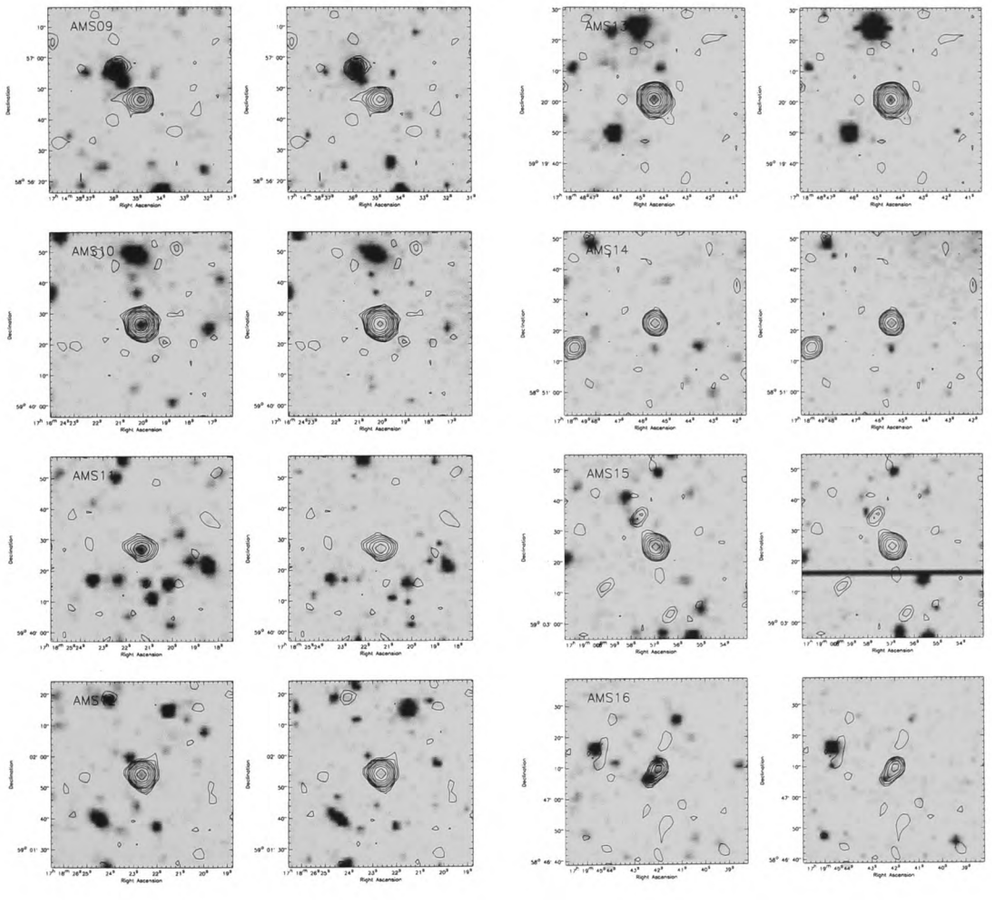

Figure 3.1: Continued

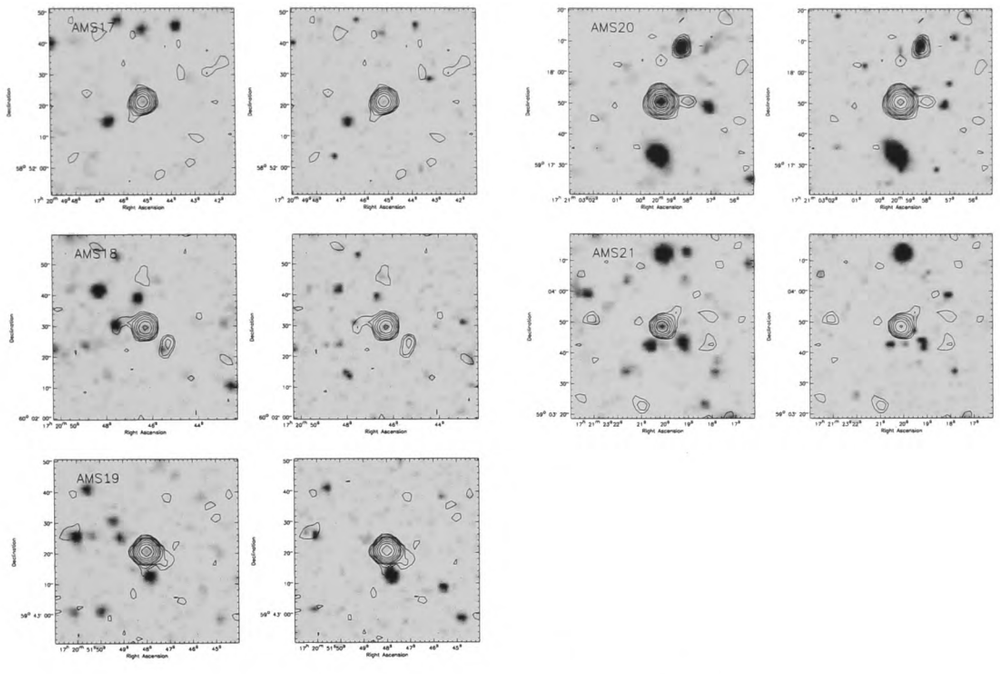

Figure 3.1: Continued

through the "semi-major axis" of the marginally-resolved radio source. The spectrum was blank at the location of the target source. This could be due to the entire galaxy being very dusty and therefore faint in the optical and even the infrared (see the discussion in Chapter 4) or it could be a very high redshift source. Recently a redshift of 1.76 has been obtained from silicate absorption and PAH emission with Spitzer IRS (Weedman et al., 2006), confirming this is a very dusty system at high redshift.

AMS07 AMS07 is quite a red object (within our sample) in that the 3.6 μm is relatively bright, whereas the R-band is very faint. There is another radio source 56 arcsec SW of the target, so the slit (with PA 19°) was made to go through both radio sources. The spectrum was blank at the target position.

AMS08 Here we have a relatively bright source for our sample, both in the IRAC and R bands. A faint (slightly extended) radio source, 18 arcsec SE of our source, was visible in the radio images. The slit was made to go through both this source and our target. AMS08 appears in the spectrum, showing Ly α ($\sim$ 3.7 arcsec wide after deconvolving from the seeing), C IV and He II and blue continuum.

AMS09 This is a faint source at 3.6 μm and is undetected in R-band. The 3.6 μm image shows

Name	RA (J2000)	Dec	$S_{24\mu m}$ / μJy	$S_{1.4GHz}$ / μJy	$S_{3.6\mu m}$ / μJy	$S_{4.5\mu m}$ /μJy	m_R	z_{phot}	z_{spec}
AMS01	17 13 11.17	+59 55 51.5	536	490	25.0	30.0	25.1	2.1	
AMS02	17 13 15.88	+60 02 34.2	294	1184	44.5	61.0	25.3	1.4	
AMS03	17 13 40.19	+59 27 45.8	500	1986	16.0	28.0	24.4	3.1	2.698[1]
AMS04	17 13 40.62	+59 49 17.1	828	536	18.0	22.0	22.96	2.8	1.782
AMS05	17 13 42.77	+59 39 20.2	1769	1038	34.7	61.4	25.2	1.7	2.017
AMS06	17 13 43.91	+59 57 14.6	969	444	<20	<25	≥25.3	≥2.5	1.76[2]
AMS07	17 14 02.25	+59 48 28.8	503	354	37.9	47.8	24.7	1.5	
AMS08	17 14 29.67	+59 32 33.5	792	655	41.6	46.3	22.48	1.4	1.979
AMS09	17 14 34.87	+58 56 46.4	685	426	25.2	<25	≥25.3	2.1	
AMS10	17 16 20.08	+59 40 26.5	338	1645	39.2	44.7	24.1	1.5	
AMS11	17 18 21.33	+59 40 27.1	442	356	32.4	55.6	24.7	1.7	
AMS12	17 18 22.65	+59 01 54.3	518	946	25.24	<25	23.77	2.0	2.767
AMS13	17 18 44.40	+59 20 00.8	4196	1888	24.7	49.1	22.89	2.1	1.974[3]
AMS14	17 18 45.47	+58 51 22.5	937	469	8.0	15.0	23.67	4.6	1.794
AMS15	17 18 56.93	+59 03 25.0	371	440	16.0	16.0	≥25.3	3.0	N.O.[4]
AMS16	17 19 42.07	+58 47 08.9	788	390	18.0	21.0	23.07	2.8	4.169
AMS17	17 20 45.17	+58 52 21.3	1134	615	10.0	15.0	23.80	3.9	3.137[1]
AMS18	17 20 46.32	+60 02 29.6	925	390	<20	<25	23.53	≥2.5	1.017
AMS19	17 20 48.00	+59 43 20.7	1433	822	<20	26.9	≥25.3	≥2.5	2.25[2]
AMS20	17 20 59.10	+59 17 50.5	492	1268	45.2	64.9	23.80	1.4	[5]
AMS21	17 21 20.09	+59 03 48.6	720	449	25.2	38.6	24.2	2.1	

Table 3.1: Basic data on the 21 type-2 quasars in our sample. The J2000.0 positions are from the Spitzer FLS radio catalogue (Condon et al., 2003). The MIPS 24-μm flux density $S_{24\mu m}$ is obtained by point spread function (PSF) fitting (Marleau et al., 2004) as all objects (except AMS16) are point sources at the $\sim$ 6 arcsecond resolution of the MIPS observations, with positional errors $\sim$ 1 arcsecond. It has a typical error of $\pm 10 - 15\%$. The 1.4-GHz flux density is the integrated value (in μJy per beam) from the radio catalogue. The IRAC 3.6- and 4.5-μm flux densities are measured in 5-arcsec-diameter apertures (Lacy et al., 2005b) and have typical errors of $\pm 10\%$. The R-band magnitudes are measured using a 3-arcsecond diameter aperture from the images of the 4-m Mayall Telescope Kitt-Peak National Observatory (Fadda et al., 2004), with typical errors of 0.03 for objects with magnitude 22-23, 0.10 for objects with 23-24 and 0.25 mags for those with magnitudes of 25. [1] These objects have redshifts identified from a single line, which we identified as Lyman-α: in AMS03, from the amount of structure in the line, and in AMS17 from the fainter continuum blueward of the line. [2] These two objects have redshifts from Spitzer-IRS spectroscopy from Weedman et al. (2006), who give two values for the redshifts. Here we show the mean of the two values. [3] This object was observed with Spitzer-IRS by Yan et al. (2005) who measured a redshift of $z = 2.1 \pm 0.1$ in good agreement with our value. [4] As explained in Table 3.2, AMS15 has not really been observed spectroscopically.[5] AMS20 shows faint red continuum but no emission lines. Note there were errors in the redshifts of AMS14 and AMS18 presented in Table 1 of Martínez-Sansigre et al. (2005) and these have been corrected here, together with minor corrections to several other redshifts.

only one infrared ID for our radio source, but the R-band image shows there might be a serious confusion issue, as there are several faint sources near the radio position. There were two other radio sources in the field, one close to the N (visible in Figure 3.1) and one E. We chose to place the slit through the eastern radio source (41 arcsec away) and the PA angle (119 deg) is actually appropriate to try and catch several of the possible optical IDs. There is barely a hint of continuum from AMS09 in the red two-dimensional spectrum and no hint of the other source.

AMS10 AMS10 is a relatively bright source in the IRAC bands, and has $m_{\rm R}$ =24.1. The 3.6 μm source is actually confusing two R-band sources, but the radio position is clearly associated to only one of the R-band galaxies. There were no other radio sources in the field, so we chose the PA to match the parallactic angle. The 2D spectrum of AMS10 is blank.

AMS11 This is another quite red source, relatively bright at 3.6 μm and faint in R-band. There are no other radio sources near but the radio emission seems to be slightly extended in the E direction, so we chose the PA so the slit would go through it. AMS11 was not detected by ISIS.

AMS12 Here we have a faint source in all bands. The PA was chosen to go through a radio source 50 arcsec SE of our target. The spectrum of AMS12 shows several emission lines: Ly α (spatially unresolved), C IV and He II (see Table 3.3) and faint continuum.

AMS13 AMS13 is a point-like radio source, and is quite faint at 3.6 μm, so we matched the PA to the parallactic to minimise dispersion of the blue light (even though the airmass, 1.16, was not particularly high). In the 2D spectrum, however, it is very bright, showing spatially extended Ly α and C IV lines ($\sim$ 4.3 and 3.5 arcsec wide respectively) as well as continuum. The continuum explains why it is not that faint in the R-band. The optical spectra show AMS13 is at a redshift of 1.974, and Yan et al. (2005) find a redshift of 2.1 $\pm$ 0.1 from the silicate absorption feature in their Spitzer-IRS spectroscopy, in agreement with our redshift.

AMS14 This source is extremely faint in the IRAC bands (8 μJy at 3.6 μm) making us expect this to be a very high redshift source. A PA of 105°was chosen to go through another faint radio source 10 arcsec E of our target. The spectrum, however, shows a very strong (and spatially resolved) Ly α line ($\sim$ 1.6 arcsec wide) as well as C IV at a redshift of z = 1.794. A mistake in an early wavelength calibration led us to mis-identify the lines and the redshift reported in Martínez-Sansigre et al. (2005) is incorrect.

AMS15 This is another very faint source at 3.6 μm and undetected in R-band. This is a good

Name	RA (J2000)	Dec	Date Observed	Airmass	PA /deg	Slit /arcsec
AMS01	17 13 11.17	+59 55 51.5	15/07/04	1.17	103	1.5
AMS02	17 13 15.88	+60 02 34.2	14/07/04	1.37	149	2.0
AMS03	17 13 40.19	+59 27 45.8	14/07/04	1.17	114	1.5
AMS04	17 13 40.62	+59 49 17.1	14/04/05	1.18	36	2.0
AMS05	17 13 42.77	+59 39 20.2	14/07/04	1.47/1.56[1]	98	2.0
AMS06	17 13 43.91	+59 57 14.6	13/07/04	1.19	120	2.0
AMS07	17 14 02.25	+59 48 28.8	16/07/04	1.22	19	1.5
AMS08	17 14 29.67	+59 32 33.5	15/07/04	1.32	128	1.5
AMS09	17 14 34.87	+58 56 46.4	15/07/04	1.17	111	1.5
AMS10	17 16 20.08	+59 40 26.5	14/07/04	1.20	114	1.5
AMS11	17 18 21.33	+59 40 27.1	16/07/04	1.19	76	1.0
AMS12	17 18 22.65	+59 01 54.3	15/07/04	1.16	150	1.5
AMS13	17 18 44.40	+59 20 00.8	14/04/05	1.16	186	2.0
AMS14	17 18 45.47	+58 51 22.5	13/07/04	1.20	105	2.0
AMS15	17 18 56.93	+59 03 25.0	15/04/05[2]	-	-	-
AMS16	17 19 42.07	+58 47 08.9	16/07/04	1.25	141	2.0
AMS17	17 20 45.17	+58 52 21.3	15/04/05	1.27	117	1.5
AMS18	17 20 46.32	+60 02 29.6	13/07/04	1.40	133	2.0
AMS19	17 20 48.00	+59 43 20.7	14-15/04/05	1.17/1.17	170/185	2.0
AMS20	17 20 59.10	+59 17 50.5	14/07/04	1.22	160	2.0
AMS21	17 21 20.09	+59 03 48.6	15/04/05	1.20	84	1.5

Table 3.2: Summary of the spectroscopic observations. Most of the objects were observed in July 2004, and the spectroscopy was completed in April 2005. The objects were all observed with airmass < 1.5 (except AMS05), with good seeing (in the range 0.7-1.0 arcsec). As described in Section 3.1, the position angles (PAs) of the slit were generally chosen to go through any other radio source in the field, or any bright 3.6 μm source, to help the astrometry and identification. In some cases neither were available, or the airmass was high, so the PA was chosen to match the parallactic angle and therefore minimise dispersion of the blue light. [1]AMS05 was observed twice on the same night, at different airmasses. [2]AMS15 was targetted in April 2005, but the position used was slightly wrong (~ 0.8 arcsec) and therefore we do not consider it to have been observed.

candidate for a high-redshift type-2 quasar. However we used a slightly wrong position (the one published in Martínez-Sansigre et al. (2005) is off by ~0.8 arcsec) for follow-up spectroscopy. For this reason we do not consider this object to have been observed.

AMS16 AMS16 is very faint in the IRAC bands, although it is not extremely faint in R-band ($m_{\rm R} = 23.07$). It has an extended radio structure, whose central position matches the optical and IR positions. However, the extended emission matches two galaxies next to the source very well, and in the 24-μm image the three sources are confused, and have a similar structure to the radio emission. There is the possibility that the two foreground galaxies might be lensing AMS16 (see Figure 3.1). Two factors therefore influenced the choice of PA in this case. First, the radio emission around AMS16 is extended in the SE to NW direction (diagonally, possibly due to the two galaxies). In addition, there is a radio loud ($S_{1.4\ \rm GHz}$ =21.6 mJy) type-1 quasar about an arcmin NW. By good fortune, the same angle is required to get the slit through the 'semi-major axis' of the extended radio emission, the brighter foreground galaxy and the type-1 quasar. We found Ly α (~ 2.7 arcsec), N V (~ 1 arcsec) and C IV (spatially unresolved) in AMS16, indicating a redshift of $z = 4.169$. The emission lines of AMS16 are all strong, which explains why it is not that faint in the R-band. To the NW of AMS16, 58 arcsec away, we found a radio-loud type-1 quasar, at redshift $z = 3.785$ (see Figure 3.3).

AMS17 This is another faint source in the IRAC bands, suggesting a high redshift, although the R-band is not particularly faint for this sample, and the images show the optical/IR positions match perfectly the centre of the radio emission, with no possible sources of confusion nearby. The slit PA was chosen to go through another object, about 59 arcsec SE of our target. AMS17 is indeed at high-redshift, as it shows one narrow line in the blue spectrum (which we identify as Ly α at $z = 3.137$) and faint continuum redwards of the line. The Ly α line is extended ~ 1.6 arcsec wide in the spatial direction, once the seeing is deconvolved.

AMS18 Here is a source which is undetected in the IRAC catalogues, which suggests a high redshift. The PA was chosen to go through a bright radio source 57 arcsec South-East. The 2D spectrum shows AMS18 has several faint emission lines, which we identify as C II], Mg II and [O II] at $z = 1.017$, so it is at a lower redshift than first expected from the crude photometric redshift. Note the weakness of the [O II] line, which suggests a faint AGN rather than something similar to a radio galaxy. The same wavelength calibration error discussed for AMS14 led to the

redshift of AMS18 being incorrect in Martínez-Sansigre et al. (2005). The lack of high-ionization lines suggests this could plausibly be a ULIRG contaminant, which is how it made it through our selection criteria. It is however, difficult to judge whether the lines are spatially extended, due to the low SNR.

AMS19 The PA was chosen to be identical to the parallactic angle, as it is very faint in the near-infrared and the radio emission of AMS19 is point-like. This could mean a high redshift, so we tried to maximise the blue light received. Indeed, in the two-dimensional AMS19 does not even show faint continuum. However it was also observed by Weedman et al. (2006) with Spitzer IRS and is found to be at $z = 2.25$ from PAH and Silicate features.

AMS20 This is a relatively bright source for our sample, and so is not expected to lie at a particularly high redshift. The slit was placed at an angle so it would go through two fainter radio sources NW of AMS20 (19 and 55 arcsec away). The spectrum of AMS20 shows faint red continuum but no lines to allow us to obtain a redshift. Further study is required to determine whether this is a very bright high-redshift type-2, or more similar to AMS18, a faint, lower-redshift object. The lack of lines suggests $z \sim 1.3 - 1.6$.

AMS21 The last source in our sample is relatively faint in at 3.6 μm and R-band. In this case, the PA was chosen to go through a fainter radio source about 25 arcsec E of the target. However, neither AMS21 or the other radio source have been detected in the optical spectrum.

3.2 Type-2 Spectra

Approximately half of the objects (10 out of 21) showed narrow emission lines and sometimes continuum (see Figure 3.2). Ly α with full-width half maximum (FWHM) $\lesssim 2000$ km s^{-1} was found in nine objects (with a redshift range $1.78 \leq z \leq 4.17$) and high excitation lines such as C IV (1549 Å) or He II (1640 Å) were also found in several objects (C IV is present in 6 objects; see Table 3.3). In two cases (AMS03 and AMS17) we only found one emission line, which was taken to be Ly α by virtue of its extreme rest-frame equivalent width (-203 Å and -320 Å respectively), blue-absorbed line profile and lack of other lines supportive of alternative identifications. The Ly α line of AMS03 is particularly spatially-extended. One object, AMS18, proved to be at $z = 1.02$, lower than expected from our selection criteria. AMS18 could still be an AGN (but it

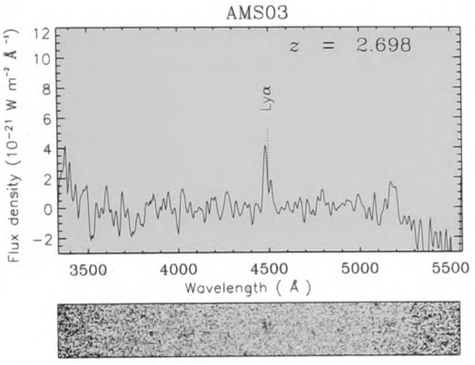
AMS03
z = 2.698
Lyα
Flux density (10⁻²¹ W m⁻² Å⁻¹)
Wavelength (Å)

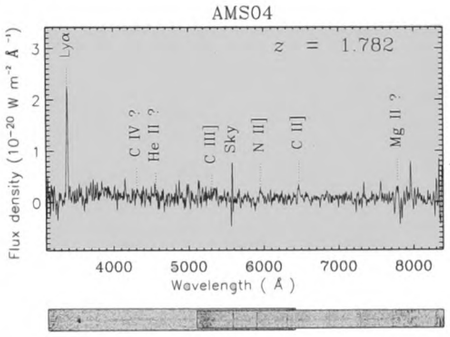
AMS04
z = 1.782
Lyα
C IV ?
He II ?
C III]
Sky
N II]
C II]
Mg II ?
Flux density (10⁻²⁰ W m⁻² Å⁻¹)
Wavelength (Å)

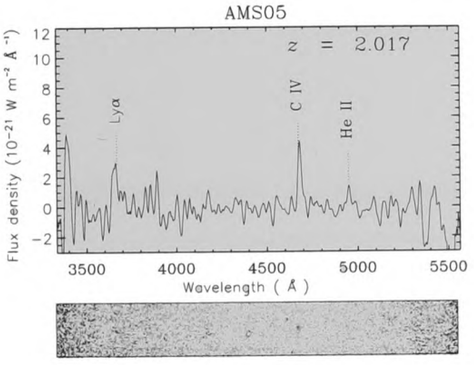
AMS05
z = 2.017
Lyα
C IV
He II
Flux density (10⁻²¹ W m⁻² Å⁻¹)
Wavelength (Å)

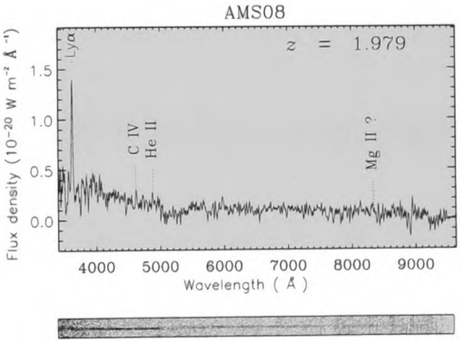
AMS08
z = 1.979
Lyα
C IV
He II
Mg II ?
Flux density (10⁻²⁰ W m⁻² Å⁻¹)
Wavelength (Å)

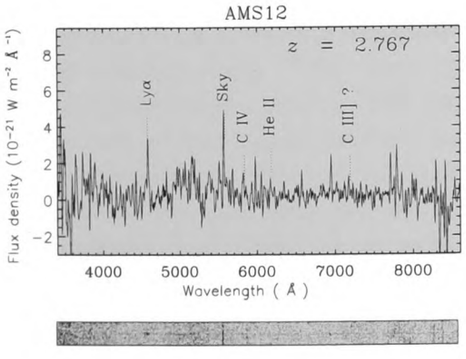
AMS12
z = 2.767
Lyα
Sky
C IV
He II
C III] ?
Flux density (10⁻²¹ W m⁻² Å⁻¹)
Wavelength (Å)

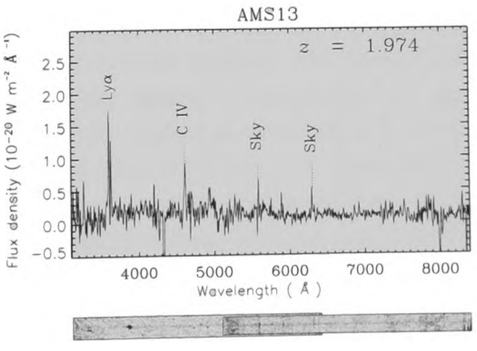
AMS13
z = 1.974
Lyα
C IV
Sky
Sky
Flux density (10⁻²⁰ W m⁻² Å⁻¹)
Wavelength (Å)

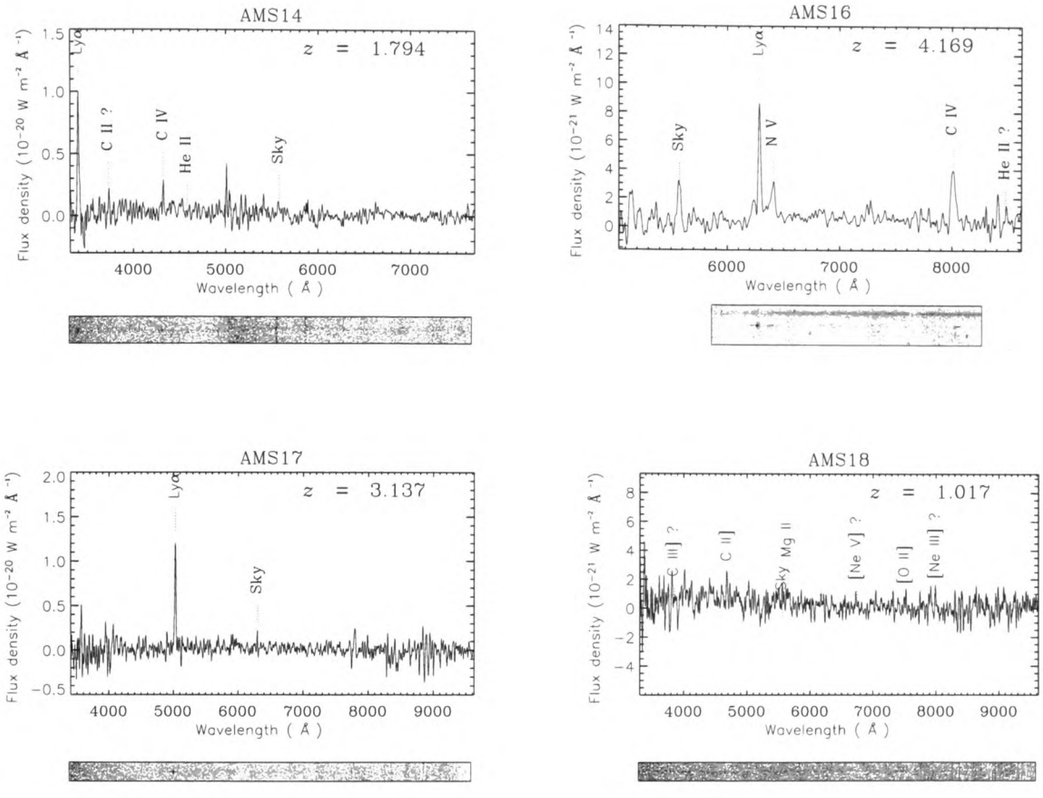

Figure 3.2: Optical spectra of objects in the sample which showed emission lines. The emission lines from which the redshifts were obtained are labelled, while tentative identifications of lines which have not used for the redshifts are labelled with a question mark. The corresponding two-dimensional spectra are shown underneath the one-dimensional ones as a visual help to find the emission lines. They have approximately the same scale in the horizontal direction as the one-dimensional spectra. The grey scale has been chosen to bring out low signal-to-noise lines and can lead to visual artefacts such as the strange change in continuum strength of AMS08. For the two objects observed in April 2005 (AMS04 and AMS13), the pixel scale in the dispersion axis was not the same for the blue and red arms, and so the two-dimensional spectra are not combined, just overlayed on each other. Particularly strong residual sky lines have been labelled in the one-dimensional spectra and are clearly visible in the two-dimesional ones. In AMS04, the sky lines are close to the N II] and C II] lines, making these two lines hard to detect in the grey scale image. The reader is assured that these two lines are detected and are not due to the residual sky lines.

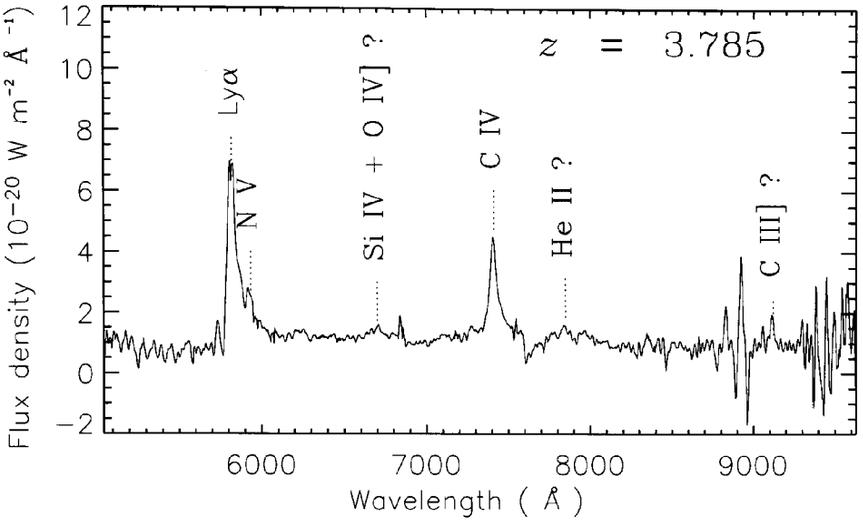

Figure 3.3: The spectrum of the type-1 quasar observed at the same time as AMS16.

is probably a pure starburst: see Chapter 5). Only one object showed (very faint) continuum and no lines: AMS20. As mentioned in Section 3.1, it will require more study to determine whether this object is similar to AMS18, is at $1.3 \lesssim z \lesssim 1.7$, or is a higher-redshift object. If this object were a contaminant, like a $z \sim 0.5$ ULIRG, it would have shown stronger continuum and the [O II] 3727 Å line. It is important to emphasize on how faint our sources are: all objects, even those with emission lines in the R-band or showing some continuum, have $m_R \geq 22.5$ (Vega), and most have $m_R \geq 23$. The rest of the objects show blank spectra, confirming that there are no low-redshift contaminants in our sample. A $2.6L^*$ elliptical at $z = 1.4$ would have a continuum flux density of 1×10^{-21} W m^{-2} Å^{-1}, at the limit of our sensitivity. AMS20, with faint red continuum, is therefore consistent with having an elliptical host galaxy, and being somewhere in the spectroscopic desert.

For all 9 objects at $z_{spec} \geq 1.7$, the redshift implies mid-infrared luminosities consistent with quasars and radio luminosities consistent with radio-intermediate AGN. This, however, is assuming the warm dust detected at mid-infrared wavelengths is characteristic of accreting objects (the dust in the torus of the unified schemes). The most recent studies of radio-loud AGN have shown strong support for this interpretation (Ogle et al., 2006; Shi et al., 2006), but independent proof that our objects are accreting can only come from high-ionisation lines. Six objects have detectable C IV,

so strictly speaking, only these 6 are independently confirmed to be type-2 quasars.

The nature of the blank-spectrum objects is discussed further in Chapter 4, but we see that their blank optical spectra are consistent with host ellipticals at $z \gtrsim 1.4$. If 24-μm flux density is a good tracer of narrow emission line strength, then we expect all our sources to have detectable Ly α lines if they lie at $z \geq 1.7$. In addition, the C IV (1549Å) line is detected in six out of the nine objects with Ly α, and in the composite spectrum (see Section 3.4) it has 36% of the flux of Ly α. Hence, some objects in the spectroscopic desert should also have detectable C IV lines. The two blank objects brightest at 24-μm have redshifts from Spitzer-IRS in the same range as the rest of the optical spectra, where we should have seen Ly α. This suggests that at least some of the blank objects are at redshifts high enough to have narrow emission lines in the optical band, and that their spectra are blank for another reason. This reason could be that they have weaker emission lines, but they would have to be significantly weaker than those of the narrow-line objects, despite having similar 24-μm fluxes. Another alternative, is that the narrow emission line region is itself obscured. This seems a very likely scenario for AMS06 and AMS19, which are both at redshifts ($z = 1.76$ and $z = 2.25$ respectively) where Ly-α should be visible in our optical spectroscopy.

3.3 Crude Photometric Redshifts

As discussed in Section 2.2, for $A_V \gtrsim 10$ the 3.6-μm flux density should be dominated by light from the host galaxy's old stellar population. We estimated crude "photometric" redshifts for the entire sample by assuming the host galaxies to be the progenitors of present day massive elliptical galaxies (see Table 3.1). These galaxies were taken from the models of Bruzual & Charlot (2003), formed at $z = 10$ in a single starburst, with a Salpeter IMF (Salpeter, 1955) and a stellar mass of $3.8 \times 10^{11} M_{\odot}$. Such host galaxies would become 2.6 L^* galaxies in the local K-band luminosity function (Cole et al., 2001). The justification for such an assumption is that radio-loud galaxies show a $K - z$ Hubble diagram consistent with such massive host galaxies ($\sim 3L^*$ Jarvis et al., 2001a; Willott et al., 2003a) and evidence points to the host galaxies of $z \sim 2$ radio-quiet quasars being $\sim 2L^*$ ellipticals (Kukula et al., 2001).

The scatter in true host luminosity means that individually, the photometric redshifts are not necessarily close to the spectroscopic redshift. However, for 10 out of 12 objects, the photometric

Name	z	Line	λ_{rest} /Å	λ_{obs} /Å	FWHM /km s^{-1}	Flux /W m^{-2}	$\log_{10} L_{\rm line}$ /W	Error in flux /%
AMS03	2.698 ± 0.009	Ly α	1216	4481	1400	1.22×10^{-19}	35.86	20
		Ly α	1216	4512	550	3.69×10^{-20}	35.34	18
AMS04	1.782 ± 0.001	Ly α	1216	3382	1800	5.01×10^{-19}	36.04	12
		C III]	1909	5311	1450	1.02×10^{-19}	35.35	21
		N II]	2142	5963	2550	1.16×10^{-19}	35.40	20
		C II]	2326	6467	1250	8.59×10^{-20}	35.27	28
AMS05	2.017 ± 0.006	Ly α	1216	3658	1250	1.32×10^{-19}	35.59	38
		C IV	1549	4681	1000	1.16×10^{-19}	35.53	18
		He II	1640	4952	500	3.16×10^{-20}	34.97	41
AMS08	1.979 ± 0.004	Ly α	1216	3622	1900	5.05×10^{-19}	36.15	15
		C IV	1549	4622	1400	4.49×10^{-20}	35.10	23
		He II	1640	4877	900	2.30×10^{-20}	34.81	35
AMS12	2.767 ± 0.005	Ly α	1216	4586	650	4.41×10^{-19}	36.45	17
		C IV	1549	5824	1150	3.50×10^{-20}	35.35	25
		He II	1640	6181	1100	2.22×10^{-20}	35.15	26
AMS13	1.974 ± 0.003	Ly α	1216	3613	1650	9.88×10^{-19}	36.44	12
		C IV	1549	4611	1300	1.67×10^{-19}	35.67	20
AMS14	1.794 ± 0.001	Ly α	1216	3398	1500	3.69×10^{-19}	35.91	18
		C IV	1549	4326	600	5.61×10^{-20}	34.92	21
AMS16	4.169 ± 0.002	Ly α	1216	6288	1050	3.19×10^{-19}	36.73	12
		N V	1240	6406	2050	1.56×10^{-19}	36.42	28
		C IV	1549	8009	2050	2.69×10^{-19}	36.66	16
AMS17	3.137 ± 0.002	Ly α	1216	5031	1200	2.89×10^{-19}	36.40	16
AMS18	1.017 ± 0.004	C II]	2326	4680	1400	8.19×10^{-20}	34.65	25
		Mg II	2798	5652	3500	1.14×10^{-19}	34.79	44
		[O II]	3727	7527	2200	1.12×10^{-19}	34.79	27

Table 3.3: Table of emission line properties of the 10 objects with spectroscopic redshifts from our optical spectroscopy. The lines were fitted with gaussians to find λ_{obs}, FWHM, and the flux. For objects with several lines, the error quoted is the square root of the average variance. For objects with only one line, the error is assumed to be dominated by the fitting of a gaussian to the line. This in turn is dominated by the spectral resolution and the seeing. In two cases (AMS14 and AMS18) an error in wavelength calibration led to incorrect identification of lines and redshifts in Martínez-Sansigre et al. (2005). The error in flux (and luminosity) is the sum in quadrature of the photometric error (typically 10%), the error from the slit (typically 5%) and the uncertainty in the continuum. The FWHM is deconvolved by subtracting in quadrature the seeing from the observed size of the emission line. For lines with errors > 20% the measurements of the FWHM are not reliable, and the possible presence of broad lines (e.g. Mg II in AMS18) is therefore not significant.

redshifts are overall in reasonable agreement with the spectroscopic redshifts. There are two cases (AMS14 and AMS18) in which the photometric redshift is clearly overestimated. There are two possible explanations for this: a host galaxy which is smaller than the progenitors of $\sim 2-3L^*$ ellipticals, and so our mass is an overestimate, or a star-forming host-galaxy, in which case our elliptical galaxy template is not appropriate. For the objects that have spectroscopy, the mean and median values of $z_{\rm phot}$ are 2.75 and 2.65 respectively while the mean and median spectroscopic redshifts are 2.33 and 2.00 (2.29 and 2.00 if the Spitzer-IRS are included): this represents reasonable agreement for such a simple photometric redshift estimation and gives us some confidence that we can estimate how many objects that remained unobserved or had blank optical spectra are at $z \geq 2$ (for the modelling in Chapter 4). To bring the median $z_{\rm phot}$ to the value of the median $z_{\rm spec}$ one would have to change the mass of the elliptical to $2.9 \times 10^{11} M_{\odot}$, which would correspond to the progenitor of a $\sim 2L^*$ elliptical galaxy instead of $\sim 2.6L^*$. This would also bring the mean $z_{\rm phot}$ close to the mean $z_{\rm spec}$. The fact that, for the objects with emission lines, the "photometric" redshifts are roughly in agreement with the spectroscopic ones, suggests the host galaxies are the progenitors of massive ellipticals ($\gtrsim 2L^*$).

A possible source of error for our photometric redshifts would be the contribution of quasar light to $S_{3.6\mu{\rm m}}$, together with a large host galaxy. This could plausibly make us miss some $z \sim 2$ type-2 quasars, which would only make the results of Chapter 4 and Martínez-Sansigre et al. (2005) more striking. Another source of error is if the host galaxy is not a simple progenitor of an elliptical, but an active starburst. The old stellar population would then be less luminous, and $z_{\rm phot}$ would be overestimated. The lack of lower-redshift contaminants in our spectra gives us confidence that this is not a serious problem.

3.4 Composite Type-2 Spectrum

Following Rawlings et al. (2001), we proceeded to create a composite type-2 quasar spectrum by shifting the individual spectra to the rest-frame with the IRAF task NEWREDSHIFT. The individual spectra were all scaled by their Ly α line flux and then averaged bin-by-bin with a sigma-clipping rejection algorithm with the clip set to $\pm 1.5\sigma$. The object at $z = 1.02$ was therefore not included as there was no way of scaling it consistently. The composite of 9 objects is shown in Figure 3.5

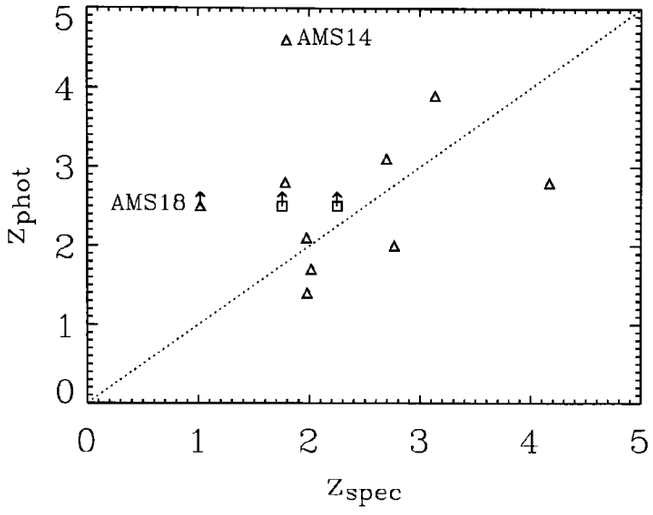

Figure 3.4: Comparison between crude photometric and spectroscopic redshift for the objects with redshifts. Triangles are objects with narrow-lines in our spectroscopy, squares are objects with redshifts from Spitzer-IRS only. We see a large scatter, and individually the photometric redshifts are of no use. On the whole, the agreement is reasonable except for two objects (AMS14 and AMS18). This means that the objects with spectroscopic redshifts in our sample are consistent with having massive elliptical galaxies as hosts.

and shows strong C IV (1549 Å) and He II (1640 Å) as well as Ly α (1216 Å) lines. C II] (2326 Å) and Mg II (2798 Å) are also detected.

Table 3.4 shows the line fluxes relative to Ly α. We can see C IV , He II and C II] are clearly detected, with relative values of 0.36, 0.09 and 0.09. For the 6 objects with detected C IV, the relative value compared to Ly α ranges between 0.08 and 0.84. In addition we see that the Mg II line is present, with a relative line flux of 0.05, while the N V (1240 Å) and C III] (1909 Å) are not detected. The Mg II line must be detected at low SNR in several individual spectra to make it detected in the composite. C III] is only detected in one of the objects making the composite and this could be due to the fact that at $z \gtrsim 2$ it is shifted to $\lambda \geq 5700$ Å, where it falls near the dichroic cross-over region used in the July 2004 observations. AMS04 has C III] and is at $z = 1.78$, but it was observed using a 5300 Å dichroic. The N V line is only present in AMS16. This composite spectrum is similar to that found for high-redshift radio galaxies (e.g McCarthy, 1993, and more recently Rawlings et al., 2001; Jarvis et al., 2001b), except that the relative strength of C IV is a factor of ~ 3 higher here than in McCarthy (1993). The C II] line is stronger by a factor of 3 compared to McCarthy (1993) and the Jarvis et al. (2001b) value for radio galaxies with a

projected linear size, D, > 70 kpc, but consistent with the Jarvis et al. (2001b) value for radio galaxies with D < 70 kpc.

Comparing these ratios with McCarthy (1993); Rawlings et al. (2001); Jarvis et al. (2001b) we find that they are broadly similar to those of powerful radio galaxies except C IV is significantly stronger, even stronger than for the McCarthy (1993) Seyfert-2 galaxies. The C II] is similar to the Jarvis et al. (2001b) value for radio galaxies with D < 70 kpc. This might be an indication of a more complicated line-emission mechanism than simple photoionisation from a central engine, some of the ionisation might be happening as a result of jet activity (see for example Best et al., 2000; Jarvis et al., 2001b).

Also, comparing our composite type-2 to four individual high-redshift type-2s from the literature, we find that the Stern et al. (2002) type-2 ($z = 3.288$) has Ly α, C IV and He II ratios (100:19:9) similar to our composite. The Mainieri et al. (2005) object ($z = 3.660$) has a Ly-α-to-C IV ratio (100:14) slightly lower than of our composite and the Jarvis et al. (2005) type-2 ($z = 1.65$) has a C IV to He II ratio (1:1) slightly lower than our composite. The Norman et al. (2002) type-2 at $z = 3.700$ has substantially weaker Ly α relative to C IV and He II (100:60:17); it is more similar to AMS16, for example, than to the composite. We therefore find, on average, good agreement between the individual high-redshift type-2s from the literature and our composite.

As a word of warning, we note that the composite includes both objects with C IV and without C IV detections. It not impossible that the objects where C IV is not detected lack this high-ionisation line altogether, and the C IV to Ly α ratio in the composite might be artificially very high due to AMS05 and AMS16 having very strong C IV lines. In Figure 3.6 we plot the $\log_{10}$ of the ratio of C IV to Ly α, against $\log_{10}$ Ly α luminosity, and find there is no obvious trend. For the 6 objects with detected C IV, the C IV to Ly α ratios vary from 0.88 to 0.02, indicating a range in ionisation states. The higher ratios are consistent with that expected for "classic" type-2 quasars, while the lower ratios are more similar to, for example, the McCarthy (1993) radio galaxies or even QSOs. It seems that our sample contains a fraction of objects where the observed ionisation state is lower than expected for type-2 quasars.

We consider this alongside our finding that several of the Ly α lines are extended over ~1-5 arcsec (see Section 3.1), corresponding to physical sizes of 8-40 kpc. There is a strong hint that a significant part of the Ly α emission originates in low-ionisation, extended regions, and therefore

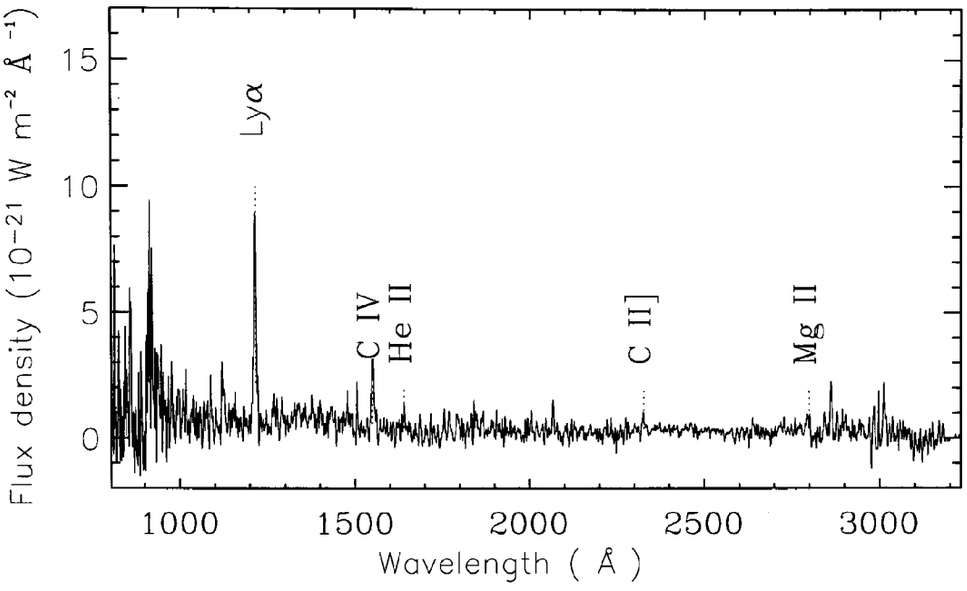

Figure 3.5: Composite type-2 quasar spectrum. This has been made as described in Section 3.4, and it shows Ly α, particularly strong C IV, He II, C II] and Mg II. C III] is present in one individual object, and might be present in more but at $z \sim 2$ it falls around the dichroic cross-over region, so the noise might be too high to detect it. All the lines detected in the composite and in individual objects are present in the observations of IRAS FSC 10214+4724 (Rowan-Robinson et al., 1993; Serjeant et al., 1998).

the total Ly α luminosity correlates poorly with the C IV line strength (which originates from the narrow-emission line region). This could explain the variance in some of the C IV to Ly α line ratios.

The radio properties of our objects also show significant variance (see Chapter 5). It is possible that by selecting radio-intermediate objects, we have found a sample which includes objects with ionisation properties similar to those of radio-galaxies (e.g. AMS04 and AMS13) and others more similar to radio-quiet type-2 quasars (e.g. AMS05 and AMS16). In this case, the ionisation states of the sources should be considered separately, and the composite spectrum might not be representative of individual sources. However, the poor signal-to-noise ratio of our spectra does not allow such study on an individual basis.

Somewhat surprisingly another characteristic in common with radio galaxies is that all objects which show Ly α have at least some extended emission (in particular AMS03, AMS04, AMS08, AMS13 and AMS16 have very extended Ly α emission). AMS12 seems to have two Ly α

Line	This Sample	McCarthy (1993) RG	SyII	QSO
Ly α	100	100	100	100
C IV	36	12	22	8
He II	9	10	4	5
C II]	9	3	-	4
Mg II	5	3	4	23

Table 3.4: Comparison between the line ratios of this sample and those found by McCarthy (1993) for radio galaxies (RG) Seyfert-2s (SyII) and QSOs. The line fluxes are quoted as a percentage of the Ly α flux. The He II, C II] and Mg II are roughly consistent with the radio galaxy values, but the C IV is significantly brighter, even brighter than found in Seyfert-2s.

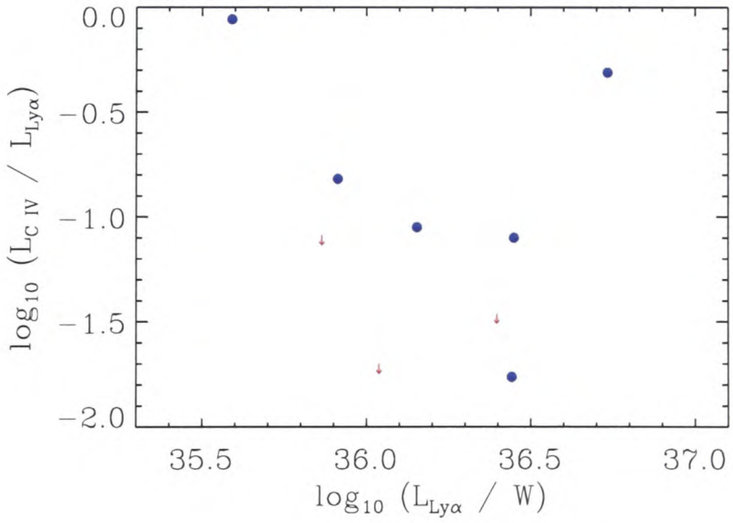

Figure 3.6: $\mathrm{Log_{10}(L_{C\ IV}/\ L_{Ly\ \alpha})}$ vs $\mathrm{Log_{10}(L_{Ly\ \alpha}/\ W)}$. Objects with a detection of C IV are in blue, while those with only a limit on the line strength are marked as red arrows. The values are from Table 3.3, and where C IV is undetected it has been assigned an upper flux limit of 1×10^{-20} W m^{-2} and converted to a luminosity using the spectroscopic redshift. There is no obvious correlation. As discussed in the text, together with the spatial extent of the Ly α line of certain objects, suggests at least part of the Ly α flux originates in different physical regions to the C IV line.

components: a bright, spatially-unresolved "peak" sitting on top of a spatially-extended fainter "plateau". Also, AMS13 and AMS16 have other lines which are spatially extended (C IV and N V respectively). In AMS04, the Ly α is $\sim$ 5.5 arcseconds in size (once deconvolved from the seeing), which is larger than the VLA beam size. For the other cases, we cannot currently tell whether the emission lines extended over regions larger than the radio emission. These characteristics all remind us of classic radio loud sources despite their relatively low radio flux densities, so in Section 3.5 we proceed to compare our type-2 quasars with radio loud objects.

3.5 Comparison to Radio-Loud Objects

The mean radio flux density of the sample at 1.4 GHz is 780 μJy, which at the mean spectroscopic redshift $z = 2.33$ corresponds to a radio luminosity of $L_{1.4\ \mathrm{GHz}} = 2 \times 10^{24}$ W Hz^{-1} sr^{-1} (assuming a spectral index $\alpha = 0.8$, where $L \propto \nu^{-\alpha}$). This is well below the break in the RLF (Willott et al., 1998) and in the regime where typical radio-selected objects have Fanaroff-Riley Class I (FRI) radio structures (Fanaroff & Riley, 1974). There is also little direct evidence of associated optical quasar activity (Grimes et al., 2004) and weak or absent emission lines suggesting that, whether or not obscuring tori exist in this class of objects (Chiaberge et al., 1999), any associated quasar is accreting at a very low rate (Rawlings & Saunders, 1991). However, considering that FRIs have occasionally been found to accrete at high rates (Blundell & Rawlings, 2001), we proceed to investigate the possibility of our objects having similar properties to radio-loud objects.

One typical characteristic of radio-loud objects is the presence of extended jets on scales larger than the host galaxy. Figure 3.1 shows that most of the type-2 quasars shown in this paper are point-like in the VLA observations ($\sim$ 5-arcsec resolution). In the few cases where the radio flux is extended, it generally coincides with another galaxy in the R band or 3.6 μm images. However, if there is diffuse flux on large scales, the relatively long baselines of the VLA B-array could miss it, so we would not see large jets.

The Westerbork Synthesis Radio Telescope (WSRT) has also observed at 1.4 GHz the central region of the FLS, with an angular resolution of $\sim$ 14 arcsec (Morganti et al., 2004). The shortest baselines of the WSRT are smaller than those of the VLA in B-array and this enables it to pick up flux on more extended scales, so any extended sources should have a significantly higher flux

Nname	$S_{\rm VLA\ 1.4GHz}$ /μJy	$\sigma_{\rm VLA}$ /μJy	$S_{\rm WSRT\ 1.4GHz}$ /μJy	$\sigma_{\rm WSRT}$ /μJy
AMS01	490	31	499	19
AMS02	1184	55	1209	17
AMS03	1986	87	2370	16
AMS04	536	72	887	13
AMS05	1038	49	1017	12
AMS06	444	31	380	14
AMS07	354	27	289	10
AMS08	655	36	679	12
AMS10	1645	73	1911	11
AMS11	356	29	253	9
AMS13	1888	83	2076	14
AMS18	390	29	351	23
AMS19	822	41	783	15

Table 3.5: Comparison between the radio flux densities of the VLA in B array (beam size $\sim$ 5 arcsec) and the WSRT fluxes (beam size $\sim$ 14 arcsec). We can see that the two flux densities agree within 3-σ in all but two cases. Only AMS03 and AMS04 are not consistent, but examination of the VLA B-array images shows this is due to confusion. In the case of AMS03 it is clearly due to another radio source, while in the case of AMSO4, it is not yet clear whether the confused flux density is from another source or from a diffuse radio component.

density in the WSRT catalogue than the VLA one. Thirteen of our targets are within the area observed by the WSRT: the flux densities are shown in Table 3.5. The rest of our sample was outside the area covered by the survey of Morganti et al. (2004). Most of the objects in Table 3.5 have consistent fluxes and therefore are unlikely to have a significant fraction of their radio flux in extended jets. AMS04, however has a flux density as measured by WSRT which is 65% higher than that measured by the VLA, suggesting the presence of jets. The 3.6 μm-radio overlay (Figure 3.1) shows there is another radio source within the WSRT beam, and there is a hint of a faint galaxy which does not match the radio position perfectly. The companion radio source has a flux density of 331 μJy, so the WSRT flux density is clearly the sum of these two individual sources. If this is indeed due to another galaxy, then the WSRT is confusing both sources. However, we cannot be certain that the adjacent radio source is independent and due to another galaxy, so there is a chance that AMS04 has an extended jet with a flux density comparable to that of the central source.

The type-2s with the highest flux densities (AMS03, AMS10 and AMS13) all have more flux as observed by WSRT. Once again, however, there is a radio source with a clear optical (and infrared) ID next to one of the objects (AMS03), with a flux density of 203 μJy, so the WSRT flux

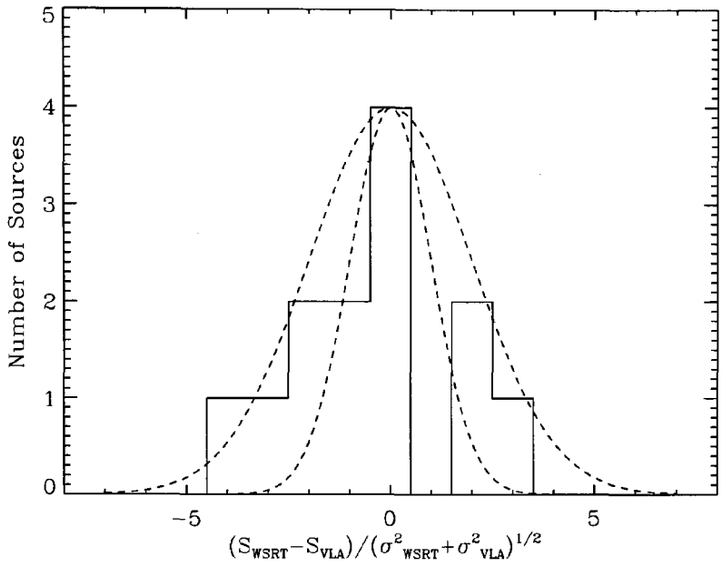

Figure 3.7: Normalised flux density difference distribution. This is computed as described in the text, and should match the gaussian distribution with $\sigma = 1$ (inner gaussian). This is clearly not the case, but it matches reasonably well somewhere between the $\sigma = 1$ and $\sigma = 2$ gaussians.

is consistent with the sum of the two confused sources, within their errors. The flux of AMS13 is consistent in both telescopes to within 2σ and AMS10 is consistent within 3σ. Although 3σ might appear poor agreement, the reader is reminded of the highly spatially correlated nature (and therefore non-poissonian) of the noise in interferometer images, meaning the usual interpretation that only 0.5% of measurements should differ by 3σ is not appropriate here. The central frequencies of both observations are not exactly the same: however, this small difference in frequency can only account for$\sim$ 2% of the flux difference.

To analyse the differences in flux density between both interferometers, we computed the normalised flux density difference: the measured flux density difference divided by the sum in quadrature of the 1σ errors of Table 3.5, $(S_{\rm WSRT} - S_{\rm VLA})/\sigma$ where $\sigma = (\sigma^2_{\rm WSRT} + \sigma^2_{\rm VLA})^{1/2}$, and plotted it in Figure 3.7. For AMS03 and AMS04, we remove from the WSRT flux density the VLA flux density of the adjacent radio sources. Overplotted on the distribution are two gaussian distributions, one with $\sigma = 1$, another with $\sigma = 2$. If there is no systematic difference between the two measurements, the plot should look like the gaussian distribution with $\sigma = 1$, centred around 0. We see that this is clearly not the case, so the flux densities from both surveys are not consistent with random noise of variance $\sigma^2 = \sigma^2_{\rm WSRT} + \sigma^2_{\rm VLA}$. However, the distribution roughly

agrees somewhere between the $\sigma = 1$ and $\sigma = 2$ gaussians (with $\sigma^2 = 2-4\times(\sigma^2_{\rm WSRT}+\sigma^2_{\rm VLA})$). This suggests that the measurements from the WSRT and VLA are consistent provided the errors are taken to be larger (but still less than twice) the RMS value of the noise. We therefore conclude that there is no firm evidence of extended radio emission around any of the 13 objects observed by both interferometers (other than possibly AMS04). The angular resolution of the VLA observations (5 arcsec) gives us an upper limit on the size of any jets. At $z = 2$ this corresponds to a jet size $\lesssim 40$ kpc.

Another known characteristic of radio-loud galaxies is the presence of extended line emission on similar scales to those of the radio jets. We have not only found that the composite spectrum resembles that of radio galaxies, but several of our objects show significantly extended Ly α (AMS03, AMS04, AMS08, AMS13 and AMS16) and some have other extended lines (AMS13 and AMS16). In some objects (e.g. AMS16) the slit was placed along the direction of the slightly elongated radio axes, meaning that the emission lines could be extended along a hypothetical jet. In most cases, however, the slit PA was chosen for other reasons, so that any alignment with hypothetical jets would be coincidence.

The line ratios and the spatial extent of high-excitation lines of our objects seem to have some similarities to radio galaxies, as we have discussed in Section 3.4. The [O III] line is an excellent indicator of the strength of the underlying quasar continuum (Simpson, 1998a), so we now use the McCarthy (1993) radio galaxy line ratios to convert our line luminosities to [O III] (5007 Å) luminosities, to compare our results to the radio-loud samples discussed by Grimes et al. (2004). We converted the Ly α line to [O III], and when C IV is present we also converted that line. This yields two different estimates for the [O III] luminosity which are likely to be quite different, giving us a handle on the possible systematic errors in converting to [O III] luminosity, given that our composite spectrum has some differences with the McCarthy (1993) radio galaxy composite. The McCarthy (1993) ratios are $([\text{O III}]/\text{C IV})_{\rm RG} = 2.38$ and $([\text{O III}]/\text{Ly }\alpha)_{\rm RG} = 0.28$. We also convert radio flux at 1.4 GHz to luminosity at 151 MHz, assuming a spectral index $\alpha^{1.4}_{151} = 0.8$ (where flux density $\propto \nu^{-\alpha}$). The values obtained are shown in Table 3.6

Figure 3.8 shows how our objects sit on the $L_{151} - L_{[\rm OIII]}$ plane. The solid line shows the best fit line for the radio-loud galaxies from the 3CRR,6CE and 7CRS samples (Figure 4 of Grimes et al., 2004). The region between the dashed lines encompasses all of the radio loud objects, so

Name	Line used	$\log_{10} L_{[\mathrm{OIII}]}$ /W	$\log_{10} L_{151}$ /W Hz^{-1} sr^{-1}
AMS03	Ly α	35.3	25.6
AMS03	Ly α	34.8	25.6
AMS04	Ly α	35.5	24.7
AMS05	Ly α	35.0	25.1
AMS05	C IV	35.9	25.1
AMS08	Ly α	35.6	24.8
AMS08	C IV	35.5	24.8
AMS12	Ly α	35.9	25.3
AMS12	C IV	35.7	25.3
AMS13	Ly α	35.9	25.3
AMS13	C IV	36.0	25.3
AMS14	Ly α	35.4	24.4
AMS14	C IV	35.3	24.4
AMS16	Ly α	36.2	25.4
AMS16	C IV	37.0	25.4
AMS17	Ly α	35.8	25.3

Table 3.6: Data used to plot Figure 3.8. The second column states which lines were used to estimate the [O III] line strength. The 151 MHz luminosities were estimated from the 1.4 GHz flux densities, assuming a spectral index $\alpha_{151}^{1.4} = 0.8$ between 151 MHz and 1.4 GHz.

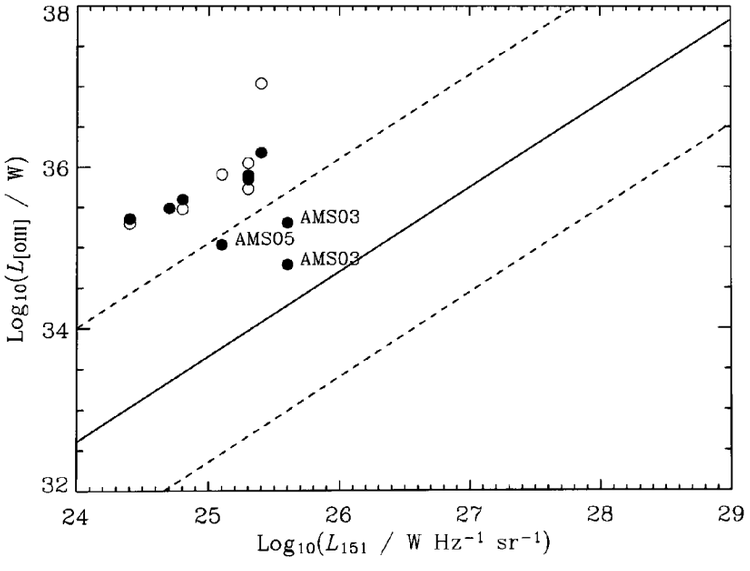

Figure 3.8: Comparison to Figure 4 of Grimes et al. (2004). The symbols represent which line has been used to convert to [O III]: filled circles for Ly α, empty circles for C IV. The solid line represents the best fit to the radio-loud samples (3CRR, 6CE, 7CRS) in Grimes et al. (2004), with the dashed lines representing the loci which encompass all the radio-loud sources (so similar to $\pm 3\sigma$ contours).

all our objects except AMS03 lie in a different region to them. However, some important details must be remembered. First, we have assumed all our sources to be steep spectrum ($\alpha_{151}^{1400} = 0.8$), something for which we have no current evidence. The true value of $\alpha_{151}^{1.4}$ is unlikely to be much larger (i.e. steeper) but objects with flatter true spectra will actually have lower L_{151} than shown here (see Chapter 5). In addition, the $L_{[OIII]}$ for all of the objects has been estimated using the radio-galaxy ratios from McCarthy (1993) which have Ly α relative to C IV or He II systematically brighter than in our sample. The objects for which we have estimated $L_{[OIII]}$ from Ly α (such as AMS03) are likely to have true $L_{[OIII]}$ values brighter than those shown here. Finally, the dashed lines in Figure 3.8 are not $\pm 1\sigma$ loci, they are the lines that encompass the entire radio-loud population (i.e. they could be considered $\sim 3\sigma$ contours). Once these effects are taken into consideration, one sees that all the possible systematic errors would only lead to brighter [O III] lines and fainter radio luminosity at 151 MHz. Only two objects are anywhere near the radio-loud samples: AMS03 and AMS05. The first object has two different Ly α lines, and although we have used both for comparative reasons, the weaker of the two lines (the narrower line of the two) is unlikely to originate from an AGN, the stronger line should be looked at. The Ly α line of AMS05 has a large uncertainty in its flux measurement and is likely to be missing some flux since it was observed at a high airmass.

The sample presented here has typical [O III] luminosity (in $\log_{10}$) of 35-36. This is comparable to the radio-loud quasars in Figure 4 of Grimes et al. (2004), however, for a similar value of $L_{[OIII]}$, the sample presented here has a L_{151} fainter by a factor of 100. It therefore differs from typical radio-selected objects in several respects: once the obscuration of the quasar nucleus is accounted for, they have the high accretion rates of typical quasars, but relatively low radio luminosities. The radio luminosities of these objects show that these are the radio-bright end of the radio-quiet population, or so called 'radio-intermediate' quasars.

3.6 Summary

We have found a set of selection criteria that yields a population of radio-quiet, more strictly radio-intermediate, type-2 quasars at $z \sim 2$. About half of the objects in this sample show emission lines in their optical spectra. The ratios of these emission lines are similar to those of radio galaxies with

the main difference that the C IV line of type-2 quasars is on average stronger and consistent with individual high-redshift type-2 quasars from the literature. The Ly α is often spatially-extended, as are sometimes the high ionisation lines. This suggests that some of the line emission originates outside the classic narrow-line region, but the exact nature of this emission cannot be deduced here. The spectroscopic redshifts, combined with the mid-infrared fluxes, suggest we have indeed found type-2 quasars, but this is slightly model-dependent: it assumes the mid-infrared emission is an indicator of underlying accretion. Independent confirmation, in the form of high-ionisation lines (e.g. C IV) is only present in 6 objects. In the other 3, until higher SNR spectra can be obtained, no strong independent conclusion can be made about obscured accretion. However, the results of recent mid-infrared studies of radio-loud AGN (Ogle et al., 2006; Shi et al., 2006) are still consistent with the unified scheme.

To further compare the type-2s to radio galaxies and radio-loud quasars, we compare their location on the $L_{151} - L_{[\mathrm{OIII}]}$ plane, and find significant differences. The type-2s have $L_{[\mathrm{OIII}]}$ comparable to radio-loud type-1 quasars, while being fainter at radio wavelengths by a factor of ~ 100. In addition, the type-2s presented here show no signs of large extended jets (except possibly AMS04). Finally, comparison between our rough photometric redshift estimation, which assumes $2.6L^*$ host galaxies and our spectroscopic redshifts suggests that the objects in our sample which yield optical spectra are consistent with having host galaxies which are massive ellipticals. In particular changing our model elliptical from $2.6L^*$ to $2L^*$ would bring agreement to the median z_{phot} and z_{spec}, and close to agreement for the mean z_{phot} and z_{spec}.

Chapter 4

Most supermassive black hole growth is obscured by dust

In the previous Chapter, we have found a population of classic (radio-intermediate) type-2 quasars, showing only narrow-lines with, presumably, the torus blocking direct view of the quasar along our line-of-sight. We refer to these objects as 'torus-obscured' type-2s. The lack of objects with spectroscopic redshifts around $z \sim 1.5$ could plausibly be due to the Ly α line being below the atmospheric cut-off, but C IV is detected in most of the higher-z objects (and He II and C II] are sometimes detectable) so the lack of objects at this redshift may instead be associated with the silicate absorption feature falling on the 24-μm band, as discussed in Section 2.1 of Chapter 2.

Of the remaining 11 objects, 10 show completely blank spectra and only one shows faint red continuum (AMS20). Their faint 3.6 μm flux densities and large R-band magnitudes suggest these are high redshift objects just like the 'torus-obscured' objects. In our 30-minute integrations, type-1 quasars would have shown bright continuum and lower-redshift ($z \lesssim 1$) starbursts would have shown [O II] line emission or at least some strong continuum, like AMS18, our only likely contaminant. Thus our sample does not suffer heavily from contamination: these blank objects are probably also high-redshift type-2 quasars.

Some of these 11 objects could be at $1.4 \leq z \leq 1.7$ with the C IV or He II lines too faint to be detected, although we have seen that 24-μm selection might disfavour this particular range of redshifts. It is not impossible that some objects have Ly α too faint to be detected, but we cannot

test this hypothesis without spectroscopy using a telescope that is significantly more sensitive (e.g. an 8-m class telescope).

The remaining objects are presumably obscured by dust on a large scale ($\sim$10 pc to 1 kpc), which hides the narrow-line region as well as the broad-line region. Such concentration of dust is characteristic of star-forming regions, so we are presumably seeing either a nuclear or a galaxy-scale starburst. From their blank optical spectra we know that these objects are indeed at high redshift and therefore their mid-infrared flux density is characteristic of objects accreting at a high rate, while in most cases the radio flux density is too high to originate only in star-forming regions and must be due to an AGN (see Chapter 5). In two cases (AMS06 and AMS19), published mid-infrared spectra confirm these objects to lie in the correct redshift range. In the other nine cases, despite the lack of lines to pinpoint their exact redshift, we are confident that these blank objects are type-2 quasars at high redshift.

The obscuration, however, is not entirely due to an orientation effect, like for 'torus-obscured' objects, since then we would expect to have a clear line-of-sight to the narrow-line region. A plausible explanation is dust in the host galaxy, and so we refer to these objects as 'host-obscured' type-2s. At this stage, we cannot differentiate between dust at scales of $\sim$10 pc or $\sim$1 kpc. Such objects, lacking AGN emission lines in the optical spectra, have been found at lower redshift in the samples of Lacy et al. (2004, 2005a) and Leipski et al. (2005), and the properties we infer for our 'host-obscured' type-2 quasars are indeed those predicted for supermassive black holes growing in the centres of proto-galaxies (Fabian, 1999).

Some of the blank objects are probably torus obscured at $1.4 \leq z \leq 1.7$. Therefore, strictly speaking only the objects at redshifts where Ly α is detectable should be considered as possible host-obscured objects. Since our photometric redshifts are crude at best, we cannot differentiate in individual objects. However, further down we use the crude redshifts to estimate how many of our blank objects, are expected to be at $z \geq 2$ and are therefore likely host-obscured since Ly α would be, in principle, detectable if it were not obscured.

It is therefore not surprising that the Ly α (whether from the narrow-line or star-forming regions) in the host-obscured type-2s is too obscured for our exposure times (30 minutes) with a 4-m telescope. Note that Ly α is particularly susceptible to destruction by resonant scattering if Ly α emitting regions are dusty. For example, successful spectroscopy of sub-mm galaxies

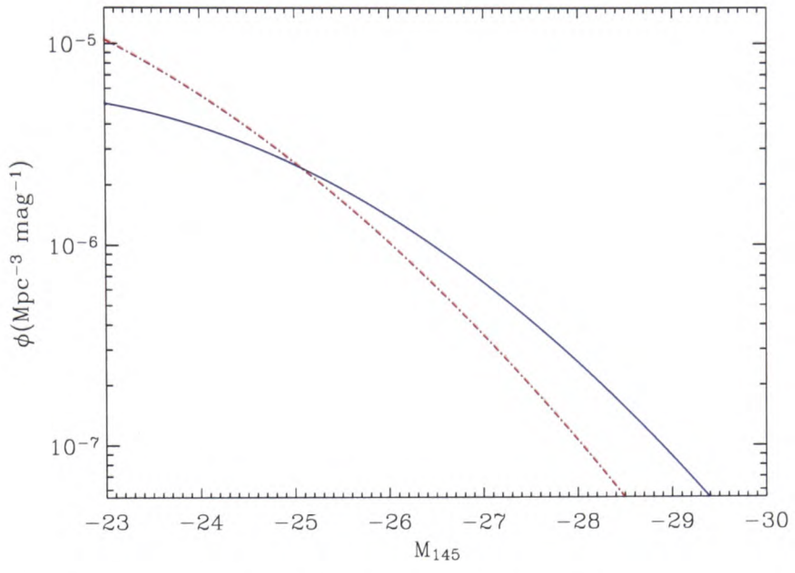

Figure 4.1: Type-1 luminosity function from Wolf et al. (2003) (solid blue line) used to estimate the number of type-1 quasars adhering to our selection criteria. The red dashed-dotted line is the type-2 luminosity function resultant from applying the receding-torus model of Simpson (2005) to the type-1 luminosity function. This type-2 luminosity function enables us to predict the expected quasar fraction from the receding torus (RT2) in Figure 4.2.

in the blue requires very long integrations (1.5-6 hours) with 8-m or 10-m class telescopes (e.g. Chapman et al., 2005). We do note that AMS03 shows spatially-extended Ly α, no other lines and no continuum, so there is a chance this object is host-obscured and the second Ly α line traces the starburst: this requires further study.

4.1 The quasar fraction

To interpret our results in terms of the 'quasar fraction' q – the ratio of the number of type-1 quasars to the total number of type-1 and type-2 quasars – we need to predict $\langle N_1 \rangle$: the average number of type-1 quasars meeting identical $S_{24\mu m}$ and $S_{1.4GHz}$ selection criteria to our sample of type-2 quasars, and having matched redshift and sky area selection functions. To account for the various uncertainties, we estimate a probability distribution $p(\langle N_1 \rangle)$.

The most important uncertainty, and the dominant contributor to the width of $p(\langle N_1 \rangle)$, results

from the lower $S_{1.4\mathrm{GHz}}$ cut. This cut greatly reduces the number of quasars by excluding the low-luminosity end of the radio-quiet population (Cirasuolo et al., 2003) but is at a point where radio-quiet quasars contribute significantly to the source counts (Jarvis & Rawlings, 2004, Simpson et al., 2006, Appendix A). We used the B-band luminosity function of Wolf et al. (2003), adopted a radio luminosity versus optical luminosity correlation, including a measured scatter, for type-1 quasars (Cirasuolo et al., 2003) and generated a probability distribution for the fraction of type-1 quasars with $S_{24\mu m} > 300$ μJy and $z \geq 2$ which would fall in our target range in $S_{1.4\mathrm{GHz}}$.

We did not include the 3.6-μm criterion as such in the modelling of the type-1 quasars, since it is designed to remove type-1 quasars. Instead, we take this criterion to guarantee type-2 quasars, and as a photometric redshift cut of $z \gtrsim 1.4$. We therefore only consider type-1 quasars above this photometric redshift, but since there is a large uncertainty in this cut, and we could plausibly have missed out type-2 quasars at $z \sim 1.4$, we decide to implement the cut at the higher redshift of $z \geq 2.00$. This choice is due to three reasons: the quasar activity peaking around this redshift, selection at 24-μm disfavouring quasars at $z \sim 1.5$ and Ly α only becoming visible to optical spectrographs at $z \gtrsim 1.7$. The cut at $z \geq 2.00$ prevents our analysis from being flawed due to incompleteness in our sample.

The distribution, $\mathrm{p}(\langle N_1 \rangle)$, was derived using the Wolf et al. (2003) type-1 luminosity function at 145 Å, $\phi(M_{145})$, where $M_\mathrm{B} = M_{145} + 1.75$ for a quasar. The 24-μm flux density limit (300 μJy) was converted to a luminosity density limit, at a frequency $\nu_{24} = (1+z)c/(24 \times 10^{-6})$ Hz as a function of redshift by using

$$L_{\nu_{24}} = l_\mathrm{d}^2 \times 300 \times 10^{-32}/(1+z) \text{ W Hz}^{-1} \text{ sr}^{-1} \tag{4.1}$$

where l_d is the luminosity distance (e.g. Peacock, 1999). From this luminosity at rest-frame 24/(1+z) μm, and from the Rowan-Robinson (1995) SED, a B-band luminosity density and absolute magnitude were derived. The fraction of sources that would fall inside the radio criteria was modelled by assuming the sources to follow the gaussian distribution of radio-to-optical ratios for radio-quiet quasars of Cirasuolo et al. (2003). This relates the $\log_{10}$ B-band and 1.4 GHz luminosity densities via a ratio, R, which has a lognormal distribution, so

$$\log_{10}(\mathrm{L}_{1.4}/\text{W Hz}^{-1} \text{ sr}^{-1}) = R \log_{10}(L_\mathrm{B}/\text{W Hz}^{-1} \text{ sr}^{-1}) \tag{4.2}$$

and

$$\mathrm{p}(R) = A\mathrm{e}^{\frac{-(R-\mu_R)^2}{2\sigma_R^2}}, \tag{4.3}$$

where A is a normalisation term. Cirasuolo et al. (2003) found the best-fit values for radio-quiet quasars to be $\mu_R = -0.5$ and $\sigma_R = 0.75$. The number of sources expected to meet our 24-μm and radio criteria, given an infrared and a radio spectral index ($\alpha_{\rm IR}$ and $\alpha_{\rm rad}$ respectively) was therefore:

$$\mathrm{p}(\langle N_1\rangle|\alpha_{\rm IR},\alpha_{\rm rad}) = \int_{z=2}^{z=5}\mathrm{d}z\int_{M_1}^{M=-34}\mathrm{d}M_{145}\,\frac{\mathrm{d}V}{\mathrm{d}z}\phi(M_{145},z)\int_{R_1}^{R_2}\mathrm{d}R\,\mathrm{p}(R)\,R(M_{145}+1.75), \tag{4.4}$$

where, at a given z, M_1 is the magnitude that corresponds to the 24-μm flux-density limit of 300 μJy, given $\alpha_{\rm IR}$, and $M = -34$ is a magnitude above which we can safely ignore the number density of AGN. At a given z and magnitude, R_1 and R_2 are the ratios that correspond to the 1.4 GHz limits of 350 μJy and 2 mJy respectively, given $\alpha_{\rm rad}$.

We assumed a radio spectral index $\alpha_{\rm rad} = 0.80$ (where flux density $\propto \nu^{-\alpha_{\rm rad}}$, see Chapter 5) and estimate the possible range between $\alpha_{\rm rad} = 0.50$ and 1.00. For the conversion between observed 24-μm flux densities and restframe B-band luminosities, we assumed a spectral index $\alpha_{\rm IR} = 1$ and vary the range between $\alpha_{\rm IR} = 0.85$ and 1.15 (Neugebauer et al., 1987). We also assumed pure luminosity evolution (as this allows us to predict exactly the number of type-1 quasars of Zheng et al. (2004), which gives us confidence in our method) and quantified uncertainties by varying between pure luminosity evolution and pure density evolution for the luminosity function of Wolf et al. (2003). All the errors were then combined in quadrature.

The approximation of $\mathrm{p}(\langle N_1\rangle) = 4.3^{+2.2}_{-1.1}$, represents the number of type-1 quasars expected to adhere to both our 24-μm and 1.4-GHz selection criteria, and with $z \geq 2$ in a 3.8 deg^2 patch; this number would be 15-times higher without any radio selection criteria. To obtain the normalised posterior probability $\mathrm{p}(q|\mathrm{data},\{\mathrm{Type}-1\ \mathrm{quasar}\})$ we use Bayes' theorem with a uniform prior over the range $0 \leq q \leq 1$ so that

$$\mathrm{p}(q|\mathrm{data},\{\mathrm{Type}-1\ \mathrm{quasar}\}) = \mathrm{p}(\mathrm{data}|q,\{\mathrm{Type}-1\ \mathrm{quasar}\}). \tag{4.5}$$

We then calculated this likelihood function, at each q, as a Poisson distribution for the observed (integer) number of type-2 quasars at $z \geq 2$ where the mean number expected $\langle N_2\rangle = (1-q)\langle N_1\rangle/q$. Because of uncertainties in the background information on $\langle N_1\rangle$, we had to evaluate the likelihood at each q and $\langle N_1\rangle$ and then marginalise over N_1. This bayesian approach allowed

us to account properly for small number statistics, but note that Poisson sampling fluctuations were correctly excluded from the error budget because we were interested in $\langle N_1 \rangle$ and not the patch-to-patch variance of N_1.

Figure 4.2 shows the resulting conditional probability distribution of the quasar fraction q given our new data on type-2 quasars and our background knowledge of the type-1 quasar population, namely p(q|data, {type $-$ 1 quasar}). It is difficult to judge whether the blank-spectrum objects with photometric redshifts $z_{\rm phot} > 2$ should be included (dashed red line in Figure 4.2) until we know more about the dust content of their host galaxies, but considering just the objects with spectroscopic redshifts (solid blue line in Figure 4.2) is clearly a conservative estimate.

There are 5 narrow-line objects in our sample with spectroscopically confirmed $z \geq 2.00$, and the quasar type-2 to type-1 ratio for narrow-line (torus-obscured) type-2s and type-1 quasars is therefore $\sim$1:1. For the blank objects, the crude photometric redshifts can be used to estimate, on average, how many blank (host-obscured) objects are at $z \geq 2$. There is one extra object with confirmed spectroscopic redshift $z_{\rm spec} = 2.25$ from Spitzer IRS, and 4 blank objects with $z_{\rm phot} \geq 2.00$. Therefore the current estimated number of objects at $z \geq 2.00$ is 10. From the errors in the modelled number of type-1 quasars, and the Poisson errors in our sample, the ratio of type-2 to type-1 quasars is found to be $2.3^{+1.8}_{-1.2}$.

The most likely systematic problem with our analysis is that we have implicitly assumed identical radio properties for type-1 and type-2 quasars matched in intrinsic luminosity. However, unified models predict Doppler-boosted radio emission from the weak jets aligned closer to the line-of-sight for type-1 quasars (Baker et al., 2002) and hence, on average, lower radio luminosities for type-2 quasars. This would yield lower derived values of q and strengthen our conclusion that most quasars are obscured. It is of course possible to postulate that the optical-to-radio correlation evolves with redshift, but this is currently an unknown. It is also possible that we are missing type-2 quasars with an extreme obscuring column ($A_{\rm V} \gtrsim 50$) which could be due, for example, to the obscuring torus being completely edge-on to the line of sight, but this would only strengthen our result. Similar spectroscopic studies of radio-loud type-2 quasars (Rawlings et al., 2001) almost always yield narrow emission lines, presumably because extended radio sources clear dust and gas from the inner part of the host galaxy (Baker et al., 2002).

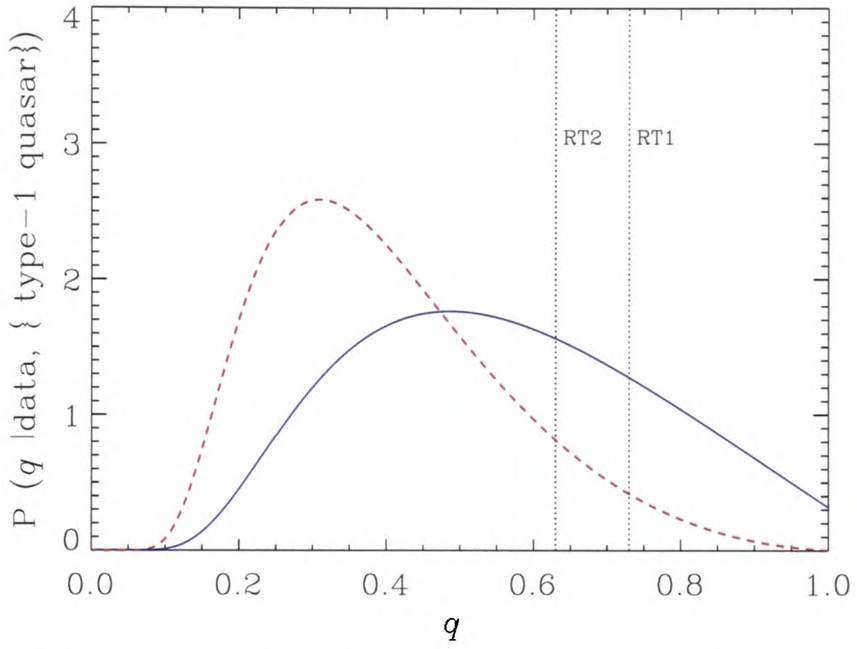

Figure 4.2: Probability distributions for the quasar fraction. The normalised posterior probability $p(q|\text{data}, \{\text{type}-1\ \text{quasar}\})$ of the quasar fraction q given our new data on type-2 quasars, and background information on type-1 quasars. The two lines represent different interpretations of the number of type-2 quasars at $z \geq 2$ determined from our new data. The solid blue line is the posterior probability if we believe the only candidates with $z \geq 2$ are the 5 whose optical spectroscopic redshifts confirm this. If, additionally, we use the redshifts from Spitzer-IRS (so we include the $z = 2.25$ object), and photometric redshifts of the rest of the candidates with blank spectra (4 additional candidates with $z \geq 2$), then we obtain the red curve. The best estimate for q is probably somewhere between the two curves. The two vertical lines represent the predictions of receding torus models, one with a fixed torus height (marked 'RT1' Simpson, 1998a) and one ('RT2') with a torus height varying with luminosity (Simpson, 2005).

4.2 Discussion

The median redshift of our spectroscopic sample is at $z = 2$ which is exactly where the optical luminosity density of the type-1 quasar population is at its peak (e.g. Wolf et al., 2003). Our sample shows that during this 'epoch of quasar activity' we can be confident that about half of all high-luminosity quasars are obscured and if some of the blank-spectrum objects turn out to have $z \gtrsim 2$ then it is likely that type-2 quasars outnumber type-1 quasars by a significant factor. This is the first direct detection of a high-redshift type-2 quasar population likely to outnumber the type-1 population.

We compare our results with unified schemes (Antonucci, 1993) by considering models in which, for type-2 objects, a dusty torus obscures direct view of the quasar nucleus. Our preferred value $q = 0.2 - 0.4$ (see Figure 4.2) implies a torus half-opening angle $\theta \approx 20° - 40°$ for $z \gtrsim 2.0$ quasars. At first sight this does not sit easily with the 'receding torus' models (Lawrence, 1991; Simpson, 1998a, 2005) in which the solid angle subtended by the torus decreases, and hence q increases, systematically with increasing quasar luminosity. As our selection criteria select luminous quasars, the torus should have receded to the point that $q \approx 0.6$. We suggest that the resolution of this problem is that there is increased kpc-scale dust obscuration affecting both the nuclear and narrow-line regions in some fraction of $z \sim 2$ quasars: the 'host-obscured' sources. This would explain why a good fraction of our optical spectra were completely blank. Thus, receding torus models should only be compared to the quasar fraction inferred from type-1 and 'torus-obscured' quasars: the solid blue line (with $q \approx 0.4$) and these models are perfectly consistent with the data.

The 'two types of type-2' quasar, and a type-1 quasar are schematically represented in Figure 4.3. For a quasar to be of type-1 it has to lie in a relatively dust free galaxy (a 'transparent' galaxy) as well as having a favourable orientation to the torus (case A in Figure 4.3). A quasar in a transparent galaxy, with an unfavourable angle to the torus will not outshine its host galaxy, but the narrow-line region will still be visible (case B: a torus-obscured type-2). When the host galaxy is dusty enough to obscure the quasar (cases C and D) it is no longer possible to see the central region, whether we have a favourable angle to the torus (C) or not (D). Objects of case C and D are likely to yield blank spectra, and are indistinguishable from each other with the current dataset. Observations at radio frequencies, however, could shed some light on the orientation if

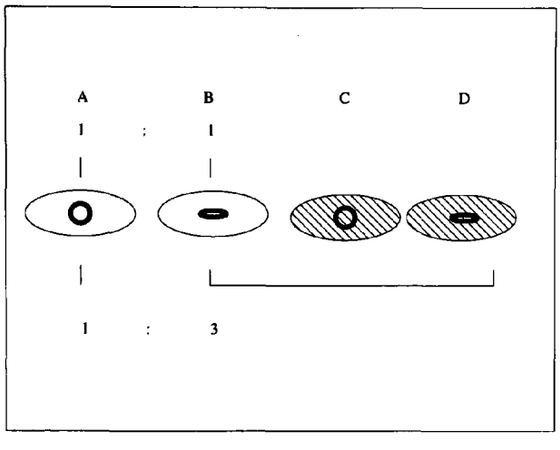

Figure 4.3: Schematic representation of the three types of quasar. The empty ellipses represent a transparent host galaxy, while the filled ellipses representing dusty ones. The solid black circle represents the torus around the quasar. A is hosted by a transparent galaxy, and since we are viewing the torus face on, we can see the broad line region. It is a type-1 quasar. B is also hosted by a transparent galaxy, but since the torus is edge on, we only see the narrow line region. This is a torus-obscured type-2. C has a favourable geometry, while in D the torus is in the line of sight, but since both are obscured by large-scale dust in the galaxy, we cannot see the central region, so they are both host-obscured type-2s. We have found the ratio of B to A to be ~1:1, and the ratio of B,C and D (together) to A to ~2-3:1. We note that although we are calling C and D 'host'-obscured, the dust could plausibly be due to a nuclear starburst, with a characteristic scale ~ 100 pc, as well as a galaxy-scale starburst.

radio jets are present (Chapter 5).

This simple picture is likely to be applicable only to radio-quiet objects, since the powerful radio jets are likely to be capable of removing dust on large scales (Baker et al., 2002; Willott et al., 2002a). Therefore, although the ratio of type-2 to type-1 is likely to be ~2-3:1 for radio-quiet samples (and for all non-radio-selected samples, since radio-quiet objects will dominate), it should be closer to 1:1 for radio-loud samples. Thus radio-loud samples will have few 'host-obscured' quasars (cases C and D, although some are probably present in the sample of Willott et al., 2001) and the quasar fraction measured in these radio-loud samples will be dominated by the geometry of the torus. This picture is therefore consistent with the ratio of narrow-line to broad-line quasars predicted by unified models and found for radio-loud objects (~1:1 e.g Willott et al., 2000a).

As stated earlier, inferring a type-2 to type-1 ratio ~2-3:1 for the sample presented in this article does not disagree with the receding-torus models (e.g. Lawrence, 1991; Simpson, 2005), since the obscuring mechanism for 'host-obscured' type-2s is unrelated to the torus orientation or geometry. The ratio of torus-obscured (B) to type-1 (A) quasars predicted for our sample is ~1:1

(and indeed consistent with the receding-torus: Figure 4.3). This phenomenon of host-obscuration might also be present in the Seyfert-2s at $z \sim 1$ that dominate the hard X-ray background, in which case care must be taken to separate the obscuring mechanism necessary to explain the AGN dominating the X-ray background from modifications to the unified schemes such as the receding torus.

The ratio of ~2-3:1 found for this sample is similar to the ratio required for Seyfert-2s to Seyfert-1s at $z \sim 1$ to fit the hard X-ray background, although a ratio ~2-3:1 for the quasars is not required by the hard X-ray background (Ueda et al., 2003; Treister & Urry, 2005). We do note, that due to the range in gas-to-dust ratios, some of the X-ray obscured quasars that contribute to the hard X-ray background are not necessarily type-2s in the optical sense (they might only be reddened quasars with $A_V \sim 1 - 5$ but a large gas-to-dust ratio). However, at least in our sample, we find the ratio of all type-2s (B, C and D) to type-1 (A) is ~2-3:1: a higher type-2 to type-1 ratio than is found in deep X-ray surveys. This suggests that indeed, 24-μm selection can find type-2 quasars that X-ray selection in the 2-10 keV band has not been able to detect, and therefore a number of the type-2 quasars presented here should be Compton-thick. This, of course, can be tested via X-ray follow-up of this or a similar sample (see Chapter 6).

To conclude, we have found that 50-80% of the accretion onto high-redshift SMBHs is obscured. If we consider our results alongside those of the X-ray surveys at lower redshifts ($z \lesssim 2$, Barger et al., 2005) and studies of the hard X-ray background (e.g. Worsley et al., 2005), which find that most accretion at low redshift occurs in type-2 Seyferts. We deduce that throughout cosmic history, black hole growth seems to have been concentrated in obscured regions. This implies, from comparisons between the integrated luminosity density of quasars (both type-1 and type-2) and the local space density of relic black holes (Yu & Tremaine, 2002), that black hole growth occurs in short, efficient spurts.

Chapter 5

Radio properties

The sample presented in Chapter 3 consists of $z \sim 2$ radio-intermediate type-2 quasars: quasars with radio luminosities below the FRI/FRII break, but above that would be expected from star-formation alone. We have found secure optical redshifts (from narrow lines) for $\sim 50\%$ of the sample with the remaining optical spectra typically completely blank. In Chapter 4, we discuss the possibility of the blank optical spectra being due to a dusty host galaxy obscuring all the central activity, including narrow emission lines, and label these as "host-obscured" type-2 quasars.

Radio observations can be used to test this scenario since in such host-obscured objects the obscuration should be independent of the orientation. The first expectation is that the radio jets, if present, are randomly oriented. This predicts that a small fraction of host-obscured sources should have the jet close to the observer's line of sight, although this will, of course, be boosted by a radio selection criterion. Hence, some flat-spectrum sources are expected, but only amongst the type-2 quasars with blank optical spectra.

The objects that show narrow emission lines ("torus-obscured") are expected to have the jets at a large angle to the line of sight, and are therefore expected to have steep spectra. Therefore, the suggestion by Miller, Rawlings & Saunders (1993) and Falcke, Malkan & Biermann (1995) that the radio-intermediate quasar population is comprised of Doppler-boosted flat-spectrum radio-quiet quasars would pose serious difficulties for the narrow-line type-2 quasars in this sample. Finally, if the jets in some of the sources were recently triggered, then GHz-peaked spectra, characteristic of young jets (O'Dea, 1998), are expected.

In this Chapter, we describe the results of observing the entire sample at 610 MHz and 4.9

GHz, combined with the public data at 1.4 GHz. We also discuss the conclusions on orientation or age that can be inferred. The observations and data reduction of the 610 MHz dataset were carried out by Timothy Garn and Dave Green but are included here for completeness.

5.1 Observations and data reduction

5.1.1 1.4 GHz dataset

The 1.4 GHz data, taken from Condon et al. (2003), were part of the dataset used to select the sample in the first place (Chapter 2 and Martínez-Sansigre et al., 2005). The 1.4 GHz survey of the FLS was carried out using the Very Large Array (VLA) in B-configuration, with a synthesised beam size of $\approx 5 \times 3$ arcsec^2. The root mean square (rms) noise achieved was ~ 23 μJy and the type-2 quasars were selected in the flux density range 350 $\mu\text{Jy} \leq S_{1.4} \leq 2$ mJy, so all objects are detected at the 15σ-level or higher. At 1.4 GHz, all the sources are point-like, except for AMS16, which has a slightly extended radio structure and AMS04 which has an adjacent radio source North-East (NE) which could plausibly be a jet. Several of the sources were also observed in the WSRT survey of Morganti et al. (2004) and comparison of the flux densities suggested no hints of extended radio structure (other than AMS04), as we saw in Chapter 3.

5.1.2 4.9 GHz dataset

The 4.9 GHz data were also obtained using the VLA, but this time through pointed observations of every object in the sample, except AMS08 which was observed in the field of view of AMS03. Making use of dynamical scheduling time, we observed our 21 sources during July and August 2005, while the VLA was changing from B to C configuration. The data presented here were effectively taken in C configuration. The observations were scheduled to optimise the coverage of the *uv* plane. Sources were observed for 2-3 minutes at a time, with visits to the phase calibrators every 9-12 minutes. The amplitude calibrators 3C48 or 3C286 were observed once every 1-2 hours, and at least once per observing run. Overall, all sources were observed for almost exactly the same length of time, about 17 minutes each (except AMS10 which was observed for twice as long). With the VLA typically having $\sim$ 25 working antennae each run, the expected thermal noise was $\sim$45 μJy ($\sim$ 32 μJy for AMS10).

The reduction of the 4.9 GHz data was peformed using AIPS. Each run was reduced individually in the same way. The first 10 seconds of each scan were deleted, and visibly bad data-points were removed; dead antennae and bad periods of time of individual antennae were also flagged. The data were calibrated for amplitude using either 3C48 or 3C286, and for phase using either 1638+625 or 1756+578. The sources themselves are too faint for self-calibration but some of the pointings include sources bright enough ($\sim$10 mJy) to allow tests for phase stability: the phases varied by $\lesssim 10^{\circ}$ in the 9-12 minute intervals between visits to the phase calibrator so, even where possible, self-calibration would have little effect on the final image.

The calibrated *uv* files of individual sources in individual runs were then combined and imaged. The beam size was $\approx$4$\times$3 arcsec^2, well matched to the 1.4 GHz beam, and the rms noise in the central region of all the images was found to be 50-54 μJy (37 μJy for AMS10), close to the expected thermal noise. A primary beam correction was applied in the case of AMS08, since this source is at the edge of the image of AMS03. At 4.9 GHz, all detected sources are unresolved and point-like, except AMS04 which is slightly extended ($\approx 6 \times 3$ arcec^2) in the NE to SW direction.

5.1.3 610 MHz dataset

The FLS region was observed in 2004 March with the Giant Meterwave Radio Telescope (GMRT). Seven pointings were observed, one central pointing, and six in a surrounding hexagonal grid, separated by 43 arcmin. Each pointing was observed for several scans of $\approx$ 200 minutes, spread over 4 ten-hour observing sessions made between March 23rd and 27th. The flux density scale of the observations were tied to observations of 3C48 and 3C286 made at the start and end of each observing run (with assumed flux densities at 610 MHz of 29.4 and 21.1 Jy respectively). The nearby source 1634+627 was observed between the observation of each FLS pointing, to monitor any phase and amplitude variations of the telescope. The data were calibrated using standard techniques using AIPS, and images synthesised. Given the relative large field of view of the GMRT compared with its resolution – primary beam half-width of 44.4 arcmin, with a resolution of $\approx$ 5 arcsec – 19 facets were used to image each pointing, including several interations of self-calibration. The rms noise on these images varied between 28 and 32 μJy beam^{-1} before primary beam correction, although dynamic range limitations means that the noise close to bright sources is larger. Comparison of the flux densities of sources in the overlap regions between pointings,

Name	$S_{4.9\mathrm{GHz}}$ /μJy	$S_{1.4\mathrm{GHz}}$ /μJy	$S_{610\mathrm{MHz}}$ /μJy	$\alpha_{1.4}^{4.9}$	$\alpha_{610}^{1.4}$
AMS01	164 ± 52	490 ± 31	1167 ± 165	$0.87^{+0.35}_{-0.27}$	$1.04^{+0.13}_{-0.13}$
AMS02	408 ± 52	1184 ± 55	2985 ± 152	$0.85^{+0.15}_{-0.13}$	$1.11^{+0.08}_{-0.08}$
AMS03	365 ± 53	1986 ± 87	5180 ± 191	$1.35^{+0.16}_{-0.14}$	$1.15^{+0.07}_{-0.07}$
AMS04A†	135 ± 53	536 ± 72	1092 ± 77	$1.10^{+0.50}_{-0.38}$	$0.86^{+0.26}_{-0.24}$
AMS04B‡	232 ± 106	867 ± 101	1519 ± 122	$1.05^{+0.58}_{-0.40}$	$0.68^{+0.24}_{-0.23}$
AMS05	443 ± 51	1038 ± 49	1214 ± 164	$0.68^{+0.14}_{-0.13}$	$0.19^{+0.13}_{-0.13}$
AMS06	191±53	444 ± 31	1115 ± 153	$0.67^{+0.31}_{-0.25}$	$1.11^{+0.14}_{-0.14}$
AMS07	239 ± 51	354 ± 27	578 ± 151	$0.31^{+0.25}_{-0.22}$	$0.59^{+0.20}_{-0.20}$
AMS08	<718	655 ± 36	889 ± 151	>-0.07	$0.37^{+0.21}_{-0.22}$
AMS09	174 ± 51	426 ± 29	1118 ± 190	$0.71^{+0.33}_{-0.26}$	$1.16^{+0.18}_{-0.18}$
AMS10	501± 36	1645 ± 73	4590 ± 93	$1.04^{+0.13}_{-0.12}$	$1.24^{+0.74}_{-0.07}$
AMS11	<104	356 ± 29	628 ± 89	>0.98	$0.68^{+0.21}_{-0.21}$
AMS12	305 ± 83	946 ± 45	2440 ± 194	$0.90^{+0.19}_{-0.17}$	$1.14^{+0.10}_{-0.94}$
AMS13	495 ± 80	1888 ± 83	4559 ± 135	$1.07^{+0.18}_{-0.16}$	$1.06^{+0.07}_{-0.72}$
AMS14	158 ± 52	469 ± 29	1099 ± 196	$0.87^{+0.37}_{-0.28}$	$1.03^{+0.14}_{-0.14}$
AMS15	326 ± 53	440 ± 29	570 ± 174	$0.24^{+0.19}_{-0.17}$	$0.31^{+0.23}_{-0.25}$
AMS16	<108	390 ± 60	<170	>1.02	<-1.00
AMS17	265 ± 53	615 ± 34	1354 ± 226	$0.67^{+0.22}_{-0.19}$	$0.95^{+0.18}_{-0.19}$
AMS18	212 ± 53	390 ± 29	502 ± 113	$0.49^{+0.29}_{-0.24}$	$0.30^{+0.25}_{-0.26}$
AMS19	506 ± 52	822 ± 41	958 ± 152	$0.50^{+0.18}_{-0.16}$	$0.18^{+0.17}_{-0.17}$
AMS20	1391 ±53	1268 ± 58	674 ± 187	$-0.07^{+0.07}_{-0.07}$	$-0.76^{+0.32}_{-0.40}$
AMS21	145 ± 53	449 ± 29	1019 ± 169	$0.91^{+0.42}_{-0.30}$	$0.99^{+0.16}_{-0.16}$

Table 5.1: Radio data for the entire sample. The integrated fluxes with errors are from the AIPS tasks IMFIT, SAD and JMFIT (for 4.9 GHz, 1.4 GHz and 610 MHz respectively). †The properties of AMS04 without the flux density of the source at 17 13 41.20 +59 49 24.0 which might be an extended component of AMS04. ‡The properties of AMS04 including the flux density of the possible extended component.

after correction for the nominal primary beam of the GMRT, revealed systematic inconsistencies between adjacent pointings. The differences could be explained by a consistent offset for the primary beam of the GMRT compared with the phase centre of each observation, of about 3 arcmin. Consequently, an offset primary beam correction was made to each of the pointings, before determining flux densities for the sources.

At 610 MHz all sources are point-like, except AMS04. In this case the adjacent radio source is detected, and the gaussian fit to the combined object results in a 10.3 × 5.1 arcsec^2 ellipse, at a position angle of 40 degrees (North through East).

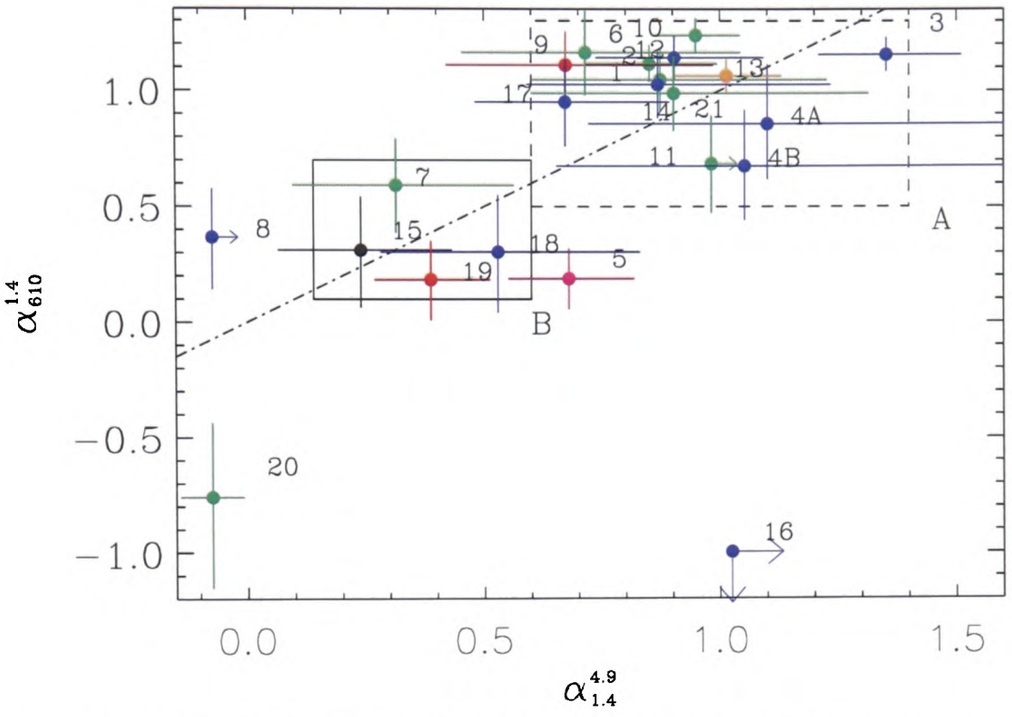

Figure 5.1: Spectral index between 610 MHz and 1.4 GHz, vs spectral index between 1.4 and 4.9 GHz. The numbers identify each source: blue indicates sources with narrow-emission lines in their optical spectra; green, sources with blank optical spectra; the black point (AMS15) has not been observed with optical spectroscopy; red, the two objects (AMS06 and AMS19) with blank optical spectra, but spectroscopic redshifts from Spitzer-IRS; yellow shows AMS13, which has narrow lines in the optical, as well as a redshift from Spitzer-IRS; pink, AMS05, with narrow lines in the optical, but no redshift obtained from Spitzer-IRS. The line $\alpha_{610}^{1.4} = \alpha_{1.4}^{4.9}$ and Boxes A and B have been drawn to aid the discussion of Section 5.2

5.2 The spectral indices of the sample

The spectra of our sample are described here using two power laws, with flux density $S_\nu \propto \nu^{-\alpha}$. The spectral index between 1.4 and 4.9 GHz ($\alpha_{1.4}^{4.9}$) and between 610 MHz and 1.4 GHz ($\alpha_{610}^{1.4}$) are given in Table 5.1. The flux densities used are all integrated quantities from gaussian-fitting procedures. Since the beam sizes at the three frequencies are well matched, and the sources are generally point-like, the spectral indices measured here are not strongly affected by problems such as confusion, or resolving out some of the flux density.

Table 1 summarises the data and Fig. 5.1 shows $\alpha_{610}^{1.4}$ plotted against $\alpha_{1.4}^{4.9}$. The colours indicate the optical and mid-infrared spectroscopic properties of the sources. Fig. 5.2 shows the luminosity

at 1.4 GHz as a function of redshift for the sample. Objects with no spectroscopic redshift are placed at $z = 2$. The 1.4 GHz luminosities of the sources were calculated using the spectral index $\alpha_{610}^{1.4}$ to convert from observed-frame to rest-frame 1.4 GHz. The dashed lines show the luminosity of the FRI/FRII break (Fanaroff & Riley, 1974, converted from 178 MHz to 1.4 GHz) and the luminosities expected for pure starbursts (Condon, 1992). The two 1.4 GHz flux density cuts used in our selection are also plotted. For all these, we assume $\alpha = 0.8$. The difference in spectral indices between the measured ones and the value assumed for the flux density cuts explains why some sources fall outside the expected selection locus.

The star-formation rates are quoted for stars more massive than 5 $M_\odot$, and require an initial mass function (IMF) to to convert to the total star-formation rate. The conversion factor, Q is given by

$$Q = \frac{\int_{M_1}^{M_2} M\Psi(M)dM}{\int_{5M_\odot}^{M_2} M\Psi(M)dM} \tag{5.1}$$

where Ψ(M) is the IMF, with M_1 and M_2 as the minimum and maximum stellar masses. If we assume M_1 =0.25 $M_\odot$ and M_2 =100 $M_\odot$ and a Salpeter IMF (Salpeter, 1955, where $\Psi(M) \propto M^{-2.35}$) then $Q = 3.9$. The star-formation rates due to massive stars, 300 $M_\odot$ yr^{-1} and 1000 $M_\odot$ yr^{-1}, would then correspond to total star-formation rates of 1170 $M_\odot$ yr^{-1} and 3900 $M_\odot$ yr^{-1} respectively.

5.2.1 Steep-spectrum sources

Looking at Fig. 5.1, the majority of the sources have steep ($\alpha \sim 1$) indices in both intervals and the two indices have similar values. Considering objects in Box A, $\langle\alpha_{1.4}^{4.9}\rangle = 0.91 \pm 0.18$ and $\langle\alpha_{610}^{1.4}\rangle = 1.0 \pm 0.14$. This group includes objects with optical narrow lines and blank optical spectra. To test for any trends, we assume the hypothesis that all 13 sources in box A are realisations of the same underlying binomial distribution and have an ~50% chance of having narrow-emission lines; 6 out of 13 objects in Box A have emission lines which is obviously consistent with our hypothesis. Dividing the sources in two by splitting the Box by the median $\alpha_{1.4}^{4.9}$, $\alpha_{610}^{1.4}$ or by a diagonal median, we can test for trends, this time assuming the 6 sources in each half are drawn from this underlying distribution. In this case, deviations from 90% confidence would require one

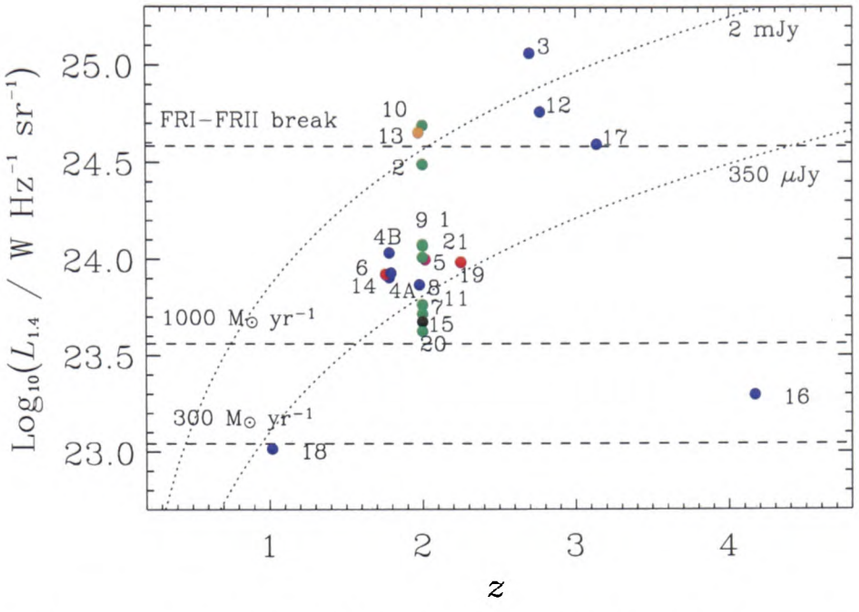

Figure 5.2: The luminosity at 1.4 GHz plotted against redshift. The colour coding is the same as for Fig. 5.1. The dotted lines indicate the radio criteria used in the selection of the sample and the dashed lines the FRI/FRII break and the radio luminosity due to star-formation rates of 1000 and 300 $M_\odot$ yr^{-1} in stars more massive than 5 $M_\odot$.

or zero sources of a given type, but each division always yields at least 2 sources of one or the other type. We can conclude that there is no trend or correlation between spectral index and optical properties in the sources in Box A.

In Fig. 5.2, we see several of these steep-spectrum sources (AMS03, AMS12, AMS13, AM17 and AMS10 if it is at $z \sim 2$) have radio luminosities around the FRI/FRII break. Since our objects are selected to be type-2 quasars, we have possibly found some highly accreting FR-I radio sources, which although a small fraction of the low-z FRI population, are not unknown (see Blundell & Rawlings, 2001, and Heywood, Blundell & Rawlings, submitted). In the case of AMS04, we tabulate and plot two sets of values, derived with (A) and without (B) the adjacent radio source at 17 13 41.20 +59 49 24.0 which could plausibly be a ~10 arcsec jet associated with the type-2 quasar. Including the jet lowers both indices, particularly $\alpha_{610}^{1.4}$, but the source is still clearly steep in both ranges.

Since the 1.4 GHz luminosities are similar to those of FR-Is, we compare the spectral indices of our sample to those compiled for the (178-MHz selected) 3C sample by Laing & Peacock (1980).

At $z = 2$, observed 610 MHz and 1.4 GHz correspond to rest-frame 1.8 and 4.2 GHz respectively, so the spectral indices between 750 MHz and 5 GHz presented by Laing & Peacock (1980) for sources at $z \lesssim 0.03$ include the range corresponding to our $\alpha_{610}^{1.4}$. They find typical spectral indices between 0.6 and 1.0 for FRI sources with values of $L_{1.4}$ between $10^{23.5}$ and 10^{25} W Hz^{-1} sr^{-1}. The values of $\alpha_{610}^{1.4}$ presented here are clustered towards the high end of the Laing & Peacock range. This is the reverse of what one expects from the most obvious selection effect: since the 3C sources are selected at lower frequency, one expects them to have steeper indices than a 1.4 GHz-selected sample. This could be explained by a combination of effects: e.g. the single-power-law spectra of Laing & Peacock goes down to 750 MHz and spectral indices typically steepen at higher frequencies; the radio-source environments at low redshift are systematically different from those at high redshift; and the cosmic microwave background (CMB) energy density is significantly higher at $z \sim 2$.

Steep straight spectra with $\alpha \sim 1$ are characteristic of the continuous injection of relativistic electrons accompanied by synchrotron & inverse-Compton losses (Kardashev, 1962). We can speculate that the electrons are accelerated in the knots of FRI-like sources and have $\alpha \sim 1$ because each has a (rest-frame) spectral 'break frequency', $\nu_{\rm break}$ (where radiative losses steepen the negative slope of the number density of particles versus energy, and hence steepen the emitted spectrum) which has been driven below $\sim$ 1 GHz by the high value of the $z \sim 2$ CMB energy density.

The relevant equation (Eqn. 3.10 of Leahy, 1991) is

$$\nu_{\rm break} = (9/4)\left(\frac{1.12 \times 10^3 B_{\rm source}}{[B_{\rm source}^2 + B_{\rm CMB}^2]^2 t_{source}^2}\right) {\rm nT^3 Myr^2}, \qquad (5.2)$$

where $B_{\rm CMB} = 0.318(1+z)^2$ nT, and $B_{\rm source}$ and t_{source} are the characteristic magnetic field and age of the source respectively. At $z \sim 2$, $B_{\rm CMB} \sim 3$ nT. From minimum energy arguments, assuming $L_{1.4} = 10^{24}$ W Hz^{-1} sr^{-1} and a characteristic size of 30 kpc, then $B_{\rm source} \sim 1 - 2$ nT depending on the shape of the emitting region. Therefore a 10 Myr-old source at $z = 2$ will have rest-frame $\nu_{\rm break} \sim 300$ MHz due to the high value of the CMB energy density.

5.2.2 Flat spectrum sources

Another visible group is Box B in Fig. 5.1 which has $\alpha \lesssim 0.5$ in both radio spectral intervals. This includes the sources AMS15, AMS18 and AMS19, more arguably AMS07, and maybe AMS08. Flat ($\alpha \lesssim 0.5$) spectral indices in both frequency ranges suggest that the jets are close to the observer's line of sight with Doppler boosting of compact jet knots leading to a flat spectrum. In a unified scheme, such objects are not expected to be obscured by the torus, so any dust is expected to be on a larger scale, presumably in the host galaxy. This picture is consistent for AMS07 and AMS19 which have no narrow emission lines in their optical spectra, and could presumably be being obscured by dust in the host galaxy; AMS15 has not been observed spectroscopically. In Fig. 5.2, AMS07, AMS15 and AMS19 are seen to have 1.4 GHz luminosities consistent with radio-intermediate type-2 quasars: too high for star-formation only (unless they are hyper-luminous infrared galaxies) but below the FRI/FRII break.

AMS18 has a 1.4 GHz luminosity consistent with a pure starburst with a massive-star-formation rate of only ~ 300 $M_\odot$ yr^{-1}. Such an object could plausibly make it through our selection criteria and indeed AMS18 has an atypical optical spectrum showing only an [O II] 3727 Å line and other low-ionization lines like C II] (2326 Å) and Mg II (2798 Å). No high-ionization lines are securely detected (see Figure 3.1) so AMS18 could well be a pure starburst. If the radio emission is indeed due to the starburst, then the flat spectral indices can be explained by a bremsstrahlung contribution.

AMS08 has a flat spectrum between 1.4 GHz and 610 MHz ($\alpha_{610}^{1.4} = 0.37$) but the limit obtained for $S_{4.9\mathrm{GHz}}$ is of little use in constraining $\alpha_{1.4}^{4.9}$. Since it has narrow lines in the optical, a flat value for $\alpha_{1.4}^{4.9}$ would suggest a beamed jet and would not sit easily with the obscuration by the torus. However, a steep value ($\gtrsim 0.7$) could be explained as a GHz-peaked source, in the same was as for AMS05 (see Section 5.2.3).

5.2.3 GHz-peaked sources

Finally, there are three more sources with different spectral properties from those in Boxes A and B: AMS05; AMS16; and AMS20. These spectral properties can be explained as being due to young, compact jets, with synchrotron self-absorption leading to GHz-peaked spectra (GPS; see

O'Dea, 1998, for a review). AMS20 has $\alpha_{610}^{1.4} = -0.76$ and $\alpha_{1.4}^{4.9} = -0.07$ suggesting the spectrum peaks somewhere above observed 4.9 GHz. We do not have a spectroscopic redshift for this object since the optical spectrum shows faint red continuum only but it is very unlikely to be at $z < 1$, so the peak is likely to be at a rest-frame frequency of 9.8 GHz or higher. AMS16 (at $z = 4.169$) has a very negative $\alpha_{610}^{1.4}$ and a very positive $\alpha_{1.4}^{4.9}$: it is consistent with peaking around observed 1.4 GHz (rest-frame 7 GHz) and due to the bandwidth narrowing with redshift, the frequencies observed range from rest-frame 25 GHz (observed 4.9 GHz) to rest-frame 3 GHz (observed 610 MHz). In Fig. 5.2 we can see that both AMS16 and AMS20 are intrinsically quite radio-faint at rest-frame 1.4 GHz, placing an interesting limit on any associated massive-star-formation rate ($\lesssim$ 500-1000 $M_\odot$ yr^{-1}).

AMS05 has $\alpha_{610}^{1.4} = 0.19$ and $\alpha_{1.4}^{4.9} = 0.72$ and lies in the 'radio-intermediate' region of Fig. 5.2. The spectral indices can be explained by a GPS source peaking between 610 MHz and 1.4 GHz (observed frequencies).

5.3 Conclusions

We have used radio-data at three different frequencies, with well-matched beam sizes, to study the radio spectral properties of our population of high-redshift type-2 quasars. The sample contains a range of different radio spectral properties, which include mainly steep-spectrum sources ($\alpha_{610}^{1.4}$ and $\alpha_{1.4}^{4.9} \sim 1$), plus a minority of flat steep sources, with ($\alpha_{610}^{1.4} \lesssim 0.5$ or $\alpha_{1.4}^{4.9} \lesssim 0.5$), and three, or perhaps four, GHz-peaked sources. The presence of flat-spectrum sources would be hard to reconcile with obscuration by a torus but we find no secure examples of such a case as there are no narrow-line type-2s with flat radio spectra. Otherwise, we find no correlation between radio spectral properties and optical spectral properties, suggesting no obvious dichotomy between "host-obscured" and "torus-obscured" type-2s, at least in terms of their radio spectral properties.

When determining the radio luminosities of our sources, we find the majority fall below the FRI/FRII break but above the luminosity corresponding to a massive-star-formation rate of 1000 $M_\odot$ yr^{-1}. Although we do not generally have the surface brightness sensitivity to detect extended jets, many of these objects could have FRI-like structures. Only one source has a radio luminosity

consistent with being entirely due to a ~ 300 $M_{\odot}$ yr^{-1} starburst, consistent with its low-ionization-only emission lines. Only 4 out of 21 sources (at most 5 with AMS08) are flat-spectrum sources, so the idea that the radio-intermediate quasar population might be dominated by Doppler boosted radio-quiet quasars (e.g Miller et al., 1993) is not correct for this high-z population.

Interestingly, we find that the steep spectrum ($\alpha \sim 1$) sources have radio spectra consistent with those of low-redshift FRI sources once the effects of an increased CMB energy density is taken into account. The spectral indices can be explained by active, developed jets with continuous injection of relativistic electrons and inverse-Compton scattering by CMB photons, leading to the 'break frequency' being lowered to ~ 0.3 GHz and hence $\alpha \sim 1$ at observed frequencies above $\sim 0.3/(1+z)$ GHz.

Chapter 6

Evidence for Compton-thick quasars

From Chapters 3 and 4, we have found a population of high-redshift type-2 quasars at least as numerous as the type-1 population and which possibly outnumber the type-1s by ~2-3:1. The presence of some type-2 quasars with flat spectra at radio frequencies is consistent with the hypothesis of host obscuration, and suggests that the inferred ratio of ~2-3:1, and not ~1:1, is probably correct. If the type-2 quasars indeed outnumber the type-1s then some of these mid-infrared and radio-selected quasars are expected to be Compton-thick, or else this fraction would have been inferred in hard X-ray surveys. However, no X-ray data are currently available for that sample.

AGN invisible in X-rays were indeed found by Donley et al. (2005), who used a mid-infrared and radio excess criterion to select a sample of AGN. However, the majority of these AGN are at $z \lesssim 1$ and are better described as Seyfert-2s. The authors found that while the sources detected in the X-ray were unlikely to be Compton-thick, the AGN not detected in the X-ray (~20% of their sample) could be Compton-thick. The obscured and gravitationally-lensed quasar IRAS FSC 10214+4724, at $z \sim 2.3$ has been found to be Compton-thick (Alexander et al., 2005a).

Polletta et al. (2006) use two different selection criteria, X-ray and infrared, to look for Compton-thick AGN. Their X-ray selection, which is restricted to sources detected in the X-ray map, finds 5 Compton-thick AGN, of which 2 are spectroscopically-confirmed high-redshift quasars. Of the infrared-selected sources, the strict SED criteria imposed on the sources guarantee AGN, but are likely to exclude heavily obscured ($A_V \gtrsim 20$) high-redshift ($z \geq 1$) sources which do not show power-law mid-infrared spectral energy distributions (SEDs), but have significant

contributions from stellar light at 3.6 and 4.5 μm. It is not surprising, therefore, that they find a smaller Compton-thick fraction ($\sim$10%) than expected in their infrared-selected sample, as it is probably biased against heavily obscured AGN.

The question of whether there is indeed a population of heavily X-ray absorbed high-redshift quasars is therefore still unanswered. Although the dominant contributors to the hard X-ray background (HXB) are $z = 0.5 - 1$ Seyferts, the AGN energy density output at high redshift is dominated by the population around the break in the luminosity function (the quasars). Of particular cosmological relevance is the quasar population at $z \sim 2$, when the quasar activity and the cosmic star-formation rates were at a maximum. As well as helping our understanding of AGN unification models (e.g. Antonucci, 1993), the heavily X-ray absorbed quasars might represent a different phase of the SMBH and host galaxy evolution (e.g. Fabian, 1999).

6.1 Sample selection and dataset

Following the success of the selection criteria described in Chapter 2, we proceed to select a similar sample in the Subaru XMM-Newton Deep Field (SXDF). The small number of objects in the aforementioned sample was due mainly to the radio criterion. In this work we decrease the lower radio flux density criterion, to increase the number of quasars. This is important as here we have a smaller area ($\sim$0.8 deg^2 as opposed to 3.8 deg^2 in the sample of the previous chapters). The selection criteria used here are $S_{24\ \mu\mathrm{m}} > 300$ μJy, $S_{3.6\ \mu\mathrm{m}} \leq 45$ μJy, and 100 μJy $\leq S_{1.4\mathrm{GHz}} \leq$ 2 mJy, which yields 38 candidates. The criteria from Chapter 2 were carefully chosen to avoid starburst galaxies, so the deeper radio selection criterion used here was expected to introduce some contaminants.

As a brief summary, the two mid-infrared criteria are able to target $z \sim 2$ type-2 quasars with $Av \gtrsim 5$, but will also allow $z \lesssim 1$ ultra-luminous infrared galaxies (ULIRGs) in the sample. These ULIRGs will have radio luminosities following the FIR-radio correlation (Condon, 1992), and so by choosing a high-enough radio flux, one can cut out all but the most extreme starbursts. Lowering the radio criterion has the disadvantage that less extreme starbursts are allowed in the sample. The lower the radio criterion, the higher the number of expected ULIRG contaminants. Powerful starbursts are not necessarily expected to be detectable in X-rays, since they might not

contain a powerful AGN, so it is crucial to filter out the ULIRG contaminants before making any conclusion on the X-ray properties of high-redshift type-2 quasars.

The mid-infrared data were obtained by using the SWIRE DR2 (Surace et al., 2005), which covers the SXDF, and has a 5σ flux density limit of $\sim$250 μJy at 24 μm. The SWIRE catalogue does not include sources with $S_{3.6\ \mu\mathrm{m}} < 14$ μJy or $S_{4.5\ \mu\mathrm{m}} < 15$ μJy, so it is possible that our sample is missing a few sources that are very obscured or at very high redshift. From Chapter 3, the fraction of such sources is expected to be small, and we decided to trade missing some sources for the robustness of the SWIRE catalogue. The 1.4 GHz catalogue used is described in Simpson et al. (in press) and Appendix A, and comes from a B-array ($\sim$5×4 arcsec^2 beam) VLA survey with a flux-density limit of 100 μJy ($\sim$5-7 σ).

The spectroscopic completeness of the SXDF is poor at this stage, so we decided to undertake this preliminary study using photometric redshifts. This was much helped by the fact that, for our target objects, the optical to near-infrared light originates from the host galaxy only, as the quasar is severely obscured at these wavelengths. The dataset for this came from two sources. The optical data were obtained from the Subaru B,V,R,i and z imaging (Sekiguchi et al., in prep.). The near-infrared data (J and K) from the UKIDSS (Lawrence et al., 2006) ultra-deep survey (UDS) DR1. The X-ray data were obtained from the XMM-Newton EPIC images (Ueda et al., in prep.).

6.2 Photometric redshifts and filtering out contaminants

In order to disentangle type-2 quasars from ULIRGs and obtain photometric redshifts, the SEDs of the candidates were fitted using a three-component model. The SEDs were assumed to include contributions from warm dust, a stellar population and a "blue" component, the normalisations of which were allowed to vary together with the redshift, although for a given A_V, the normalisation of the warm dust component was fixed to fit the 24 μm data. Two different four-parameter models were investigated, and the ratio of bayesian evidences (e.g. Sivia, 1996) was used to select between the models. These models differed only in their dust properties and consisted of a type-2 quasar and a ULIRG. The extinction A_V, was allowed to vary, with a flat prior both for the ULIRG and the quasar model. The fourth free variable parameter is the redshift, z, which was given a flat

prior between $0 \leq z \leq 7$. No real quasars have been detected at $z \sim 7$, justifying this cutoff.

The stellar population was modelled by taking the SED of a $z = 0$ elliptical galaxy from Coleman et al. (1980). Although this might seem a poor choice at high redshift, many of the observed SEDs showed very strong 4000-Å breaks, which are not well fitted by young elliptical galaxies. SEDs showing smaller 4000-Å breaks were well fitted by the elliptical galaxy together with the blue component (see below). The elliptical was normalised to match the K-band luminosity of an L^* galaxy in the local K-band luminosity function of Cole et al. (2001). The luminosity of the galaxy relative to the local $L^*_{\rm K}$ was then allowed to vary with a prior flat in log-space, between $-1.3 \leq \log_{10}(L_{\rm gal}/L^*_{\rm K}) \leq 1.3$. This choice brackets the reasonable range of host galaxies for a powerful quasar accounting for passive evolution: from a very faint $0.05L^*_{\rm K}$ to a very bright $20L^*_{\rm K}$ galaxy. The choice of a prior flat in log-space means that the host galaxy is believed, a priori, to be as likely to lie between $0.1L^*_{\rm K}$ and $L^*_{\rm K}$ as between $L^*_{\rm K}$ and $10L^*_{\rm K}$. This is more realistic than a prior flat in real space, which would imply a quasar is as likely to be hosted by an $L^*_{\rm K}$ galaxy as by a $10L^*_{\rm K}$ one.

The blue component, between 912 Å and 5000 Å, has a physical motivation as well as serving a practical purpose. It can represent the scattered light from the obscured quasar, blue light from young stars or a UV-upturn brighter than that of the template elliptical galaxy used (and therefore a smaller 4000-Å break). The normalisation of the blue component is a free parameter given as a ratio of the luminosity to that of an $L^*_{\rm K}$ galaxy at 5000 Å, while the slope was set to $S_\nu \propto \nu^{-0.5}$, which is representative of both type-1 quasars and starforming galaxies. The luminosity of this blue component was allowed to vary independently of the galaxy, with a flat prior between $-2 \leq \log_{10}(L_{\rm blue}/L^*_{\rm K,5000Å}) \leq 2$, spanning the range between a blue component fainter than an $L^*_{\rm K}$ elliptical galaxy's UV-upturn, and as bright as the most powerful type-1 quasar.

The ULIRG dust component was modelled using the models of Siebenmorgen & Kruegel (2006) only allowing variation of one parameter, $A_{\rm V}$. For a given $A_{\rm V}$ and z, the bolometric luminosity of the ULIRG, $L_{\rm bol}$ was chosen to make the SED go as close as possible to the 24-μm data point. The values of $L_{\rm tot}$ are only restricted by the range available in the Siebenmorgen & Kruegel (2006) library: $10.1 \leq \log_{10}(L_{\rm tot}/L_\odot) \leq 12.7$ for our choice of parameters. Of the other parameters, the nuclear radius was fixed to 1 kpc, the ratio of luminosity of OB stars with hot spots to $L_{\rm tot}$ was

fixed to 0.6, and the hydrogen number density was fixed to 10^{10} m^{-3}. The models have a discreet set of values of the extinction (A_V = 2.2, 4.5, 6.7,9, 17.9, 35.9, 72 and 119), so the prior for the A_V consists of a set of δ-functions (with equal probability) at these values.

The mid-infrared SED for quasars was modelled using the Elvis et al. (1994) type-1 SED, and obscuring it with dust from the models of Pei (1992). For consistency with Siebenmorgen & Kruegel (2006), only Milky Way (MW)-type dust is used. This SED and dust model would allow us, in principle, to vary the values of A_V continuously, but to make the fitting procedure as fair as possible, we restricted the values of A_V to those present in the models of Siebenmorgen & Kruegel (2006) and assigned the same prior to them. Once again, for each object, the quasar bolometric luminosity L_{bol} was not allowed to vary freely, but was fixed for a given A_V and z by the observed flux density at 24 μm. There is, however, no upper limit set on L_{bol}.

For a given model, the likelihood of a given combination of parameters is

$$\mathrm{p(data|model\ A}, z, \mathrm{A_V}, \mathrm{L_{gal}}, \mathrm{L_{blue}}) = \frac{1}{(2\pi)^{n/2}\prod_i^n \sigma_i} e^{-\chi^2_A/2}, \tag{6.1}$$

where

$$\chi^2_A = \sum_i^n (\mathrm{model\ A}_i - \mathrm{data}_i)^2/\sigma_i^2, \tag{6.2}$$

model$_i$ is the predicted flux over a given waveband, given the parameters, data$_i$ is the observed flux at that band σ_i is the measurement error in that band and n is the number of bands. In the cases where σ_i was smaller than 10% of the flux density of the object, it was set to 10%. To treat non-detections at a particular band, we followed the following method: when the observed galaxy flux density and the model fell below the flux density limit (5 σ_{band}, where σ_{band} is the rms noise in that band), the band made no contribution to χ^2. When the model lay above the limit, the object was assigned a flux density equal to half of the flux density limit, and an error σ_i also equal to half of the flux density limit (so $\sigma_i = 2.5\sigma_{band}$). An undetected source would therefore only be $1\sigma_i$ away from zero flux density, and from the limit. This prescription is appropriate for our sources, selected to be faint and therefore close to the limits in most of the bands, to avoid penalising excessively nondetections in one band if the model SED does predict a detection.

To select between models, we follow Sivia (1996) in calculating the odds ratio (OR),

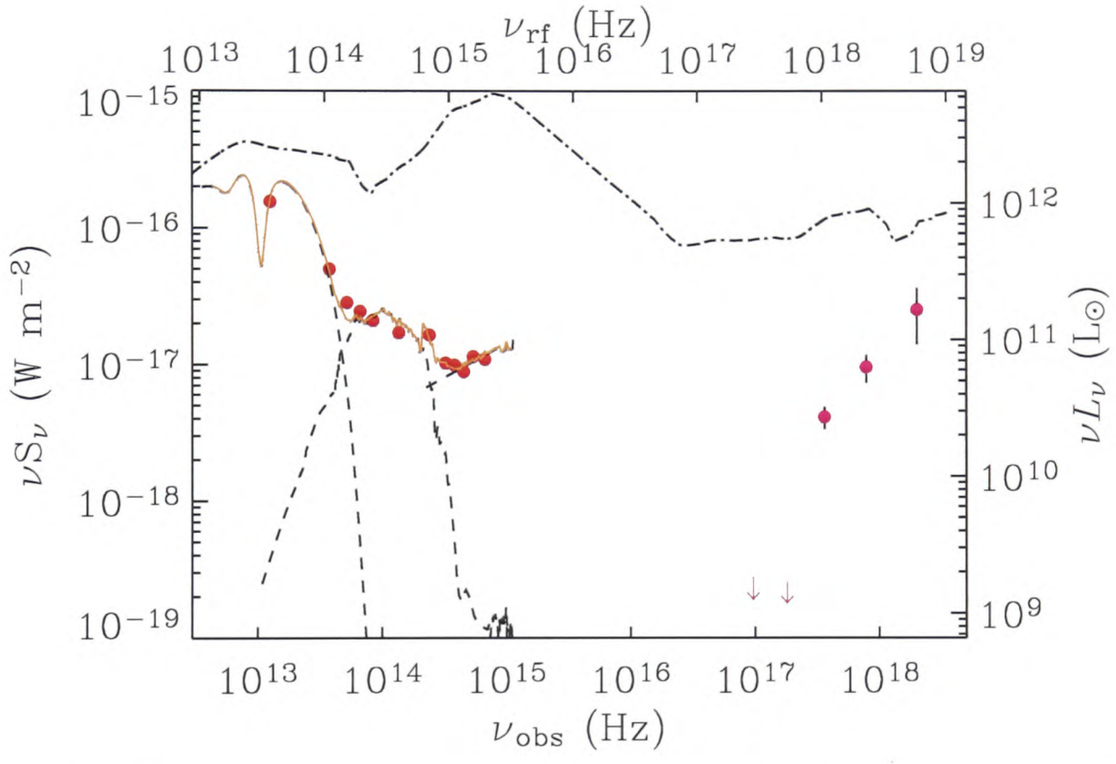

Figure 6.1: Best fit spectral energy distribution (SED) of ID401. The solid black lines show the quasar (with extinction), galaxy and blue templates normalised by the values (from Table 6.1) alongside the best fit to the data (red dots), the yellow line shows the combined best-fit templates. The purple dots and limits are the X-ray data in the 0.3-0.5 keV, 0.5-1 keV, 1-2 keV, 2-4.5 keV and 4.5-12 keV bands, from all three EPIC cameras. For comparison, the Elvis et al. (1994) type-1 SED has been overplotted (dash-dotted line), with the same values of $L_{\rm bol}$ and $z_{\rm phot}$ as ID401 (from Table 6.1), but without the Lyman forest. The top x-axis and right y-axis show the rest-frame frequencies and luminosities (in units of $L_\odot$) assuming the best-fit $z_{\rm phot} = 1.9$.

$$\mathrm{OR(A/B)} = \frac{\mathrm{p(d|A)\ p(A)}}{\mathrm{p(d|B)\ p(B)}}, \tag{6.3}$$

where, for brevity, we refer to model A as A, model B as B, and data as d. We assume that models A and B are equally likely *a priori*, $\mathrm{p}(A)/\mathrm{p}(B) = 1$, implying ignorance in the fraction of quasars c.f. starbursting galaxies. Thus the evidence for model y (where $\mathrm{y} \in \{A, B\}$) is proportional to p(d|y), which is simply the likelihood (from eq 1) integrated over the parameter space spanned by the priors, i.e.:

$$\mathrm{p(d|y)} = \int e^{-\chi^2_{\mathrm{y}}/2} \mathrm{p}(z)\mathrm{p}(A_{\mathrm{V}})\mathrm{p}(L_{\mathrm{gal}})\mathrm{p}(L_{\mathrm{blue}})\mathrm{d}z\mathrm{d}A_{\mathrm{V}}\mathrm{d}L_{\mathrm{gal}}\mathrm{d}L_{\mathrm{blue}}, \tag{6.4}$$

and $\mathrm{p}(x)$ is the normalised prior probability distribution of parameter x and the integral is over the entire prior space.

Within a given model, the set of parameters that will maximise the likelihood will be those with the lowest value of χ^2. Hence, the usual method of parameter estimation is minimising χ^2. When comparing between models, however, one cannot simply choose the model that will give the best χ^2, since this would inevitably favour the most complicated (and most fine-tuned) models. Common sense (and the famous *Ockham's razor*) tells us we should choose the simplest model that can explain the data. The odds ratio is able to do this, since it takes into account both the prior and the evidence for each model. In particular, the evidence will penalise exploring a larger parameter space and including extra parameters (through the larger normalisation term of the prior for each parameter: see Equation 6.2). Thus, for models with extra parameters (or exploring a larger parameter space) to be favoured over simpler models, the former must have an $e^{-\chi^2/2}$ term that is larger, by an amount that compensates for this penalisation (see Sivia, 1996).

In our particular case, the number of parameters and the range of the priors is the same for the two models being compared (the quasar and the ULIRG models), and we assume flat equal priors for the models. The odds ratio will therefore favour the model with the largest value of $\int e^{-\chi^2/2}\mathrm{d}V_{\mathrm{param}}$, where $\mathrm{d}V_{\mathrm{param}}$ is the entire parameter volume. This means that the model which has a low χ^2 over a larger parameter volume will be favoured over a model with a lower χ^2 for one combination of parameters, but a higher χ^2 for the rest of the parameter volume. In this way, we choose the model that best fits our data overall, and use this to judge whether each individual

Name	RA (J2000)	Dec	$z_{\rm phot}$	$\log_{10}[L_{\rm bol}$ /W]	$A_{\rm V}$	$\log_{10}[L_{\rm gal}$ $/L_{\rm k}^*]$	$\log_{10}[L_{\rm blue}$ $/L_{\rm k}^*]$	ln[OR(q/u)]	$\log_{10}$[p(d|q)/ $(S_{17})^{12}$/]	$S_{2-12{\rm keV}}$ / S_{17}
ID052	02 16 17.92	-05 07 18.56	1.90±0.05	42.11[1]	119	0.85	0.55	13.0	-10.0	<0.7
ID123	02 19 28.76	-05 09 08.81	1.75±0.05	41.12	72	0.65	0.20	5.2	-9.7	<2.9[2]
ID135	02 19 01.89	-05 11 14.22	4.15±0.05	41.14	2.2[3]	1.20	0.15	26.0	-9.4	<0.3
ID142	02 17 23.82	-04 35 13.72	4.05±0.05	41.29	6.7	1.25	0.45	10.0	-8.9	<0.4
ID147	02 19 10.31	-05 16 03.00	1.80±0.05	41.01	35.9	0.75	-0.05	28.6	-13.4	<0.3
ID200	02 18 15.71	-05 05 10.34	$1.75^{+0.05}_{-0.07}$	40.95	72	0.75	0.50	8.4	-9.1	<0.4
ID249	02 19 13.74	-04 56 04.27	1.75±0.05	40.89	35.9	0.50	0.00	25.2	-9.2	<0.6
ID342	02 17 05.35	-05 09 24.61	3.85±0.05	40.90	9.0	1.20	0.30	4.6	-15.25	<6.8[2]
ID345	02 16 29.56	-05 03 10.65	$2.00^{+0.08}_{-0.07}$	40.68	35.9[4]	1.00	0.10	10.4	-11.1	<0.6
ID347	02 18 09.64	-05 18 42.42	1.75±0.05	41.06	72	0.55	-0.30	5.8	-8.0	1.7±0.9[5]
ID386	02 17 25.11	-05 16 17.27	$1.90^{+0.05}_{-0.12}$	40.26	17.9	0.50	-0.75	6.2	-11.5	<0.1
ID401	02 16 23.02	-05 08 06.76	$1.90^{+0.05}_{-0.12}$	40.93	35.9	0.70	0.40	26.7	-8.9	3.4±1.3[5]

Table 6.1: Best-fit parameters and X-ray fluxes for the high-redshift type-2 quasars. The names are from the radio catalogue of Appendix A, and we define $S_{17} = 10^{-17}$ W m^{-2} for convenience. The errors in $z_{\rm phot}$ are estimated from the full-width half-maximum values from the marginalised probability distribution functions (PDFs) for $z_{\rm phot}$. For most objects, the PDF has at least one secondary peak, always adjacent to the primary one, with peak value between 0.5 and 0.05 of the primary peak. For the objects with $z_{\rm phot} \sim 4$, the value is likely to be an overestimate due to the lack of H-band data (i.e. they are likely to be at $z \sim 3$). The median value of $\log_{10}[L_{\rm gal}/L_{\rm k}^*]$, 0.75, corresponds to a $5.6L_{\rm k}^*$ (where $L_{\rm k}^*$ is the break in the local K-band luminosity function) galaxy at $z \sim 2$, which asuming passive evolution and using the models of Bruzual & Charlot (2003), would become a present-day $\sim L_{\rm k}^*$ galaxy. [1]This high value for $L_{\rm bol}$ is probably due to an overestimation of the $A_{\rm V}$. [2]The reason for these high values for the fluxes is that the noise is significantly higher ($\sim$100×) in the 4.5-12 keV band than in the 2-4.5 keV one. ID123 and ID342 are not detected in the X-ray data. [3]This value of $A_{\rm V}$ suggests a reddened type-1 quasar rather than a genuine type-2. [4]ID345 is a point source at K-band, which suggests the value of $A_{\rm V}$ is an overestimate. [5]ID347 and ID401 have safe X-ray detections. The best-fitting SEDs for quasar and ULIRG models for all 12 objects are shown in Figures 6.2 and 6.2

objects is more "quasar-like" or "ULIRG-like". Once a model has been chosen, the best-fitting parameters are chosen and shown in Table 6.1

To make sure that our X-ray analysis did not include any ULIRGs, only objects with OR(quasar/ulirg) $\geq$ 100 were considered as quasars. Note this criterion is very similar to the so-called Jeffreys' criterion (Jeffreys, 1961). In addition, to make sure the fits were acceptable, only sources with evidence p(data|quasar)/$(S_{17})^{12} \geq 10^{-17}$ were accepted, where $S_{17} = 10^{-17}$ W m^{-2} (S_{17} is defined to avoid numbers of order 10^{-204} or smaller). Our range of evidences in Table 1, $1.3 \times 10^{-9} \leq$p(data|quasar)/$(S_{17})^{12} \leq 5.5 \times 10^{-16}$, corresponds approximately to values of reduced $\chi^2 = 1.9 - 6.1$. Finally, only sources with $z_{\rm phot} \geq 1.70$ were kept, since Ly α is visible in optical spectroscopy, so the redshifts can be checked observationally. Preliminary spectroscopy of the sample suggests our values of $z_{\rm phot}$ are in good agreement with spectroscopic redshifts (Martínez-Sansigre et al. in prep.), except for the objects with $z_{\rm phot} \sim 4$, which are likely to lie at $z \sim 3$ with $z_{\rm phot}$ an overestimate due to the lack of H-band data.

Of the 38 candidates in the sample, 12 (32%) follow our above criteria and are considered our best candidates for high-redshift type-2 quasars. Their best-fit parameters are quoted in Table 6.1, and we proceed to analyse the X-ray properties of these sources. Visual inspection of the optical images showed several cases where the blue light was unresolved. This fits in well with scattered light from the quasar reaching us and justifies our choice of a "blue" component. Typically the best fitting normalisation for the blue component is ~5% of the normalisation of the quasar component, which agrees well with scattering fractions. The K-band images showed resolved sources in 11 cases, while ID345 is a point-source (suggesting a real $A_{\rm V} \lesssim 5$; a reddened type-1, see Chapter 2). The SED and $A_{\rm V}$ of ID135 (see Figures ?? and ??) also suggest a reddened quasar, rather than a genuine type-2.

6.3 X-ray properties of the type-2 quasars

The type-2 quasars were cross-matched with the X-ray catalogue of Ueda et al. (in prep.) with a flux limit of $\sim 3 \times 10^{-18}$ W m^{-2}, but only 2 out of 12 (17%) were detected: ID347 and ID401 (see Figure 6.4).

To obtain meaningful limits for the undetected sources, these had their counts measured

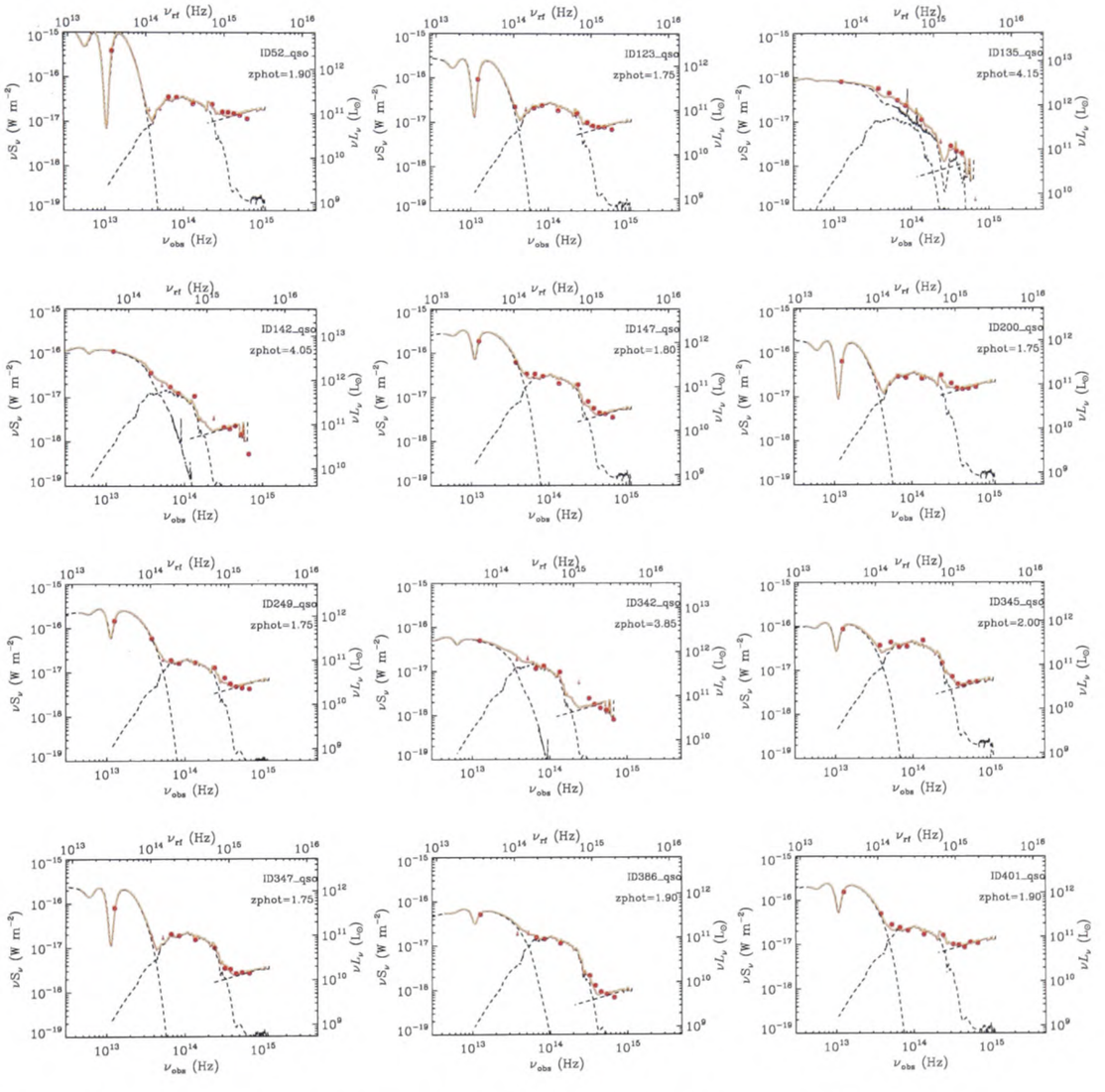

Figure 6.2: Best-fitting quasar templates for the 12 candidate type-2 quasars that meet the strict criteria. The red dots are the data points, the black dashed lines show the three components (obscured quasar, elliptical galaxy and blue component) and the combined best model is shown in yellow. The best-fit values are presented in Table 6.1.

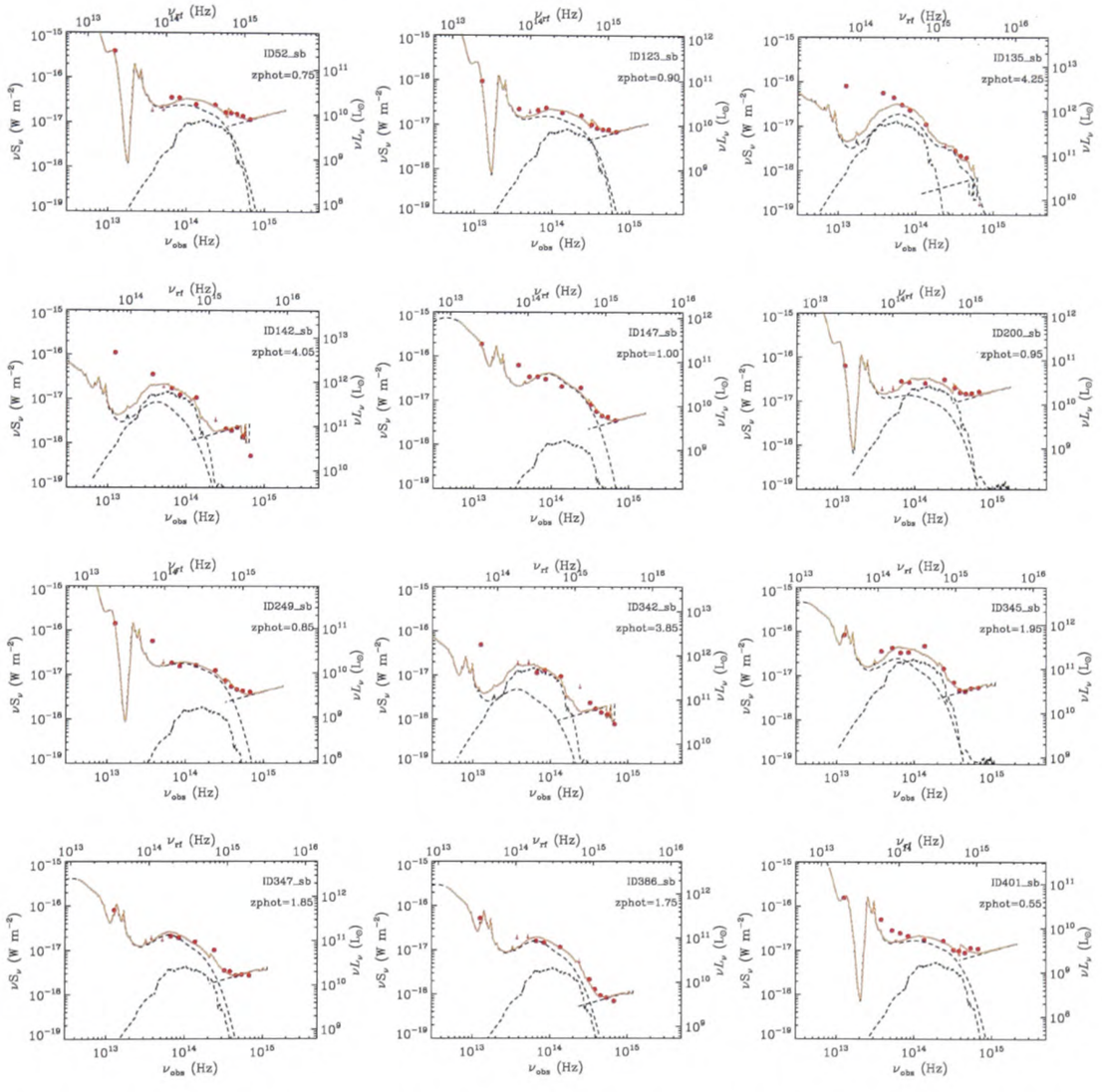

Figure 6.3: Best-fitting starburst (ULIRG) templates for the 12 candidate type-2 quasars. The same colour conventions are used as in Figure 6.2, except in this case the ULIRG models are used instead of the obscured quasar. In some cases, the best-fitting ULIRG templates can be rejected "by eye". However, many cases are not clear, showing the need for a rigorous model selection criterion.

directly from the X-ray image, using the XMM-Newton Science Analysis Software (SAS). The positions of the sources not detected in the XMM-Newton observations were added manually to the eboxdetect source lists of each observation. We then ran the SAS task emldetect keeping the positions of the sources fixed. Emldetect performs a maximum likelihood fit on the distribution of observed counts of the sources previously extracted by the task eboxdetect. The fit uses the five diferent energy bands (in keV: 0.2-0.5,0.5-1,1-2,2-4.5,4.5-12) and the three EPIC cameras (M1,M2,pn) simultaneously. This procedure allowed to fit the sources as multiple components with separate point-spread functions (PSFs), and sources with no evidence of any X-ray detection were still fitted.

This procedure allowed us to obtain fits to the counts for all sources in the 5 EPIC bands, and these were converted to fluxes assuming a photon index $\Gamma = 1.7$ and an obscuring column of $N_{\rm H} = 3 \times 10^{24}$ m^{-2}. Due to the large uncertainties in the count rates, the hardness ratios were deemed meaningless. All the 10 sources undetected in the Ueda et al. catalogue were found to have fitted values consistent with background noise, even in the harder bands. We therefore find that 83% of our sources classified as high-redshift type-2 quasars are undetected in the X-ray image, even down to a flux limit of $\sim 3 \times 10^{-18}$ W m^{-2}. Note from Figure 6.1 that even X-ray detections are well below the νL_ν $\sim$constant expectation from Elvis et al. (1994) and are therefore presumably highly obscured in the X-rays unless, of course, they are not actually AGN.

6.4 Discussion

We have found that 10 out of 12 of our sources classified as type-2 quasars are undetected in an X-ray image with an approximate flux limit $\sim 3 \times 10^{-18}$ W m^{-2} (in the 2-12 keV band). For the two detections, we use the photometric redshifts, the hardness ratios between the 0.3-2 and 2-12 keV bands, and the Monte-Carlo models of Wilman & Fabian (1999) to estimate the absorbing columns. The estimates for ID347 and ID401 are $\log_{10}(N_{\rm H}/{\rm m}^2) = 28.50$ and 28.75 respectively, and derived gas to dust ratios of $\frac{N_{\rm H}}{A_{\rm V}} = 4 \times 10^{26}$ and 2×10^{27} m^{-2} (similar to those found by Watanabe et al., 2004, and much larger than the Milky-Way value, often used as "standard"). For the undetected objects, it is not possible to estimate values of $N_{\rm H}$ from the hardness ratios.

Instead, to get a handle of the possible values of $N_{\rm H}$, in Figure 6.5 we show fiducial tracks

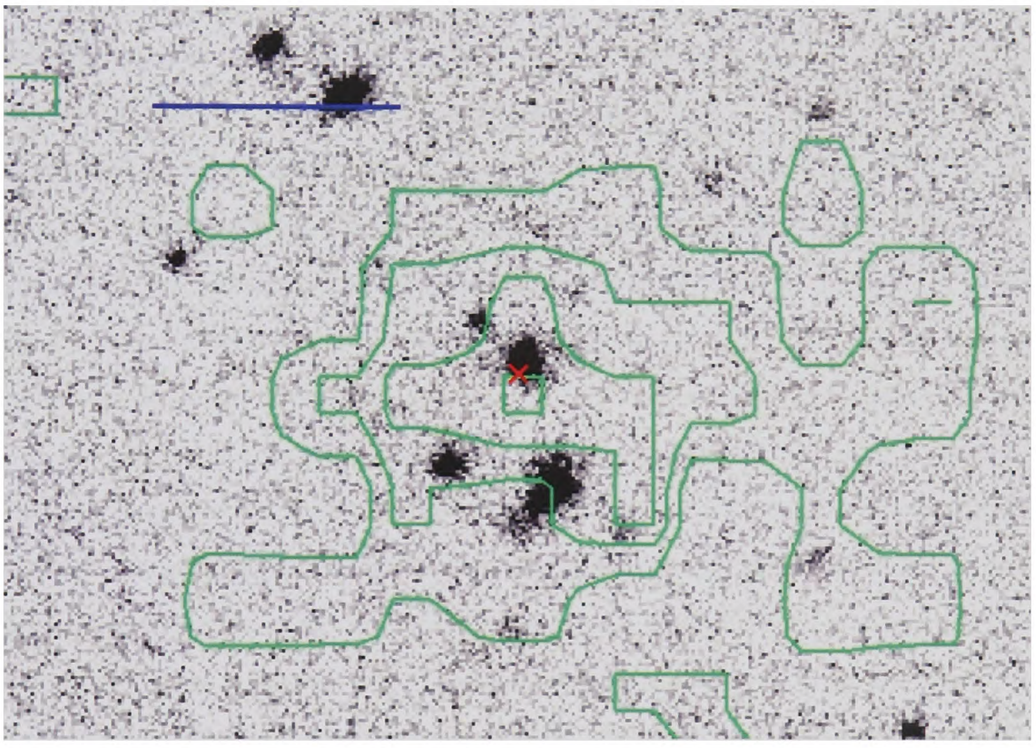

Figure 6.4: K-band image of ID401, with X-ray contours overlayed (green; all three EPIC cameras, in the energy range 0.3-12 keV). The green contours represent 4, 8, 12 and 16 photons per pixel, the X-ray pixels are smoothed to 6 arcsec, and the PSF of the EPIC cameras varies between 4 and 6 arcsec (on-axis) to ∼12 arcsec (off-axis). Given these PSFs, the X-ray source is consistent with a point source. The K-band image has a limiting magnitude of 23.5 (AB), 5-σ for a point-source, and has been taken with seeing better than 0.8 arcsec. The blue line, placed to show the scale, is 10 arcsec long. The red cross marks the radio position of the type-2 quasar. This is one of only two X-ray detections in our sample, and is a Compton-thick quasar.

for a model quasar. The model quasar has $M_{\rm B} = -25.7$, which from the Elvis et al. (1994) SED corresponds to $L_{\rm bol} \sim 7 \times 10^{39}$ W and is therefore well matched to our candidates (see Figure caption for details). ID347 and ID401 have values of $S_{24\mu{\rm m}}$ and $S_{2-12{\rm keV}}$ and estimates for $N_{\rm H}$ (derived only from hardness ratios) all in reasonable agreement with the tracks. Another two objects (ID123 and ID342) have limits for $S_{2-12{\rm keV}}$ also consistent with the tracks, suggesting $\log_{10}(N_{\rm H}/{\rm m}^2) \gtrsim 28.25$.

Eight other quasar candidates at $1.75 \leq z_{\rm phot} \leq 4.15$ have similar values of $S_{24\mu{\rm m}}$, $L_{\rm bol}$ to ID347 and ID401, yet significantly fainter limits for $S_{2-12{\rm keV}}$. If the values of $L_{\rm bol}$ have been overestimated, or the values of $z_{\rm phot}$ have been underestimated, then $N_{\rm H}$ could be slightly overestimated, but the derived values are those expected from our selection function: they do not seem gross overestimates. The most likely source of error is the choice of Γ and $N_{\rm H}$ used to derive the fluxes (Section 4), which can underestimate $S_{2-12{\rm keV}}$. Still, the lack of detections and comparison with the fiducial tracks suggests very high absorbing columns and gas-to-dust ratios. If the sources are indeed quasars, the X-ray properties of this sample seem to require $N_{\rm H} \geq 10^{28}$ m^{-2}, so that effectively all objects, even the two detections, are Compton-thick. The caveats are the same as those discussed at the end of Chapter 2, and in addition we do not have spectroscopic confirmation of all the objects being type-2 quasars. Even if they were, the Elvis et al. (1994) SED is only a median: objects with an intrinsically lower X-ray to mid-infrared ratio will require a lower value of $N_{\rm H}$ to become invisible. However, our result still strongly hints at a large population of heavily X-ray absorbed quasars.

We have therefore found that selection of type-2 quasars in the mid-infrared unveils a population of Compton-thick objects, a large fraction of which is undetectable in X-ray surveys due to the lack of surveys covering large areas at the necessary depth. In the infrared, these objects are often consistent with stellar light dominating the emission at 3.6 μm and shorter wavelengths, meaning they were impossible to find until Spitzer was launched (Werner et al., 2004).

Following Chapter 4, we model the expected number of type-1 quasars following our 24-μm and radio flux density criteria, at $z \geq 1.70$, and in 0.8 deg^2. We predict 2±0.8 type-1 quasars following these criteria, and since Poisson errors dominate the number of type-2 quasars, we can easily estimate the ratio of type-2s to type-1s at $z \geq 1.70$ from this study as $4.5^{+5.5}_{-2.4}$. This is obviously plagued by small-number statistics, so we simply consider this estimate consistent within the error

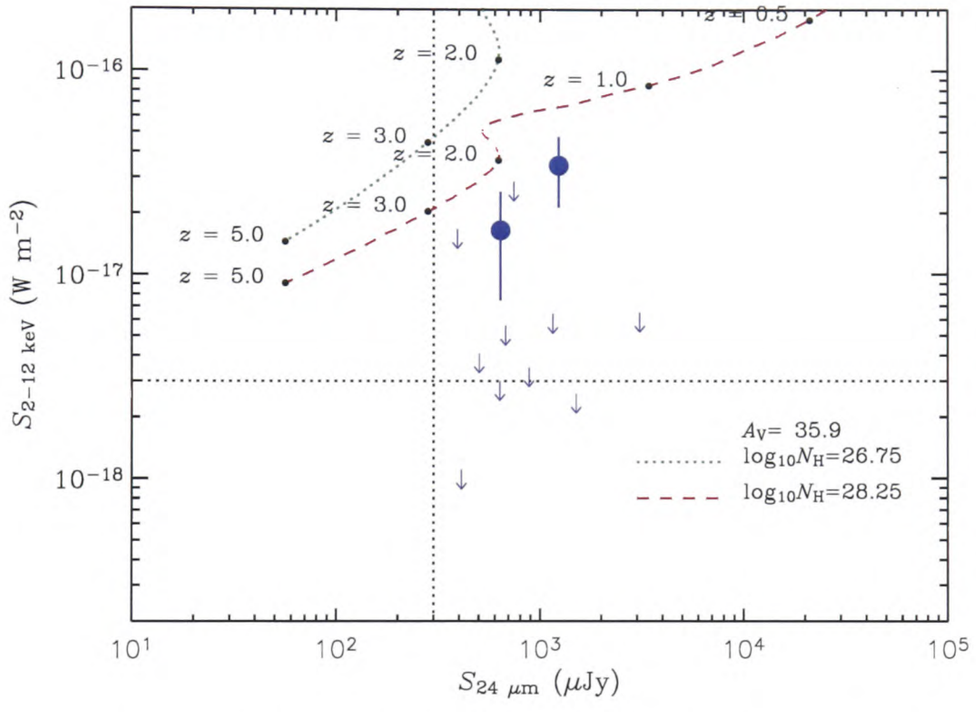

Figure 6.5: Hard X-ray flux ($S_{2-12\mathrm{keV}}$) versus 24-μm flux density ($S_{24\ \mu\mathrm{m}}$) as a function of redshift for a $M_B = -25.7$ model quasar obscured with dust from the models of Pei (1992), assuming two gas-to-dust ratios ($N_H = 1.9 \times 10^{25}$ and 5×10^{26} m$^{-2} \times A_V$) and using the absorbed X-ray spectra of Wilman & Fabian (1999; see Chapter 2 for more details). The 12 type-2 quasars in our sample are overplotted in blue. The vertical dotted line is the 300 μJy flux density limit imposed on our sample, the horizontal dotted line is the approximate flux limit of the X-ray map, $\sim 3 \times 10^{-18}$ W m^{-2}. Both quasar tracks have $A_V = 35.9$ (the median of our sample) and have black dots marking redshifts. The green track has $N_H = 6 \times 10^{26}$ m^{-2}, and is therefore a Compton-thin obscured (type-2) quasar, while the red track has $N_H = 2 \times 10^{28}$ m^{-2} and is therefore so obscured it is known as "Compton-thick". Considering our type-2 quasars are well matched in luminosity to the fiducial tracks, and they are selected to be at $z_{\mathrm{phot}} \geq 1.70$, if the sources are indeed quasars then the lack of X-ray detections can only be explained by extreme absorbing columns ($N_H \gtrsim 10^{28}$ m^{-2}).

bars with our previous result. What does seem significant is that, since all the type-2s presented here are Compton-thick, at high redshift the number of Compton-thick quasars is probably larger than the number of type-1 quasars.

With such high values of $N_{\rm H}$, due to their rare spatial density and their high-redshifts, these objects are unlikely to make a significant contribution to the hard X-ray background (energies ≥ 1 keV). However, conclusions on the cosmological evolution and relative fractions of obscured and unobscured AGN (e.g. Ueda et al., 2003; Barger et al., 2005), estimates of the radiative efficency of accreting SMBHs (e.g. Marconi et al., 2004), and searches for AGN buried in dusty objects (e.g. Alexander et al., 2005b), have generally been based on X-ray observations and are therefore likely to have underestimated the number of accreting SMBHs. Mid-infrared selection of quasars seems more successful at finding heavily obscured objects, although instead the difficulty lies in filtering out the starbursts from the quasars.

Chapter 7

Concluding Perspective

We began this thesis searching for high-redshift obscured (type-2) quasars, to determine an efficient way of finding these objects, to determine their relative numbers with respect to the unobscured (type-1) quasars, and to determine why X-ray surveys have so far been unable to find them in significant numbers.

In Chapter 2, we have discussed the relative "merits" of X-ray and mid-infrared selection of high-redshift type-2 quasars. We have found that if quasars are obscured by dust with gas-to-dust ratios similar to those of the Milky Way, then X-ray selection is expected to fare better. However, if the quasars have gas-to-dust ratios similar to those of the Small Magellanic Clouds, or even higher, then mid-infrared selection should do better. This is because heavily obscured quasars ($A_V \gtrsim 20$) will have extreme X-ray obscuring columns ($N_H \gtrsim 10^{28}$ m^{-2}, or "Compton-thick") and will only be detectable by surveys sensitive to fluxes $\gtrsim 10^{-18}$ W m^{-2}. The flux density at 24 μm is a reasonable reflection of the bolometric luminosity at $2 \lesssim z \lesssim 4$, while at $z \sim 1.5$ it is highly biased against type-2 quasars. This means that the combination of area and selection function for 24-μm surveys is better at finding $z \gtrsim 2$ quasars.

Deep hard-X-ray surveys with the combination of area and sensitivity to look for heavily absorbed quasars are just becoming available (e.g. the SXDF, see Appendix A for the radio catalogue in that field). These surveys have a flat-selection function for Compton-thick quasars, which, combined with the volume covered by the survey at each redshift, should yield a large number of objects at $1 \lesssim z \lesssim 2$. This would then be complimentary to 24-μm selection, unless there exists a population of objects with even higher values of N_H, which might only be detectable

in mid-infrared surveys.

Encouraged by this analysis, we have devised a mid-infrared and radio selection method to search for these high-redshift type-2 quasars. The exact criteria we have used are:

1. $S_{24\ \mu m} > 300\ \mu$Jy
2. $S_{3.6\ \mu m} \leq 45\ \mu$Jy
3. 350 μJy $\leq S_{1.4\ GHz} \leq 2$ mJy

The two infrared criteria are designed to look for sources with emission from warm ($\sim 300 - 400$ K) dust, which reprocesses the obscured optical and ultraviolet light. They are designed to reject sources with a flat spectral energy distribution (SED) in νS_ν, characteristic of type-1 quasars or slightly reddened ($A_V \sim$ 1-5) quasars. The 3.6 μm criterion serves as an additional crude photometric cut, allowing us to select type-2 quasars at $z \gtrsim 1.4$.

However, since ultra-luminous infrared galaxies (ULIRGs) are likely contaminants, we include a radio criterion to reject sources which are not powered by AGN. This drastically reduces the number of type-2 candidates in our sample, but should keep the fraction of contaminants to a minimum. We do note that our criteria have been designed using typical quasar SEDs, so that for quasars whose SEDs are intrinsically different, the selection function might not be as well-behaved.

Spectroscopic observations of our candidates in the Spitzer First Look Survey (FLS), described in Chapter 3, confirm at least about half of our sample as high-redshift AGN. In the frame work of the unified scheme, the mid-infrared properties are therefore consistent with genuine type-2 quasars. However, independent confirmation, in the form of C IV, is only present in 6 objects. Ly α is present in all but one object, and C IV and He II are sometimes seen. One source, AMS18 at $z = 1.017$ has no high-ionization lines visible in the optical spectra, and from the radio properties derived in Chapter 5, is likely to be a contaminant. Analysing the optical spectra and the radio properties, we find the sources are consistent with high-redshift quasars obscured by the torus (if the unified scheme is correct), albeit the radio-intermediate population, and we label these as "torus-obscured". Amongst the radio-loud population, recent work has confirmed a large fraction of radio-galaxies as having strong mid-infrared emission, consistent with hosting type-2 quasars. Thus, applying our criteria, but with higher radio-flux cuts, is expected to select similar radio-loud type-2 quasars (at high-redshift).

The sources with blank optical spectra have properties similar to those which show narrow-emission lines. ULIRG contaminants would be likely to show at least faint continuum and probably [O II] in their spectra, as is seen in AMS18. We find no evidence for a large contaminant fraction, and suspect that the blank optical spectra are due to obscuring dust on scales larger than the narrow-emission line region. These type-2 quasars, which we label as "host-obscured", are likely to be at similar redshifts to the "torus-obscured", and in two cases (AMS06 and AMS19) this is confirmed by mid-infrared spectroscopy.

Confident that contamination is not a major problem in our sample, we evaluate the quasar fraction, q, by using a bayesian method. We compute a probability distribution for q by applying our selection criteria to a type-1 luminosity function, with an optical-to-radio correlation. We conclude that the quasar fraction has a model value of $q \sim 0.5$ when considering only as type-2 quasars the sources with narrow-emission lines, and a modal value of $q \sim 0.3$ when considering all type-2 quasars.

This result is consistent both with the quasar fraction for radio-loud objects, as well as the fraction derived from the "receding-torus" models. In radio-loud objects, the radio jets are likely to clear dust in the surroundings, so that the number of host-obscured sources should be small, while the receding-torus models only consider obscuration by the torus. These should therefore be compared to our value of q from the narrow-line objects, which are obscured by the torus. However, the total quasar fraction requires taking into account other forms of obscuration, and is therefore ~ 0.3. From our modelling and our two probability distributions we can conclude that around the peak in (type-1) quasar activity 50-80% of the quasars were obscured, so that most of the accretion onto supermassive black holes is obscured.

If our results for the quasar fraction are correct and host-obscured quasars exist, then the obscuration in this subset of type-2 quasars should be independent of the orientation of the torus. Since our sample comprises radio-intermediate quasars, with at least some radio jet activity, one might expect a fraction of the host-obscured quasars to have their radio jets aligned close to our line-of-sight, and to exhibit flat radio spectra, just like some broad-line type-1 quasars do.

In addition to testing this hypothesis, radio observations can also give additional information about the nature of the jets, and the ages of the sources, so in Chapter 5 we use data at three radio frequencies to obtain spectral indices and estimate the rest-frame radio luminosities of our sources.

We find the majority of sources to have steep spectra and radio luminosities $L_{1.4} \sim 10^{24}$ W Hz^{-1} sr^{-1}. We find that these sources have radio properties (radio power and spectral index) consistent with those of low-redshift FRI sources once we take into account the effects of an increased CMB energy density. We also find a few type-2 quasars have spectra that peak at gigahertz frequencies, characteristic of young radio jets.

In addition, several of our sources have flat-spectra, as expected for type-1 quasars, but inconsistent with the hypothesis of torus-obscuration. Only one of these flat-spectrum sources shows emission lines in the optical, AMS18, but all of the lines could be due to a starburst, and not a quasar. The low radio luminosity of this object suggests powering by massive-star-formation, and not radio-jets. There is therefore strong evidence for this to be a contaminant in our sample

The other flat-spectrum sources show no narrow-emission lines, although we have a spectroscopic redshift, $z = 2.25$ from Spitzer, for one of these sources (AMS19). These sources are consistent with the hypothesis of host-obscuration, and their radio spectral indices are difficult to reconcile with torus-obscuration. We have therefore found some additional evidence for these host-obscured quasars.

The quasar fraction, accounting for the two types of type-2, is therefore probably close to $q = 0.3$. The type-2 quasars considered in this thesis are at high redshift, and their space-density is low, so that they are unlikely to make a significant contribution to the hard-X-ray background. It is still important, though, to understand why they are so rarely seen in the hard-X-ray surveys, and to test the possibility that some of them have extreme obscuring columns.

For this purpose, we have searched for a similar sample in the Subaru XMM-Newton Deep Field (SXDF), where there are very deep X-ray data as well as mid-infrared and radio data. In Chapter 6, we use identical mid-infrared criteria on a sample of radio sources down to $S_{1.4\mathrm{GHz}} = 100$ μJy, to pre-select 38 candidate type-2 quasars. Lowering the radio criterion is likely to increase the contaminant fraction, so care must be taken to exclude ULIRG contaminants from the X-ray analysis, to avoid overestimating the number of Compton-thick sources.

Due to a lack of spectroscopic data yet a wealth of available photometry, we use a bayesian SED-fitting method. This relies on maximising the posterior probabilities to find the best-fit parameters for a model (a set of templates). In addition, though, we make use of the evidence to select the most appropriate model, and apply strict criteria to remove any source that does not

have a strong evidence of being a type-2 quasar.

We are left with 12 candidate high-redshift type-2 quasars in the field (with $z_{\rm phot} \geq 1.70$), of which only 2 are detected in the X-ray catalogue. The remaining 10 sources are consistent with X-ray non-detections: this could be due to the sources being intrinsically faint, very distant, or due to extreme absorbing columns. The number of very high-redshift quasars ($z \sim 4$) is expected to be small in this small area. The results of the fitting routine suggest our sources are powerful quasars, and are mostly at redshifts ($z \sim 2$) where they should be detectable in the X-ray data, unless they have extreme values of $N_{\rm H}$. These are only candidates, and the intrinsic SEDs might differ from those we have assumed, so the exact value of $N_{\rm H}$ cannot be inferred, and until we have spectroscopic observations, these 12 objects will remain candidates.

We have therefore found strong evidence for Compton-thick quasars at high-redshift, although spectroscopy will be required to confirm this result. The existence of such Compton-thick quasars means that mid-infrared selection is able to find quasars undetectable in current X-ray surveys, although it has the disadvantage of including contaminants, in the form of ULIRGs, in significant numbers. A solution is keeping a high radio flux density criterion, but this leads to small number statistics. Interestingly, we find the number of Compton-thick quasars to be larger than the expected number of unobscured, type-1 quasars, with important consequences for any conclusions about supermassive black hole (SMBH) demographics derived from X-ray data alone.

7.1 Future Work

This thesis has been successful in finding a population of sources, type-2 quasars, which were previously limited to serendipitous discoveries. However, the work to understand these objects has only just begun. Optical spectroscopy is typically successful in finding a redshift in only half of the sources, so photometric redshifts are required to complete the samples. However, these objects are new and poorly understood, so a thorough program of complementary spectroscopy is desirable and could make use, for example, of the mid-infrared lines (such as the silicate and PAH features). This is required to discriminate between whether the "blank" sources really are at the same redshifts as the narrow-emission line objects and have obscured narrow-lines, or whether they are simply at redshifts were no optical narrow lines are detectable.

For sources which show no emission lines, and are Compton-thick, evidence for AGN activity is limited to arguments of bolometric luminosity, and mid-infrared spectral shape. These are both dangerous arguments: the sub-millimetre selected population is believed to be dominated by sources with bolometric luminosities comparable to those of quasars. At such bright luminosities, the mid-infrared continuum can dominate over line-emission, so the PAH emission lines, tell-tale signatures of star-forming activity, are not necessarily obvious.

It is therefore crucial to carry on with multi-wavelength studies of these objects, to be able to distinguish objectively between obscured starbursts and obscured quasars. There is, of course, the fascinating possibility that the two classes are closely related. In that case, obscured sources could represent a particularly important phase of quasar and galaxy evolution.

From correlations between galaxy properties and black-hole properties (e.g. Magorrian et al., 1998) and from semi-analytical modelling of the galaxy luminosity function (e.g. Benson et al., 2003), it is currently believed that quasar negative feedback truncates star-formation in the host galaxy by ejecting the gas fuelling the star-formation (e.g. Silk & Rees, 1998). Before this truncation occurs, the quasar is expected to be obscured by the surrounding starburst (e.g. Fabian, 1999). Some of the objects we have labelled as "host-obscured" might well be representative of this phase in galaxy evolution, and studies of obscured quasars might therefore prove crucial in understanding how the quasar terminates star-formation and shapes the luminosity function. This is an extremely exciting prospect, and studies ranging from radio frequencies to X-rays, combining continuum and line properties, will hopefully be able to shed more light on this currently obscured area.

Bibliography

Afonso, J., Mobasher, B., Koekemoer, A., Norris, R. P., & Cram, L. 2006, AJ, 131, 1216

Alexander, D. M., et al. 2003, AJ, 126, 539

Alexander, D. M., Chartas, G., Bauer, F. E., Brandt, W. N., Simpson, C., & Vignali, C. 2005a, MNRAS, 357, L16

Alexander, D. M., Smail, I., Bauer, F. E., Chapman, S. C., Blain, A. W., Brandt, W. N., & Ivison, R. J. 2005b, Nat, 434, 738

Almaini, O., Lawrence, A., & Boyle, B. J. 1999, MNRAS, 305, L59

Almaini, O., et al. 2003, MNRAS, 338, 303

Andreani, P., Cimatti, A., Loinard, L., & Röttgering, H. 2000, A&A, 354, L1

Antonucci, R. 1993, ARA&A, 31, 473

Archibald, E. N., Dunlop, J. S., Jimenez, R., Friaça, A. C. S., McLure, R. J., & Hughes, D. H. 2002, MNRAS, 336, 353

Baker, J. C., Hunstead, R. W., Athreya, R. M., Barthel, P. D., de Silva, E., Lehnert, M. D., & Saunders, R. D. E. 2002, ApJ, 568, 592

Barger, A. J., Cowie, L. L., Mushotzky, R. F., Yang, Y., Wang, W.-H., Steffen, A. T., & Capak, P. 2005, AJ, 129, 578

Benn, C. R., Rowan-Robinson, M., McMahon, R. G., Broadhurst, T. J., & Lawrence, A. 1993, MNRAS, 263, 98

Benson, A. J., Bower, R. G., Frenk, C. S., Lacey, C. G., Baugh, C. M., & Cole, S. ApJ, 599, 38

Bertin, E. & Arnouts, S. 1996, A&AS, 117, 393

Best, P. N., Röttgering, H. J. A., & Longair, M. S. 2000, MNRAS, 311, 23

Blandford, R. D. & Znajek, R. L. 1977, MNRAS, 179, 433

Blundell, K. M. & Rawlings, S. 2001, ApJL, 562, L5

Bohlin, R. C., Savage, B. D., & Drake, J. F. 1978, ApJ, 224, 132

Bondi, M., et al. 2003, A&A, 403, 857

Bouchet, P., Lequeux, J., Maurice, E., Prevot, L., & Prevot-Burnichon, M. L. 1985, A&A, 149, 330

Bower, R. G., Benson, A. J., Malbon, R., Helly, J. C., Frenk, C. S., Baugh, C. M., Cole, S., & Lacey, C. G. 2006, MNRAS, 659

Brandl, B. R., et al. 2004, ApJS, 154, 188

Brandt, W. N. & Hasinger, G. 2005, ARA&A, 43, 827

Brinkmann, W., Laurent-Muehleisen, S. A., Voges, W., Siebert, J., Becker, R. H., Brotherton, M. S., White, R. L., & Gregg, M. D. 2000, A&A, 356, 445

Broadhurst, T. & Lehar, J. 1995, ApJL, 450, L41+

Bruzual, G. & Charlot, S. 2003, MNRAS, 344, 1000

Chapman, S. C., Blain, A. W., Smail, I., & Ivison, R. J. 2005, ApJ, 622, 772

Chiaberge, M., Capetti, A., & Celotti, A. 1999, A&A, 349, 77

Chiang, J. & Murray, N. 1996, ApJ, 466, 704

Ciliegi, P., et al. 1999, MNRAS, 302, 222

Ciliegi, P., et al. 2005, A&A, 441, 879

Cirasuolo, M., Celotti, A., Magliocchetti, M., & Danese, L. 2003, MNRAS, 346, 447

Clewley, L. & Jarvis, M. J. 2004, MNRAS, 352, 909

Cohen, J. G., Hogg, D. W., Blandford, R., Cowie, L. L., Hu, E., Songaila, A., Shopbell, P., & Richberg, K. 2000, ApJ, 538, 29

Cole, S. et al. 2001, MNRAS, 326, 255

Coleman, G. D., Wu, C.-C., & Weedman, D. W. 1980, ApJS, 43, 393

Comastri, A., Setti, G., Zamorani, G., & Hasinger, G. 1995, A&A, 296, 1

Condon, J. J. 1984, ApJ, 284, 44

—. 1992, ARA&A, 30, 575

—. 1997, PASP, 109, 166

Condon, J. J., Cotton, W. D., Greisen, E. W., Yin, Q. F., Perley, R. A., Taylor, G. B., & Broderick, J. J. 1998, AJ, 115, 1693

Condon, J. J., Cotton, W. D., Yin, Q. F., Shupe, D. L., Storrie-Lombardi, L. J., Helou, G., Soifer, B. T., & Werner, M. W. 2003, AJ, 125, 2411

Connolly, A. J., Szalay, A. S., Dickinson, M., Subbarao, M. U., & Brunner, R. J. 1997, ApJL, 486, L11+

Croom, S. M., Smith, R. J., Boyle, B. J., Shanks, T., Miller, L., Outram, P. J., & Loaring, N. S. 2004, MNRAS, 349, 1397

Croton, D. J., et al. 2006, MNRAS, 365, 11

Czerny, B., Li, J., Loska, Z., & Szczerba, R. 2004, MNRAS, 348, L54

de Ruiter, H. R., Arp, H. C., & Willis, A. G. 1977, A&AS, 28, 211

Donley, J. L., Rieke, G. H., Rigby, J. R., & Pérez-González, P. G. 2005, ApJ, 634, 169

Downes, D., et al. 1999, A&A, 347, 809

Dunlop, J. S. & Peacock, J. A. 1990, MNRAS, 247, 19

Eddington, A. S. 1913, MNRAS, 73, 359

Elvis, M., et al. 1994, ApJS, 95, 1

Fabian, A. C. 1999, MNRAS, 308, L39

Fadda, D., Jannuzi, B. T., Ford, A., & Storrie-Lombardi, L. J. 2004, AJ, 128, 1

Fadda, D., et al. 2006, AJ, 131, 2859

Falcke, H., Sherwood, W., & Patnaik, A. R. 1996, ApJ, 471, 106

Fanaroff, B. L. & Riley, J. M. 1974, MNRAS, 167, 31P

Ferrarese, L. & Merritt, D. 2000, ApJL, 539, L9

Fioc, M. & Rocca-Volmerange, B. 1997, A&A, 326, 950

Gaskell, C. M., Goosmann, R. W., Antonucci, R. R. J., & Whysong, D. H. 2004, ApJ, 616, 147

Gebhardt, K., et al. 2000, ApJL, 543, L5

Gilli, R., Salvati, M., & Hasinger, G. 2001, A&A, 366, 407

Granato, G. L. & Danese, L. 1994, MNRAS, 268, 235

Granato, G. L., Silva, L., Monaco, P., Panuzzo, P., Salucci, P., De Zotti, G., & Danese, L. 2001, MNRAS, 324, 757

Greve, T. R., et al. 2005, MNRAS, 359, 1165

Grimes, J. A., Rawlings, S., & Willott, C. J. 2004, MNRAS, 349, 503

Gruppioni, C., Mignoli, M., & Zamorani, G. 1999, MNRAS, 304, 199

Gruppioni, C., Zamorani, G., de Ruiter, H. R., Parma, P., Mignoli, M., & Lari, C. 1997, MNRAS, 286, 470

Haas, M., Chini, R., Müller, S. A. H., Bertoldi, F., & Albrecht, M. 2006, A&A, 445, 115

Hainline, L. J., Blain, A. W., Greve, T. R., Chapman, S. C., & Smail, I. 2006

Hardcastle, M. J. & Worrall, D. M. 2000, MNRAS, 314, 359

Hopkins, A. M., Afonso, J., Chan, B., Cram, L. E., Georgakakis, A., & Mobasher, B. 2003, AJ, 125, 465

Hopkins, P. F., et al. 2004, AJ, 128, 1112

Jarvis, M. J. & Rawlings, S. 2004, New Astronomy Review, 48, 1173

Jarvis, M. J., Rawlings, S., Eales, S., Blundell, K. M., Bunker, A. J., Croft, S., McLure, R. J., & Willott, C. J. 2001a, MNRAS, 326, 1585

Jarvis, M. J., et al. 2001b, MNRAS, 326, 1563

Jarvis, M. J., van Breukelen, C., & Wilman, R. J. 2005, MNRAS, 358, L11

Jeffreys, H. 1961, Theory of Probability (Oxford University Press)

Kardashev, N. S. 1962, Soviet Astronomy, 6, 317

Katgert, P., Oort, M. J. A., & Windhorst, R. A. 1988, A&A, 195, 21

Kellermann, K. I., Sramek, R., Schmidt, M., Shaffer, D. B., & Green, R. 1989, AJ, 98, 1195

Krolik, J. H. 1999, Active galactic nuclei : from the central black hole to the galactic environment (Princeton University Press)

Kroupa, P. 2001, MNRAS, 322, 231

Kukula, M. J., Dunlop, J. S., McLure, R. J., Miller, L., Percival, W. J., Baum, S. A., & O'Dea, C. P. 2001, MNRAS, 326, 1533

Lacy, M., et al. 2005a, MmSAI, 76, 154

Lacy, M. et al. 2004, ApJS, 154, 166

—. 2005b, ApJS, 161, 41

Laing, R. A. & Peacock, J. A. 1980, MNRAS, 190, 903

Lawrence, A. 1991, MNRAS, 252, 586

Lawrence, A. et al. 2006 (astro-ph/0604426)

Leahy, J. P. 1991, Interpretation of large scale extragalactic jets (Beams and Jets in Astrophysics), 100–+

Leipski, C., et al. 2005, A&A, 440, L5

Lonsdale, C. J. et al. 2003, PASP, 115, 897

Madau, P., Ghisellini, G., & Fabian, A. C. 1994, MNRAS, 270, L17+

Magorrian, J., et al. 1998, AJ, 115, 2285

Mainieri, V., et al. 2005, MNRAS, 356, 1571

Maiolino, R., Marconi, A., Salvati, M., Risaliti, G., Severgnini, P., Oliva, E., La Franca, F., & Vanzi, L. 2001, A&A, 365, 28

Marconi, A., Risaliti, G., Gilli, R., Hunt, L. K., Maiolino, R., & Salvati, M. 2004, MNRAS, 351, 169

Marleau, F. R. et al. 2004, ApJS, 154, 66

Martínez-Sansigre, A., Rawlings, S., Lacy, M., Fadda, D., Marleau, F. R., Simpson, C., Willott, C. J., & Jarvis, M. J. 2005, Nat, 436, 666

Martínez-Sansigre, A., Rawlings, S., Lacy, M., Fadda, D., Jarvis, M. J., Marleau, F. R., Simpson, C., & Willott, C. J. 2006a, MNRAS, 370, 1479

Martínez-Sansigre A., Rawlings S., Garn T., Green D. A., Alexander P., Klöckner H.-R., Riley J. M., 2006b, MNRAS, 373L, 80

Martínez-Sansigre, A., et al. 2006c, MNRAS, submitted (astro-ph/0611739)

McCarthy, P. J., Spinrad, H., Djorgovski, S. Strauss, M. A., van Breugel, W.& Liebert, J., 1987, ApJ, 319L, 39

McCarthy, P. J. 1993, ARA&A, 31, 639

Miller, L., Peacock, J. A., & Mead, A. R. G. 1990, MNRAS, 244, 207

Miller, P., Rawlings, S., & Saunders, R. 1993, MNRAS, 263, 425

Morganti, R., Garrett, M. A., Chapman, S., Baan, W., Helou, G., & Soifer, T. 2004, A&A, 424, 371

Morganti, R., Tadhunter, C. N., & Oosterloo, T. A. 2005, A&A, 444, L9

Mortier, A. M. J., et al. 2005, MNRAS, 363, 563

Neugebauer, G., Green, R. F., Matthews, K., Schmidt, M., Soifer, B. T., & Bennett, J. 1987, ApJS, 63, 615

Norman, C., et al. 2002, ApJ, 571, 218

O'Dea, C. P. 1998, PASP, 110, 493

Ogle, P. M., Whysong, D., & Antonucci, R. 2006, ApJ, 647, 161

Omont, A., Beelen, A., Bertoldi, F., Cox, P., Carilli, C. L., Priddey, R. S., McMahon, R. G., & Isaak, K. G. 2003, A&A, 398, 857

Osterbrock, D. E. & Ferland, G. J. 2006, Astrophysics of Gaseous Nebulae and Active Galactic Nuclei (University Science Books)

Osterbrock, D. E. & Pogge, R. W. 1985, ApJ, 297, 1660

Overzier, R. A., Röttgering, H. J. A., Rengelink, R. B., & Wilman, R. J. 2003, A&A, 405, 53

Papadopoulos, P. P. & Ivison, R. J. 2002, ApJL, 564, L9

Patton, D. R., Carlberg, R. G., Marzke, R. O., Pritchet, C. J., da Costa, L. N., & Pellegrini, P. S. 2000, ApJ, 536, 153

Peacock, J. A. 1983, MNRAS, 202, 615

—. 1999, Cosmological Physics (Cambridge University Press)

Peacock, J. A. & Dodds, S. J. 1994, MNRAS, 267, 1020

Pei, Y. C. 1992, ApJ, 395, 130

Polletta, M. d. C. et al. 2006, ApJ, 642, 673

Prandoni, I., Gregorini, L., Parma, P., de Ruiter, H. R., Vettolani, G., Wieringa, M. H., & Ekers, R. D. 2001, A&A, 365, 392

Ranalli, P., Comastri, A., & Setti, G. 2003, A&A, 399, 39

Rawlings, S., Eales, S., & Lacy, M. 2001, MNRAS, 322, 523

Rawlings, S., Eales, S., & Warren, S. 1990, MNRAS, 243, 14P

Rawlings, S. & Saunders, R. 1991, Nat, 349, 138

Rees, M. J. 1984, ARA&A, 22, 471

Reid, M. J., Schneps, M. H., Moran, J. M., Gwinn, C. R., Genzel, R., Downes, D., & Roennaeng, B. 1988, ApJ, 330, 809

Richards, E. A. 2000, ApJ, 533, 611

Richards, E. A., Kellermann, K. I., Fomalont, E. B., Windhorst, R. A., & Partridge, R. B. 1998, AJ, 116, 1039

Richards, G. T., et al. 2003, AJ, 126, 1131

Richards, G. T., Vanden Berk, D. E., Reichard, T. A., Hall, P. B., Schneider, D. P., SubbaRao, M., Thakar, A. R., & York, D. G. 2002a, AJ, 124, 1

Richards, G. T. et al. 2002b, AJ, 123, 2945

Risaliti, G., Maiolino, R., & Salvati, M. 1999, ApJ, 522, 157

Rowan-Robinson, M. 1995, MNRAS, 272, 737

Rowan-Robinson, M., et al. 1991, Nat, 351, 719

Rowan-Robinson, M., et al. 1993, MNRAS, 261, 513

Salpeter, E. E. 1955, ApJ, 121, 161

Sanders, D. B. & Mirabel, I. F. 1996, ARA&A, 34, 749

Sekiguchi, K., Takata, T., Simpson, C., & Akiyama, M. 2001, in , 458

Serjeant, S., Rawlings, S., Lacy, M., McMahon, R. G., Lawrence, A., Rowan-Robinson, M., & Mountain, M. 1998, MNRAS, 298, 321

Seymour, N., McHardy, I. M., & Gunn, K. F. 2004, MNRAS, 352, 131

Shi, Y., et al. 2006, (astro-ph/0608645)

Siebenmorgen, R., Haas, M., Krügel, E., & Schulz, B. 2005, A&A, 436, L5

Siebenmorgen, R. & Kruegel, E. 2006

Silk, J. & Rees, M. J. 1998, A&A, 331, L1

Simpson, C. 1998a, MNRAS, 297, L39

—. 1998b, ApJ, 509, 653

Simpson, C., Rawlings, S., & Lacy, M. 1999, MNRAS, 306, 828

Simpson, C. 2005, MNRAS, 360, 565

Simpson C., et al., 2006, MNRAS, 372, 741

Sivia, D. S. 1996, Data Analysis. A Bayesian Tutorial (Oxford University Press)

Solomon, P. M., Downes, D., Radford, S. J. E., & Barrett, J. W. 1997, ApJ, 478, 144

Solomon, P. M. & Vanden Bout, P. A. 2005, ARA&A, 43, 677

Somerville, R. S., Lee, K., Ferguson, H. C., Gardner, J. P., Moustakas, L. A., & Giavalisco, M. 2004, ApJL, 600, L171

Sopp, H. M. & Alexander, P. 1991, MNRAS, 251, 14P

Spergel, D. N. et al. 2006

Stern, D., et al. 2002, ApJ, 568, 71

Sullivan, M., Hopkins, A. M., Afonso, J., Georgakakis, A., Chan, B., Cram, L. E., Mobasher, B., & Almeida, C. 2004, ApJS, 155, 1

Surace, J. A., Shupe, D. L., Fang, F., Evans, T., Alexov, A., Frayer, D., Lonsdale, C. J., & SWIRE Team. 2005, American Astronomical Society Meeting Abstracts, 207, 63.01

Sutherland, W. & Saunders, W. 1992, MNRAS, 259, 413

Tacconi, L. J., et al. 2006, ApJ, 640, 228

Takeuchi, T. T., Ishii, T. T., Dole, H., Dennefeld, M., Lagache, G., & Puget, J.-L. 2006, A&A, 448, 525

Treister, E. & Urry, C. M. 2005, ApJ, 630, 115

Treister, E., et al. 2004, ApJ, 616, 123

Treister, E., et al. 2006, ApJ, 640, 603

Ueda, Y., Akiyama, M., Ohta, K., & Miyaji, T. 2003, ApJ, 598, 886

Ueda, Y., et al. 1999, ApJ, 518, 656

Urrutia, T., Lacy, M., Gregg, M. D., & Becker, R. H. 2005, ApJ, 627, 75

Urry, C. M. & Padovani, P. 1995, PASP, 107, 803

van Ojik, R., Roettgering, H. J. A., Miley, G. K., & Hunstead, R. W. 1997, A&A, 317, 358

Vanden Berk, D. E., et al. 2001, AJ, 122, 549

Vrtilek, J. M. & Carleton, N. P. 1985, ApJ, 294, 106

Waddington, I., Dunlop, J. S., Peacock, J. A., & Windhorst, R. A. 2001, MNRAS, 328, 882

Wandel, A., Malkan, B. M. & Peterson, M. A., 1999, ApJ, 526, 579

Waskett, T. J., et al., T. X. 2003, MNRAS, 341, 1217

Watanabe C., Ohta K., Akiyama M., Ueda Y., 2004, ApJ, 610, 128

Weedman, D. W., Le Floc'h, E., Higdon, S. J. U., Higdon, J. L., & Houck, J. R. 2006, ApJ, 638, 613

Werner, M. W. et al. 2004, ApJS, 154, 1

White, R. L., Becker, R. H., Helfand, D. J., & Gregg, M. D. 1997, ApJ, 475, 479

Wilkes, B. J., Pounds, K. A., Schmidt, G. D., Smith, P. S., Cutri, R. M., Ghosh, H., Nelson, B., & Hines, D. C. 2005, ApJ, 634, 183

Willott, C. J., Rawlings, S., Blundell, K. M., & Lacy, M. 1998, MNRAS, 300, 625

—. 2000a, MNRAS, 316, 449

Willott, C. J., Rawlings, S., & Jarvis, M. J. 2000b, MNRAS, 313, 237

Willott, C. J., Rawlings, S., & Blundell, K. M. 2001, MNRAS, 324, 1

Willott, C. J., Rawlings, S., Archibald, E. N., & Dunlop, J. S. 2002a, MNRAS, 331, 435

Willott, C. J., Rawlings, S., Blundell, K. M., Lacy, M., Hill, G. J., & Scott, S. E. 2002b, MNRAS, 335, 1120

Willott, C. J., Rawlings, S., Jarvis, M. J., & Blundell, K. M. 2003a, MNRAS, 339, 173

Willott, C. J., et al. 2003b, MNRAS, 339, 397

Willott, C. J., et al. 2004, ApJ, 610, 140

Willott, C. J. 2005, ApJL, 627, L101

Willott, C. J., Martínez-Sansigre, A. & Rawlings, S. 2006, AJ, in press (astro-ph/0610564)

Wilman, R. J. & Fabian, A. C. 1999, MNRAS, 309, 862

Windhorst, R., Mathis, D., & Neuschaefer, L. 1990, in ASP Conf. Ser. 10: Evolution of the Universe of Galaxies, ed. R. G. Kron, 389–403

Windhorst, R. A., Fomalont, E. B., Partridge, R. B., & Lowenthal, J. D. 1993, ApJ, 405, 498

Windhorst, R. A., Miley, G. K., Owen, F. N., Kron, R. G., & Koo, D. C. 1985, ApJ, 289, 494

Windhorst, R. A., van Heerde, G. M., & Katgert, P. 1984, A&AS, 58, 1

Wolf, C., Wisotzki, L., Borch, A., Dye, S., Kleinheinrich, M., & Meisenheimer, K. 2003, A&A, 408, 499

Wolstencroft, R. D., Savage, A., Clowes, R. G., MacGillivray, H. T., Leggett, S. K., & Kalafi, M. 1986, MNRAS, 223, 279

Worsley, M. A., et al. 2005, MNRAS, 357, 1281

Yan, L., et al. 2005, ApJ, 628, 604

Yu, Q. & Tremaine, S. 2002, MNRAS, 335, 965

Zheng, W., et al. 2004, ApJS, 155, 73